

國立交通大學

材料科學與工程學系

博士論文



被動式微小型磁懸浮馬達之動態特性研究

A study of the dynamic behavior of a passive micro magnetic suspension motor

研究生：王建昌

指導教授：姚永德 教授

中華民國九十九年十一月

被動式微小磁懸浮馬達之動態特性研究

A study of the dynamic behavior of a passive micro magnetic suspension motor

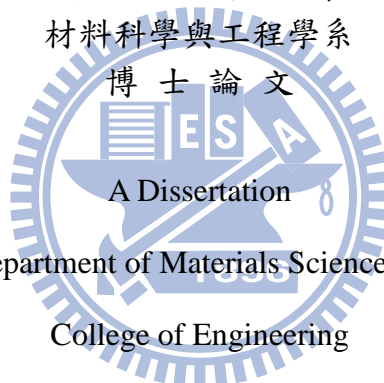
研究生：王建昌

Student : Chien-Chang Wang

指導教授：姚永德 教授

Advisor : Prof. Yeong-Der Yao

國立交通大學
材料科學與工程學系
博士論文



Submitted to Department of Materials Science and Engineering

College of Engineering

National Chiao Tung University

in partial Fulfillment of the Requirements

for the Degree of Doctor of Philosophy

in

Materials Science and Engineering

November 2010

Hsinchu, Taiwan, Republic of China

中華民國九十九年十一月

摘要

本論文主要的目的是研究所提出的一種全被動式微型磁浮軸承馬達的動態特性與其相關效應，該軸承的實現概念是利用高磁能積(N45 材質)的燒結鈮鐵硼磁石產生充分的排斥力，以使得轉子在徑向無接觸地懸浮。本研究非但開發出一種磁浮軸承數學模型，可以成功地分析所發展的微型馬達之動態特性外，而且一種原型製造的設計流程也被成功地提出。結合磁浮軸承數學模型與原型，從理論與實驗指出此微型磁浮馬達的可行性。除基礎的陀螺儀效應與轉子不平衡量效應被觀察之外，微型磁浮軸承相關效應研究尚包含：阻尼效應、軸向偏移的磁力與尺寸小型化也逐一地被加以探討。

在阻尼效應方面，新穎的阻尼裝置由一個高導磁率的磁性環與環狀的橡膠片組成。透過實驗與理論的計算，展示此一創新的阻尼結構可以顯著地提升磁浮馬達的抗衝擊效能。針對軸向偏移磁力的研究方面，一個簡潔的方法運用一種磁石偏移方式，以感應出一個軸向偏移的磁力，可進一步地降低所研究的微型磁浮馬達的徑向振動。關於尺寸效應的研究方面，一款由上述所開發的磁浮軸承小型化之後的原型（外部磁環的內直徑是 5mm，外直徑是 8mm，厚度是 3.6mm）被加以研究，內部與外部由堆疊式架構的高磁能積之環狀永久磁環所組成，這些磁環被配置在轉軸上，且位於轉子的永久磁石與馬達定部之上。經由實驗觀察，心軸在徑向無任何接觸摩擦的狀況之下旋轉。與傳統微型滾珠馬達相互比較之下，微型磁浮馬達可展示出較低的摩擦扭矩損耗。再者，所研究的微型磁浮馬達之徑向振動量，比傳統的微型滾珠馬達者降低了 21%。

前述的論文研究方向以徑向氣隙型馬達為主，本論文最後針對扁平式馬達(軸向氣隙型)，預先進行軸向振動特性研究，研究結果指出：軸向預壓力對此型式馬達的軸向振動表現影響明顯，對未來微型磁浮軸承置入此一系統的研究，具有相當的參考價值。

Abstract

The goal of this dissertation was to investigate the dynamic behaviours and the related effects of a proposed passive magnetic bearing (MB) motor. The concept of the bearing used the repulsive magnetic force to levitate the rotor in the radial direction by utilizing the sintered magnet (N45) with high energy product. Not only a mathematical model for the MB was proposed, which can predict the dynamic characteristics of the developed motor, but also a design procedure for fabricating the prototype was introduced. The mathematical model and the prototype points out that the micro magnetic bearing motor can be carried out on the basis of the developed theory and experiments. Beside the basic gyroscopic effect and rotor unbalance effect were observed, the interesting effects including damping effect, bias-magnetic force effect, and scaled-down effect were discussed one by one.

Regarding the damping effect, an innovative damping device consisting of a magnetic ring of high permeability and an annular rubber pad can apparently increase the anti-shock ability of the MB motor. Moreover, an approach of the vibration reduction utilizing an induced magnetic force was developed. In addition, a prototype of scaled-down MB motor (the outer magnet with an inner diameter of 5 mm, an outer diameter of 8 mm, and a height of 3.6 mm) was studied. Both the inner and outer part was comprised of a stack structure of high energy product magnet. These rings were arranged on the shaft above the PM of the rotor and the stator. From the experimental observation, the shaft can be rotated without any frictional contacts in radial direction. It shows that the micro magnetic bearing (MMB) demonstrates the lower friction torque loss in comparison with the conventional micro ball bearing (MBB). Moreover, the radial vibration of our device is 21 % lower than the conventional MBB type.

The research mentioned above was focused on the motor type with radial air gap. Finally, the dissertation gave the pre-study report regarding a study of axial vibration for a flat-type motor (axial air gap). The results indicate that axial pre-load apparently affects the axial vibration of the motor, and this will be a valuable reference for the research which will be aimed to study the system with the MMB.

Acknowledgements

First, I would sincerely show my gratitude to my supervisor, professor Yeong-Der Yao, whose encouragement, guidance and support from the day that I began this road to so far, particularly, he helped me a lot when I was out of track, confused, and feeling hopeless. I am also grateful to my co-supervisor, professor I Chang, all his concrete support for my overseas study made the special research experience materialized. For sure, the gentleman, professor David Alister Lowther, kindly accepted me as his student, and allowed me to stay at McGill University for one year. I would heartily thankful to everything what he had done to me.

For my colleagues in Industrial Technology Research Institute (ITRI), Chi-Shen Chang, Ann-Huang, Kun-Yi Liang, Chuang-Chun Huang, it is my pleasure to thank you for having made available your support in number of ways. I also thank my directors in ITRI, Dr. Jau-Jiu Ju, Dr. Yu-Choung Chang, and Dr. Bing-Chwen Yang for providing me with the opportunity to pursue the higher education. When I was trapped in the troubles or happy, I was glad that my friends Jun Ouyang, Kao-Shen Chung, Kevin Tang family always accompanied me. I owe my gratitude to them.

Doubtless, I can be a student again and finish writing this text all given by my wife I Ru. She took all the burden of taking care of our sons, managing the daily family life, and listening to my complaints, and I would express my deepest gratitude to her. Definitely, thank my sons Raymond and A Lu Lu for your magic power relieving the pressure from my shoulder as you were surrounding with me. I thank my father for giving me such a free space to extent my life.

Contents

摘要	I
Abstract.....	II
Acknowledgements	III
Contents.....	IV
List of figures	VI
List of Tables	IX
Nomenclature.....	X
Chapter 1 Introduction.....	1
1.1 Small motor	3
1.2 Fundamental configurations of MB.....	4
1.4 Objectives of the thesis.....	11
1.5 Outline of the thesis.....	12
1.6 Original contributions of this dissertation	14
Chapter 2 Mathematical model for the MB.....	17
2.1 Theoretical model.....	17
2.2 Procedures for prototyping the MB.....	32
2.3 Experiment	43
2.4 Results and discussion.....	44
Chapter 3 Damping effect.....	52
3.1 Introduction	52
3.2 Design and simulation	53
3.3 Experimental testing.....	57
3.4 Results and discussion.....	58
Chapter 4 Effect of bias-magnetic force.....	61
4.1 Preview	61
4.2 Design and force calculation	61
4.3 Experiment and results	64
Chapter 5 Design of a scaled-down MB motor for portable disk drives.....	74
5.1 Preview	74
5.2 Configuration of the MMB system.....	75
5.3 Design and analysis	76
5.4 Experiment	79
Chapter 6 Axial vibration study of a mobile fan motor.....	87
6.1 Introduction	87
6.2 Design and force calculation	89
6.3 Experimental measurements.....	92

6.4 Results and discussion	93
Chapter 7 Conclusion	102
Vitae (in Chinese)	106
References	107
Publication List.....	117



List of figures

Chapter 1

Fig. 1- 1. The structure of a small motor for the types of radial and axial air gaps.	4
Fig. 1- 2 Fundamental structures of radial magnetic bearings	6
Fig. 1- 3 Fundamental structures of axial magnetic bearing	7
Fig. 1- 4 Zero axial force of the radial magnetic bearing using symmetrical configuration	8
Fig. 1- 5 Stribeck curve	10

Chapter 2

Fig. 2- 1 Schematic structure of the magnetic bearing motor.....	30
Fig. 2- 2 Frames of reference.....	31
Fig. 2- 3 Geometry of the rotor.....	31
Fig. 2- 4 (a) Rotor is tilted at a critical angle 0° about positive x -axis. (b) Rotor is tilted at a critical angle 1° about positive x -axis.....	33
Fig. 2- 5 3D solid model mesh of the magnetic bearing motor.	34
Fig. 2- 6 2D top view of relative location of the rotor and stator.	38
Fig. 2- 7 3D distribution of rotor and stator.....	39
Fig. 2- 8 (a) Simulated radial force as a function of radial displacement of rotor. (b) The axial force as a function of radial displacement of rotor.	40
Fig. 2- 9 Friction loss of ball bearing type spindle motor.....	42
Fig. 2- 10 Sketch of test rig for the measurement of RRO.....	44
Fig. 2- 11 Force free response of the rotor in (a) time and (b) frequency domains.....	48
Fig. 2- 12 (a) Experimental and (b) simulated time response and frequency spectrum of RRO.	49
Fig. 2- 13 Simulated three dimensional trajectories of the rotor under the rotational speeds of (a) 3000, (b) 4500, and (c) 6000 rpm.....	50
Fig. 2- 14 Simulated RRO excited by mass unbalance: (a) RRO_x and RRO_y ; (b) 3D trajectory of the rotor; (c) time response of RRO; (d) frequency spectrum of RRO.	50
Fig. 2- 15 Simulated three dimensional trajectories of the rotor with the mass unbalances: (a) 0.1×10^{-5} kg·m, (b) 0.2×10^{-5} kg·m, and (c) 0.3×10^{-5} kg·m under the rotational speed of 3000 rpm.....	51
Fig. 2- 16 Comparison of friction torque of Ball bearing and MB motors.....	51

Chapter 3

Fig. 3- 1. Magnetic bearing motor.	54
Fig. 3- 2. The simplified physical model of the magnetic bearing motor system.	56

Fig. 3- 3. B-H curve of stator.	Fig. 3- 4. B-H curve of yoke.	57
Fig. 3- 5 B-H curve of magnet.	Fig. 3- 6 B-H curve of MB.....	57
Fig. 3- 7. (a) Time response and (b) Frequency spectrum without damping device.		59
Fig. 3- 8. (a) Time response and (b) Frequency spectrum with damping device.		60

Chapter 4

Fig. 4- 1. The schematic of the MB motor with a bias magnet.		67
Fig. 4- 2. B-H curve of bias-magnet.		68
Fig. 4- 3. Configuration of the test set-up for axial force measurement.....		69
Fig. 4- 4. (a) The comparison of predicted preload of the MB motor with experimental preload. (b) The comparison of predicted net axial force of the MB motor with experimental net axial force. (c) The comparison of predicted bias-magnetic force of the MB motor and experimental bias-magnetic force. (d) Measured net axial force of the MB motor with bias magnetic force for Dz in different positions.		70
Fig. 4- 5. The radial vibration of the MB motor as a function of the net axial force.		71
Fig. 4- 6. The Radial vibration of the MB motor as a function of the net axial force and Dz.		72
Fig. 4- 7. The dominant magnitude of the radial vibration in frequency domain measured on the bias magnet.		72
Fig. 4- 8. Time responses of radial vibration of the MB motor (a) without (b) with bias-magnetic force.		73

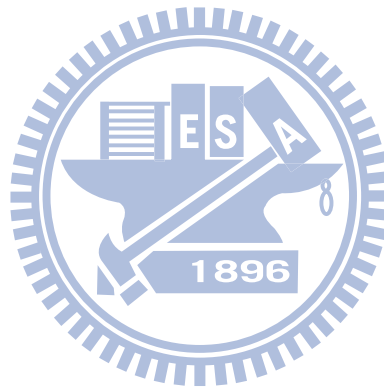
Chapter 5

Fig. 5- 1. The micro magnetic bearing motor.		80
Fig. 5- 2. B-H curve of MQ.		81
Fig. 5- 3. The 3D mesh model of the MMB motor.		82
Fig. 5- 4. Restoring torque varies with the rotation angle and Z_{gap}		82
Fig. 5- 5. Schema of the initial rotation angle between the rotor and stator.		83
Fig. 5- 6. Restoring radial force varies with the rotation angle.		83
Fig. 5- 7 Friction loss due to magnetic axial force		84
Fig. 5- 8. Total friction loss as a function of the rotation angle.		84
Fig. 5- 9. The comparison of friction loss of the MBB and MMB motor.		85
Fig. 5- 10. Radial vibration history of the (a) MBB and (b) MMB motor.		86

Chapter 6

Fig. 6- 1. The sketch of (a) the micro motor and (b) the tilted rotor.		96
Fig. 6- 2. The FEM model of the mobile fan motor.		96
Fig. 6- 3. The simulated axial loads of spatial domain for motors: (a) M4P; and (b) M1		

and M4; the frequency spectra for motors: (c) M4P; and (d) M4.....	97
Fig. 6- 4. The structure of the test setup for the axial load measurement.....	98
Fig. 6- 5. Configuration of the test setup for vibration measurement.	98
Fig. 6- 6. Frequency spectra of (a) radial and (b) axial vibrations for motors M1 to M3.	99
Fig. 6- 7. The frequency spectra of the radial and axial vibrations for motors. Radial vibration: (a) M1P and M1; and (b) M4P and M4; axial vibration: (c) M1P and M1; and (d) M4P and M4.....	100
Fig. 6- 8. The axial vibrations for motors: (a) M1P; (b) M1; (c) M4P; and (d) M4.....	101



List of Tables

Chapter 1

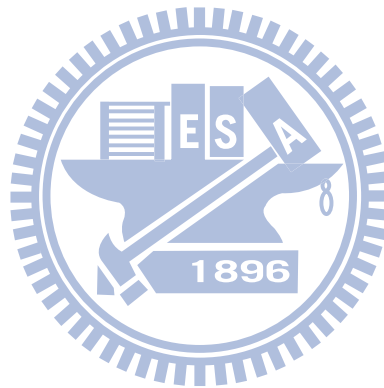
Table 2- 1 Parameters of the MB motor 32

Table 2- 2 T_y and F_z versus various D_{zz} 34

Chapter 6

Table 6- 1 The magnitudes of 1X radial and axial vibration harmonics for motors M1P and M1 to M3..... 95

Table 6- 2 The magnitudes of radial and axial vibration harmonics for motors M4P and M4 95



Nomenclature

$$G = 9.8 \text{ m/s}^2$$

XYZ = coordinate system fixed to stator

$\mathbf{I}, \mathbf{J}, \mathbf{K}$ = unit vectors of XYZ coordinate system

O = origin of the XYZ coordinate system

$X'Y'Z'$ = coordinate system fixed to rotor

O' = origin of the $X'Y'Z'$ coordinate system, fixed to the center mass of the rotor

xyz = coordinate system fixed to rotor (body coordinate system)

$\mathbf{i}, \mathbf{j}, \mathbf{k}$ = unit vectors of body coordinate system

o = origin of xyz coordinate system

X_{CM}, Y_{CM}, Z_{CM} = displacements of CM in $X, Y,$ and Z axes

θ, ϕ, ψ = Eulerian angles

$q_n, n=1-12$ = defined in equation (9)

$y_n, n=1-6$ = defined in equation (10)

$\{Q(t)\}$ = defined in equation (10)

$\{Y(t, q_n)\}$ = defined in equation (10)

$\{K_1\}, \{K_2\}, \{K_3\}, \{K_4\}$ = defined in equations (40)-(43)

t_i = time at i -th instant

Δt = time step

ω = angular velocity of the rotor

Ω = angular velocity for the axes of the body

$\sum F_x, \sum F_y, \sum F_z$ = total forces acting on rotor along X, Y, and Z axes

$\sum T_x, \sum T_y, \sum T_z$ = total torques acting on rotor along x, y, and z axes

I_y, I_z = principle moments of inertia about y and z axes

k = stiffness coefficient of MB motor

c = damping coefficient of MB motor

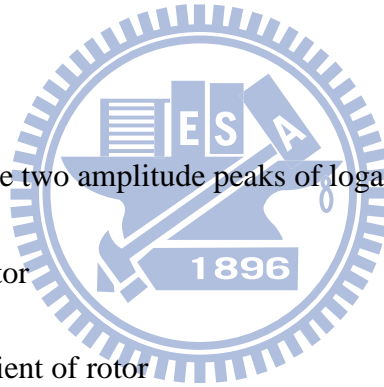
ζ = damping ratio of MB motor

δ = logarithmic decrement

τ_d = time interval between the two amplitude peaks of logarithmic decrement

ω_n = natural frequency of rotor

c_c = critical damping coefficient of rotor



Chapter 1

Introduction

Due to the outstanding magnetic performance, NdFeB material is broadly used in various applications, for example, home appliance, information data storage, communication, consumer electronics, electrical automobile industrial, and so on. The maximum energy product $(BH)_{max}$ of 50.6 MGOe was first reported by Sagawa et al. in 1987, and below 1500 ppm of oxygen was employed [1]. According to Sagawa's calculation the theoretical $(BH)_{max}$ of $Nd_2Fe_{14}B$ alloy is 64 MGOe [2]. Since many scientists are devoted to developing the novel fabrication process in order to make the powerful magnetic material available, nowadays, NdFeB material is the great candidate for levitating the rotor in a motor. The non-contact capability of fully passive magnetic levitation, which has been improved due to the widespread availability of sintered NdFeB magnets with high performance, has many merits, among which are low-loss, high-speed, and flexibility (namely the capability of working in special or worse environments, e.g., the environment in which much more dust particles are floating), and so on. Magnetic levitation fascinates many scientists and researchers, who have concentrated their efforts and reports on the development of alternative approaches to achieve a passive system. As a result, it is now well-known that diamagnetic materials

[3]-[4], superconductors [5], and eddy currents [6] can be used to develop possible stable passive levitation systems. In their development, one usually needs to deal with the intrinsically unstable issue specified by Earnshaw's theorem [7]. Simon *et al.* [8] reported that the magnetic top can be stabilized within certain limitations of spin speed, and the gyroscopic effect was introduced to illustrate his work. To get around the instability, research demonstrating that NdFeB magnets can be statically levitated using the auxiliary objects made of diamagnetic or powerful superconductor materials was carried out by Simon *et al.* [1] Pursuing the practical magnetic bearing, Yonnet *et al.* [9] thoroughly investigated the basic configurations of MBs consisting of two ring magnets and developed the calculation methods to depict the characteristics of these MB structures. In addition, Yonnet *et al.* [10] pointed out that new stacked structures, composed of magnet rings with a rotating magnetization direction, can increase the stiffness of the MBs; furthermore, he demonstrated that the properties of two repulsive radial MB configurations are exactly the same; both of them have the same mechanical dimensions but different magnetization directions (axial or radial). Wang *et al.* [11] constructed an effective structure, consisting of a magnetic ring and an annular-shaped rubber pad, can enormously improve the anti-shock performance for a passive magnetic bearing motor. Many researchers [3]-[11] have been involved in analyzing and investigating magnetic levitation or magnetic bearings; nevertheless, no research has

been focused on the subject of an entirely passive MB designed for small spindles considering a credible dynamic model. In this thesis, a prototype of a passive MB with a compact structure which is capable of being scaled-down is fabricated, and the dynamic behaviours are experimentally and numerically studied.

1.1 Small motor

Small motor is widely used in consumer electronic devices, for example, hard disk drives, scanners, mobile phones, digital cameras, digital video recorders, optical disk drives (including CD series, DVD series, and Blue ray series, and so on), laptops (for example, the cooling fans), and so on. Fig. 1-1 demonstrates the structures for the small motor with two types of air gap which are radial (see the left hand side of the graph) and axial (see the right hand side of the graph) types. The axial type also is called flat type.

In general, a small motor consists of a rotor and a stator. The rotor, which is a rotational part, comprises of a multi-pole permanent magnet (PM), a yoke, and a shaft. The rotor is conjunction with a stator via the bearing. The stator, which is a fixed part, comprises a coil, a case and a base. The bearing functions as a heart of the small motor, because it apparently affects the life-span, acoustics and vibration performances, and so on. The conventional bearings broadly used are ball [12]-[13] and sleeve [14]-[16] bearings. These mechanical bearings limit the maximum speed of the small motor and life-span due to the mechanical contact friction (for ball bearing) and mental wear (for sleeve

bearing's leakage of lubrication oil). However, very little research has been studied or reported about the passive magnetic bearing with the feature of non-contact capability, which can beat the demon friction mentioned above, particularly, for a small motor of which power consumption is lower than 10 W. Therefore, it is worth to deal with the behaviour of the small motor employing the MB in order to become one of the alternative candidate bearings to replace the sleeve or ball bearings in the future.

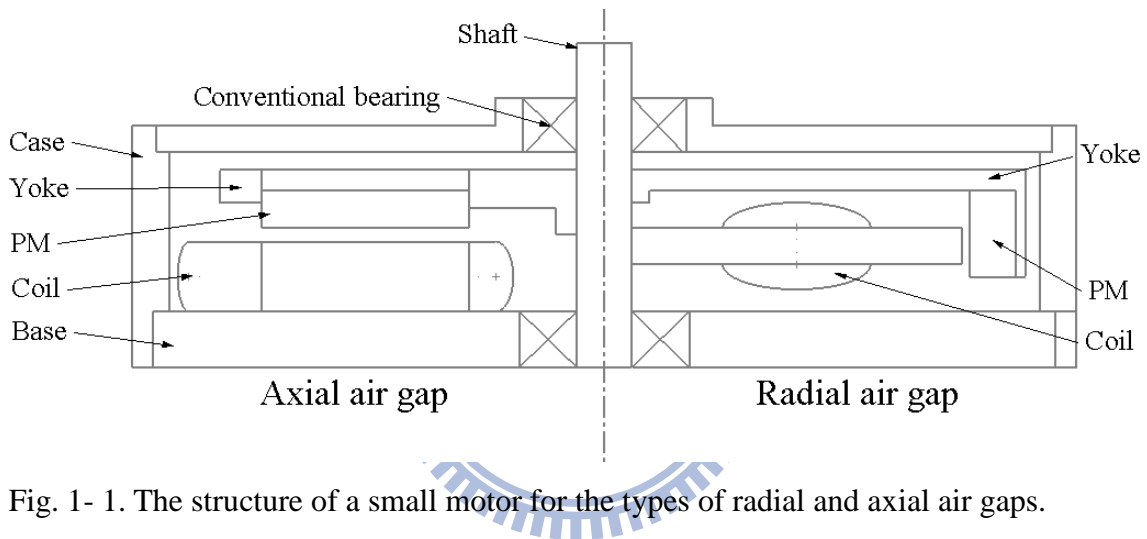


Fig. 1- 1. The structure of a small motor for the types of radial and axial air gaps.

1.2 Fundamental configurations of MB

The use of permanent magnets to construct magnetic bearings has been studied for more than half century. In 1964, Geary *et al.* [15] summarized the possible and demonstrated configurations of permanent magnet bearings which have been proposed before that date. In 1981, Yonnet *et al.* [18] paid attention to the compact magnetic bearing which consists of two permanent magnets with simple annular shape, particularly, the magnets magnetized in axial and radial direction are considered. By

calculating the forces and stiffness, he demonstrated ten structures of magnetic bearing including both radial and axial bearings. Fig. 1- 2 shows the fundamental structures of the radial bearing, i.e., there exists instability in axial direction while there exists an unstable state in radial direction for the axial bearing. The structures shown in Fig. 1- 2 (b) can be obtained by simply switching the magnetization direction of magnets in Fig. 1- 2 (a), and these two types of magnetic bearing are exactly the same. Fig. 1- 3 represents the useful outlines of the axial bearing, which can be gained by changing the magnetization of the magnet, one magnet each time, in Fig. 1- 2. When undesired axial force is generated, for example, type R51 series (i.e., R51 and RevR51) or A51 series (i.e., A51 and RevA51) represents the strongest axial force while type R11 series (i.e., R11 and RevR11) or A11 series (i.e., A11 and RevA11) has a zero axial force. In order to manipulate the axial force, Yonnet *et al.* proposed the approach to eliminate the axial force to be zero by introducing a symmetrical arrangement for the radial bearing, as shown in Fig. 1- 4. Moreover, one can adjust the preferred axial force by allocating the permanent magnets around the optimal position.

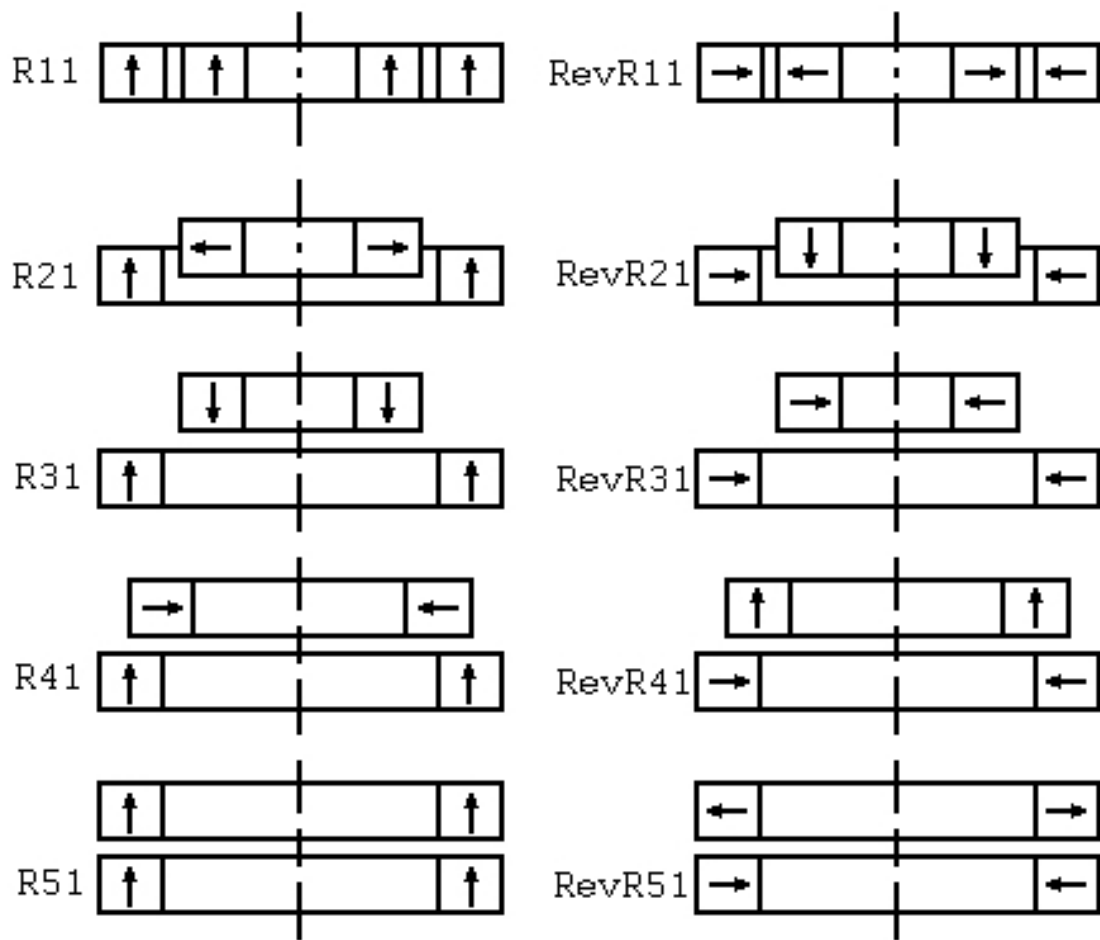


Fig. 1- 2 Fundamental structures of radial magnetic bearings

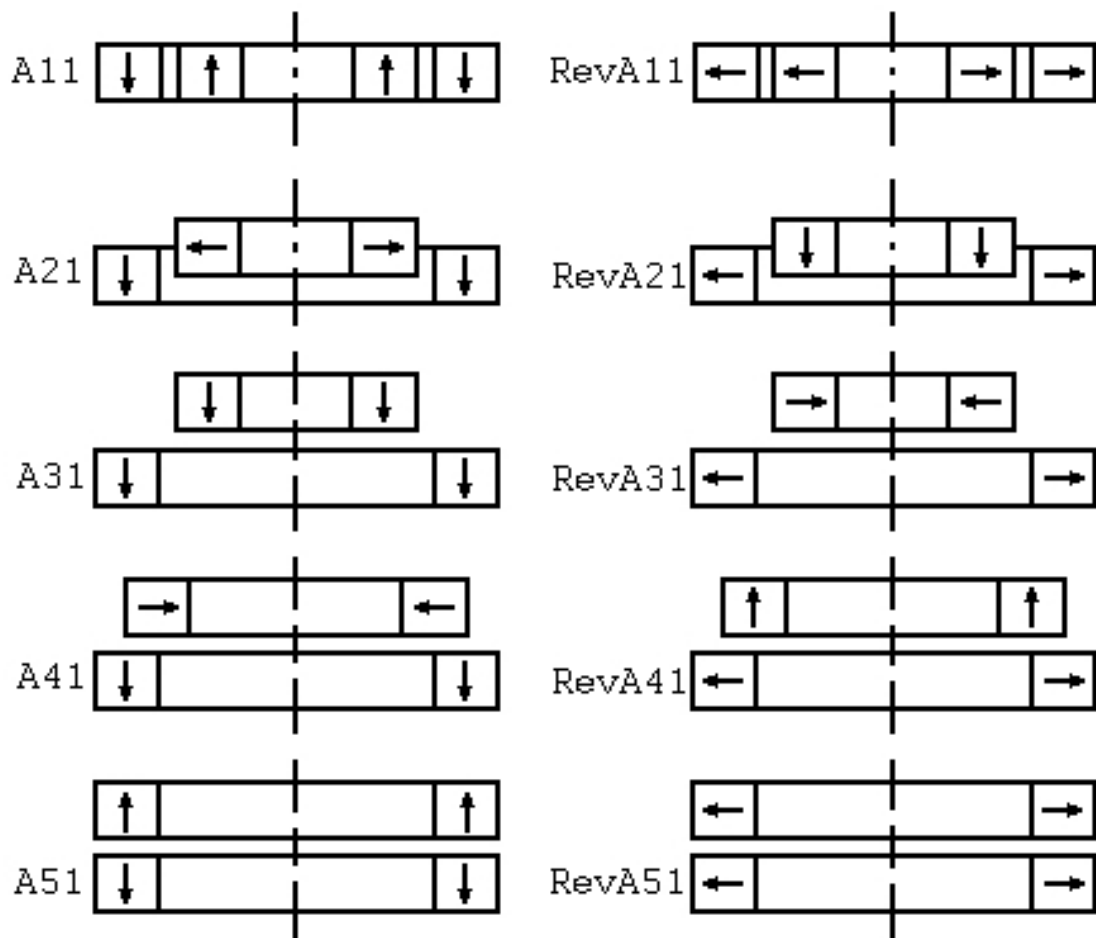


Fig. 1- 3 Fundamental structures of axial magnetic bearing

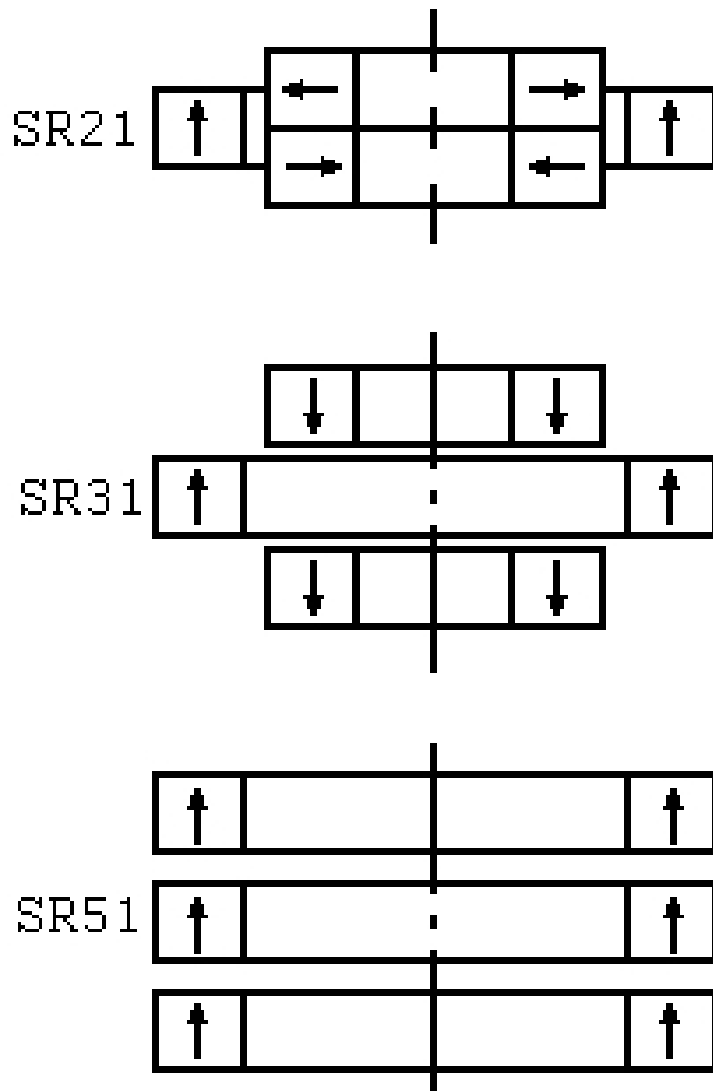


Fig. 1- 4 Zero axial force of the radial magnetic bearing using symmetrical configuration

1.3 Small sleeve bearing system

Since a plane sleeve bearing (or so-called oil-impregnated bearing) possesses the advantages of cost effective and suitably developed for mass production, it was widely used in cooling fan motors, optical disk drives, and so on. In a small spindle motor developed for the above applications, the plane sleeve, which is able to maintain the RRO of the rotor to a desired value and reduce the friction, can generate boundary lubrication [19]-[22]. In general, lubrication can be classified into three mode, boundary lubrication, hybrid lubrication, and fluid lubrication, which revealed by Stribeck [19] on the basis of observing friction experiments on bearings. As shown in Fig. 1- 5, the well-known Stribeck curve demonstrates the relationship between the friction coefficient, viscosity of the lubricating oil, load, and velocity. The vertical and horizontal axes represent the friction coefficient, and bearing parameter, respectively. The parameter is $(\text{viscosity}) \times (\text{velocity})/\text{load}$. In addition, the solid friction is specified in the curve. In the plot, on the top right, the graph clearly illustrates that there exists a thin oil-film formed by only several oil molecules between the shaft and the bearing, and it also occurs a solid friction between them.

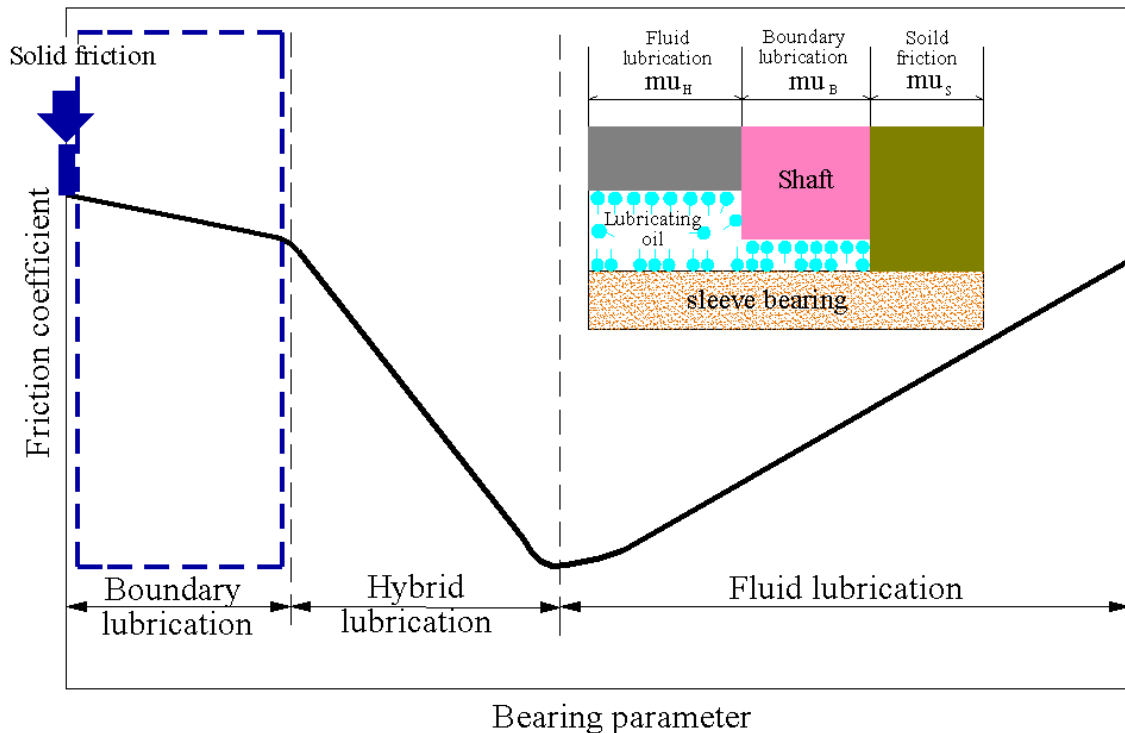


Fig. 1- 5 Stribeck curve

As described above, the lubricated surface between the sleeve bearing and the rotor of the small spindle, though, can not prevent partial contact between the rotor and the sleeve. In other words, the partial contact will result in a failure of the sleeve or vibration of the system. Consequently, it is helpful to this project to study the dynamic behaviour of the small plane sleeve after it is installed into a spindle. Because the physical model of the proposed MB is similar to the sleeve bearing, it is good to understand and review these prior studies which are related to a rotary machine.

Lund *et al.* [23] showed that the comparison of critical speeds predicted by the analysis of rotor response and the results investigated by experiments has shown good agreement. Ehrich *et al.* [24] addressed that whip-free rubbing may be achieved if the rotor system is designed with the similar dampings for both rotor and stator, and their

natural frequencies are manipulated to be different. Begg *et al.* [25] published a study related to the stability of a rotor which discussed the considerations of the power dissipation due to damping and power input due to friction. He found that the stability is affected by the friction-to-damping ratio. For studying the transient analysis of the rotor system, Choy *et al.* [26] used Jeffcott rotor to determine the effects of casing stiffness, friction coefficient, imbalance load, and system damping characteristics. The conclusion is that an increase in system stiffness, friction coefficient, system damping, and imbalance load can lead to an earlier onset of backward whirl.

According to the above literature review, it points out that the interesting items needed to be investigated for the developed MB include the effect of mass unbalance, the gyroscopic effect, and the effect of friction force acting at the pivot point. However, a valid physical model has to be proposed before these key factors affecting the dynamic characteristics can be parametrically studied and analyzed. So, this dissertation will be focused on figuring out a compact and simple configuration of MB, and then an equivalent model will be addressed in order to realize the dynamic behaviours of the MB installed in a desired motor.

1.4 Objectives of the thesis

The main objectives of this thesis were to develop, investigate, and validate a

proposed mathematical model stating the dynamic behaviour of a developed MB motor with single pivot point in conjunction with a thrust plate; especially, the MB designed with an easy and compact structure, and effectively improved the damping ratio. Moreover, this thesis aims to present a method of vibration reduction by utilizing a novel bias-magnetic force. Moreover, this thesis develops a procedure to implement a prototype of scaled-down MB motor with suppressed magnetic coupling effect for SFFO drives.

1.5 Outline of the thesis

The thesis is composed of 6 chapters. Chapter 2 provides the detail components and architecture of the proposed MB and reports the theoretical model for modeling and understanding of the behaviour of the desired MB. After validating the stability of the MB, Chapter 3 and Chapter 4 indicate the magnetic force induced damping effect and the effect of bias-magnetic force for improving the damping ratio of the MB motor and decreasing the radial vibration of the motor, respectively. Chapter 5 addresses the developed micro-magnetic MB motor which has 18.5 mm in outside diameter and 3.6 mm in height. Chapter 6 represents an axial vibration study of a mobile fan motor. Finally, Chapter 7 draws the conclusion of the thesis and gives the suggestions for the future work. The framework of the thesis is organized in the following.

Chapter 2 presents the structure of the proposed MB on the basis of review of prior

arts, and the totally passive structure consisting of sintered NdFeB rings is highly compact. A mathematical model was developed to evaluate the dynamic behaviour of the system. The governed equations for the simulation of the real system were Newton-Euler equations of motion. By using the numerical integration of RK4, the nonlinear equations were solved. The relationship between the model and the real system was clearly addressed and discussed.

Chapter 3 locates in the interest of an innovative damping induced by magnetic force. The unit of a magnetic ring of high permeability and an annular-shaped rubber pad mounted on the stator for increasing the damping ratio of the MB system was developed. The impulse method was used to determine the natural frequencies for lateral and rotational modes of the rotor. Chapter 3 summarizes the effectiveness of the damping device in terms of the anti-shock performance of the MB motor.

Chapter 4 presents a compact method adopting a novel bias magnet to induce an axial bias-magnetic force, which effectively contributes to the vibration reduction of the MB motor. The use of the axial force for affecting the vibration of the MB system was thoroughly discussed.

Chapter 5 is dedicated to the development of a MMB (Micro magnetic bearing) motor, particularly the micro motor is considered to be used in a SFFO drive. The magnetic coupling effect was taken into account when designing the device. This

chapter examined the mechanical and electrical characteristics of the MMB motor in comparison with the conventional micro ball bearing motor (MBB). Finally, the performance of the MMB motor was reported.

Chapter 6 is focused on the study of axial load effect for a flat-type motor operating with and without the rated axial thrust force. It demonstrates that axial load plays an effective and crucial factor in controlling the axial vibration of the mobile fan motor.

Chapter 7 draws the conclusion of the thesis by means of summarization of the jobs which has been done and gives the suggestion for the future work.

1.6 Original contributions of this dissertation

The original contributions of this dissertation are summarized as follows:

A very compact and simple MB structure for miniature motors is proposed; moreover, the developed mathematical model can successfully describe the dynamic behaviour of the MB motor. An entirely passive MB structure consisting of two sets of very compact sintered NdFeB rings is successfully achieved to make the contactless rotor of the prototyped motor stably levitated in the radial direction, and low friction torque is experimentally verified. A gyroscopic effect is observed, and it effectively suppresses the radial vibration due to the mass imbalance of the rotor. The consistent dynamic results are evaluated by adopting a proposed mathematical model numerically solved with RK4.

An innovative damping structure is presented. An innovative damping induced by magnetic force was designed successfully for the totally passive magnetic bearing motor. A magnetic ring of high permeability and an annular-shaped rubber pad were mounted on the stator 0.55mm below the permanent magnet of the rotor. Computer simulations were compared with experimental measurements for deciding material and configuration of the critical components. The natural frequencies for lateral and rotational modes of the rotor are around 22 Hz measured by impulse method. Both the magnetic bearing motor without and with magnetic damping are rotated at rated speed 3840 rpm, which is far above the first critical speed of 1305 rpm. Without magnetic damping, the natural damping ratio in radial direction of the rotor is 0.0655. After damping, it increases to 0.1401. We have demonstrated by both experimental measurement and theoretical calculation that the anti-shock performance is significantly improved by the innovative damping technology in a passive magnetic bearing motor.

The use of bias-magnetic force shows that the radial vibration of the MB motor is significantly reduced. A compact method using a novel bias magnet to induce an axial bias-magnetic force in order to reduce the radial vibration of the MB motor is introduced. After applying the bias-magnetic force, the optimal radial vibration of the developed MB motor is only around 0.197 G when the natural frequency of the bias magnet reaches the resonant frequency of 62 Hz. In this optimal condition the ratio in

the radial vibration of the MB motor with the bias-magnetic force to the original one is around 89 percent, and the driving power of 0.24 W is saved.

A MMB motor intends to apply in a portable optical disk drive was developed. The novel MMB motor was developed with an inner and outer magnetic-ring stack structure of high permeability. These rings were arranged on the shaft above the permanent magnet of the rotor and the stator. The magnetic force between the MMB, the permanent magnet and the stator induced the magnetic coupling effect that generated the demon friction torque loss. However, the loss was controlled well under 1.93×10^{-4} Nm by the proposed approach, so that the good stable system was achieved. After suppressing the loss caused by the magnetic coupling effect, the shaft can be rotated without any frictional contacts in radial direction, the running current was around 0.18 A, and the maximum speed was around 1850 rpm. It shows that the MMB demonstrates the lower friction torque loss in comparison with the conventional MBB. Moreover, the radial vibration of our device is 21 % lower than the conventional MBB type. To verify the performance of the provided system, both the computer simulation and experiment were performed.

Chapter 2

Mathematical model for the MB

2.1 Theoretical model

The prototype of the developed magnetic bearing motor, in which the rotor is stably levitated, is equipped with two MBs, upper and lower, as shown in Fig. 2- 1. Each of the MBs consists of two permanent magnet rings made of NdFeB with an energy product of 45 MGOe, and each is axially magnetized. The inner diameter, outer diameter, and height for the inner ring are 3×10^{-3} , 6×10^{-3} , and 4×10^{-3} m, respectively, and the corresponding dimensions for the outer one are 7×10^{-3} , 10×10^{-3} , and 4×10^{-3} m, respectively. These two MBs are properly located along the axial direction by employing two cylindrical washers. Only a single pivot point of the rotor in conjunction with the stator is introduced, and it is supported by a thrust plate fixed above the base. In addition to the inside part of the two MBs, a rotor part composed of ferrite permanent magnet with a yoke attached to it is connected to the shaft via a yoke bush, and the diameter of the rotor is 4.1×10^{-2} m. The power can be input through the printed circuit board (PCB) to generate the repulsive and attractive magnetic torque between rotor and stator to drive the spindle.

Frames of reference are defined as shown in Fig. 2- 2. The coordinate (fixed frame) with XYZ axes is an inertial set with origin O. The coordinate with X'Y'Z' axes, the

origin of which is O' , is located at the center of mass of the rotor (CM), and the orientation of this coordinate is supposed not to be altered. The origin o of the body coordinate with xyz axes is attached to the same position as O' , and the z axis is along the symmetry axis of the rotor. Then, the Eulerian angles θ , ϕ , and ψ , as well as the corresponding angular velocities $\dot{\theta}$, $\dot{\phi}$, and $\dot{\psi}$, can clearly be defined and associated with a vector on which an infinitesimal rotation or time derivative is imposed. Supposing that the xyz axes are not to be rotated about the z axis, the angular velocities for the rotor and axes of the body can be represented as:

$$\boldsymbol{\omega} = -\dot{\phi} \sin \theta \mathbf{i} + \dot{\theta} \mathbf{j} + (\dot{\psi} + \dot{\phi} \cos \theta) \mathbf{k} \quad (1)$$

$$\boldsymbol{\Omega} = -\dot{\phi} \sin \theta \mathbf{i} + \dot{\theta} \mathbf{j} + \dot{\phi} \cos \theta \mathbf{k} \quad (2)$$

where $\boldsymbol{\omega}$ is the angular velocity of the rotor, $\boldsymbol{\Omega}$ is the angular velocity for the axes of the body, and \mathbf{i} , \mathbf{j} , and \mathbf{k} are the unit vectors in the x , y , and z directions, respectively. Referring to the Newton-Euler equations of motion for a rigid body, which the desired system is assumed to be, the mathematical model for the proposed system can be expressed in the following.

$$\sum F_x = m\ddot{X}_{CM} \quad (3)$$

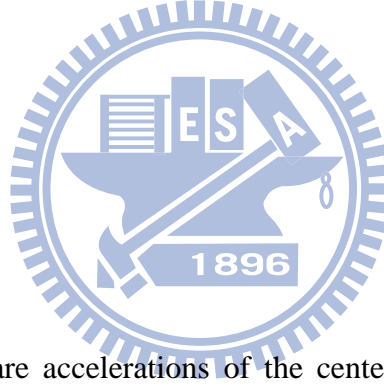
$$\sum F_Y = m\ddot{Y}_{CM} \quad (4)$$

$$\sum F_Z = m\ddot{Z}_{CM} \quad (5)$$

$$\sum T_x = -I_y(\ddot{\phi} \sin \theta + 2\dot{\theta}\dot{\phi} \cos \theta) + I_z(\dot{\theta}\dot{\psi} + \dot{\phi} \cos \theta) \quad (6)$$

$$\sum T_y = I_y(\ddot{\theta} - \dot{\phi}^2 \sin \theta \cos \theta) + I_z\dot{\phi} \sin \theta(\dot{\psi} + \dot{\phi} \cos \theta) \quad (7)$$

$$\sum T_z = I_z \frac{d}{dt}(\dot{\psi} + \dot{\phi} \cos \theta) \quad (8)$$



where \ddot{X}_{CM} , \ddot{Y}_{CM} , and \ddot{Z}_{CM} are accelerations of the center of mass of the rotor along X-axis, Y-axis, and Z-axis, respectively. I_y and I_z are the principle moments of inertia about y and z axes, respectively. It is obvious that total forces and torques acting on the rigid body are expressed in fixed frame body coordinate system, respectively.

The external forces considered in the MB motor are a mass unbalance force due to the mass imbalance of the rotor, a MB force along the radial direction, and friction and axial preload forces due to the pivot thrust plate. Then, the nonlinear equations (3)-(8) can be numerically solved by applying the RK4, combined with an iteration procedure

[27] which Wang et al. derived for modeling the porous bearing of a spindle motor.

For solving differential system equations described above, on the left hand side of the equations (3)-(8) are needed to be connected to the parameters of the MB motor which are shown in Table 2- 1. The detail derivation of these external forces and torques are illustrated in the following.

To rewrite equations (3)-(8) as the expected form of equation, $\sum F_x$, $\sum F_y$, $\sum F_z$, $\sum T_x$, $\sum T_y$, and $\sum T_z$ have to be represented in terms of X_{CM} , Y_{CM} , Z_{CM} , Eulerian angles, and their derivatives. Considering the external forces acting on the rotor which are pivot force, radial magnetic bearing force, and unbalance force, the derivation is carried out as follows:

(1) Pivot force

As shown in Fig. 2- 3, a point 3 designates the pivot point. The l_1 , l_2 , and l_3 designate the axial distances from CM to MB 1, MB 2, and the bottom of the shaft, respectively. Suppose that the rotor is unbalanced, and the unbalance can be represented by a mass \bar{m} , which is located at a distance \bar{e} and l_e from the CM along radial and axial directions, respectively.

The external forces acting at the mentioned point 3 are friction force and normal contact force. The weight of the rotor and the friction coefficient between the shaft and the thrust plate are mg and μ , respectively. Supposing the velocity of the pivot point is

known, the total force acting at this point can be calculated. In the fixed coordinate system XYZ the velocity of the pivot point can be represented as

$$\mathbf{V}_3 = \mathbf{V}_{O'} + \mathbf{V}_{3O'} \quad (9)$$

The relative velocity $\mathbf{V}_{3O'}$ can be calculated as follows:

$$\mathbf{V}_{3O'} = \boldsymbol{\omega} \times \mathbf{R}_{3O'} \quad (10)$$

where $\mathbf{R}_{3O'}$ (see Fig. 2- 3) is the position vector of point 3 relative to O' and can be expressed as follows.

$$\mathbf{R}_{3O'} = r \sin \theta \mathbf{i} + (l_3 - (r - r \cos \theta)) \mathbf{k} \quad (11)$$

Substituting equation (1) and (I-3) into (I-2), so that $\mathbf{V}_{3O'}$ can be expressed in the moving coordinate system xyz and defined as follows:

$$\mathbf{V}_{3O'} \equiv (V_{3O'})_x \mathbf{i} + (V_{3O'})_y \mathbf{j} + (V_{3O'})_z \mathbf{k} \quad (12)$$

In the fixed coordinate system, these vectors of $\mathbf{V}_{3O'}$ are obtained by performing the matrix multiplication of inverse of transformation matrix $[\text{DCM}]^{-1}$ and $\mathbf{V}_{3O'}$, i.e., the $[\text{DCM}]^{-1}$ matrix implements the coordinate transformation of a vector in moving frame $((V_{3O'})_x, (V_{3O'})_y, (V_{3O'})_z)$ into a vector in fixed frame $((V_{3O'})_X, (V_{3O'})_Y, (V_{3O'})_Z)$, thus

$$\begin{Bmatrix} (V_{3O'})_X \\ (V_{3O'})_Y \\ (V_{3O'})_Z \end{Bmatrix} = [\text{DCM}]^{-1} \begin{Bmatrix} (V_{3O'})_x \\ (V_{3O'})_y \\ (V_{3O'})_z \end{Bmatrix} \quad (13)$$

where DCM is the well known coordinate transformation matrix, and is expressed as

$$\text{DCM} = \begin{bmatrix} \cos\theta \cos\phi & \cos\theta \sin\phi & -\sin\theta \\ -\sin\phi & \cos\phi & 0 \\ \sin\theta \cos\phi & \sin\theta \sin\phi & \cos\theta \end{bmatrix} \quad (14)$$

Substituting equation (14) into equation (13), the velocity of the pivot point can be represented as,

$$\begin{aligned} \mathbf{V}_3 &= \begin{Bmatrix} \dot{X}_{CM} \\ \dot{Y}_{CM} \\ \dot{Z}_{CM} \end{Bmatrix} + \begin{Bmatrix} (V_{3O'})_X \\ (V_{3O'})_Y \\ (V_{3O'})_Z \end{Bmatrix} \\ &\equiv \begin{Bmatrix} (V_3)_X \\ (V_3)_Y \\ (V_3)_Z \end{Bmatrix} \end{aligned} \quad (15)$$

Supposing \mathbf{v} is the unit vector of \mathbf{V}_3 , and then \mathbf{v} can be represented as

$$\begin{aligned} \mathbf{v} &= \frac{(V_3)_X}{|\mathbf{V}_3|} \mathbf{I} + \frac{(V_3)_Y}{|\mathbf{V}_3|} \mathbf{J} + \frac{(V_3)_Z}{|\mathbf{V}_3|} \mathbf{K} \\ &\equiv v_x \mathbf{I} + v_y \mathbf{J} + v_z \mathbf{K} \end{aligned} \quad (16)$$

The magnitude of the velocity vector \mathbf{V}_3 is

$$|\mathbf{V}_3| = [(V_3)_X^2 + (V_3)_Y^2 + (V_3)_Z^2]^{1/2} \quad (17)$$

Because an axial force of 1.887 N is applied along the axial direction, it is believed that the shaft is always in contact with the thrust plate. Therefore, the unit vector of the velocity of the contact point should be as

$$\mathbf{v} = v_x \mathbf{I} + v_y \mathbf{J} \quad (18)$$

The friction force can then be represented as

$$\mathbf{F}_f = -\mu(mg + F_a)(v_x \mathbf{I} + v_y \mathbf{J}) \quad (19)$$

where μ , m , and F_a are friction coefficient between thrust plate and shaft, mass of the

rotor, and axial preload force, respectively.

Thus, the total force acting at the contact point is

$$\mathbf{F}_3 = -\mu(mg + F_a)v_x \mathbf{I} - \mu(mg + F_a)v_y \mathbf{J} + (mg + F_a) \mathbf{K} \quad (20)$$

By operating the transformation matrix [DCM] to \mathbf{F}_3 , so that \mathbf{F}_3 can be expressed in the xyz coordinate system to be as

$$\begin{aligned} \{\mathbf{F}_3\}_{xyz} &= \begin{Bmatrix} (F_3)_x \\ (F_3)_y \\ (F_3)_z \end{Bmatrix} \\ &= [\text{DCM}]^{-1} \begin{Bmatrix} (F_3)_X \\ (F_3)_Y \\ (F_3)_Z \end{Bmatrix} \end{aligned} \quad (21)$$

Finally, the torque about O' resulted from the contact force is as

$$\begin{aligned} \mathbf{T}_3 &= \mathbf{R}_{3O'} \times \mathbf{F}_3 \\ &= \begin{vmatrix} \mathbf{i} & \mathbf{j} & \mathbf{k} \\ r \sin \theta & 0 & l_3 - (r - r \cos \theta) \\ (F_3)_x & (F_3)_y & (F_3)_z \end{vmatrix} \\ &= -(l_3 - (r - r \cos \theta))(F_3)_y \mathbf{i} + \\ &\quad ((l_3 - (r - r \cos \theta))(F_3)_x - r \sin \theta (F_3)_z) \mathbf{j} + \\ &\quad r \sin \theta (F_3)_y \mathbf{k} \end{aligned} \quad (22)$$

where

l_3 = distance from CM to shaft bottom in z -axis

r = radius of the fillet of shaft bottom

(2) Radial magnetic bearing force

It is assumed that the radial stiffness of MB 1 (upper) and MB 2 (lower) are identical.

The components of radial MB force along X -axis are

$$(F_{k1})_X = -k_X (X_{CM} + \Delta X_1) \quad (23)$$

$$(F_{k2})_X = -k_X (X_{CM} + \Delta X_2) \quad (24)$$

The components of radial MB force along Y -axis are

$$(F_{k1})_Y = -k_Y (Y_{CM} + \Delta Y_1) \quad (25)$$

$$(F_{k2})_Y = -k_Y (Y_{CM} + \Delta Y_2) \quad (26)$$

Thus, in the fixed coordinate system, the force due to the stiffness of radial MB can be represented as

$$\{\mathbf{F}_k\}_{XYZ} \equiv \begin{Bmatrix} (F_k)_X \\ (F_k)_Y \\ (F_k)_Z \end{Bmatrix} = \begin{Bmatrix} (F_{k1})_X + (F_{k2})_X \\ (F_{k1})_Y + (F_{k2})_Y \\ (F_{k1})_Z + (F_{k2})_Z \end{Bmatrix} \quad (27)$$

By operating the transformation matrix [DCM] to the force vectors $\{\mathbf{F}_{k1}\}_{XYZ}$ and $\{\mathbf{F}_{k2}\}_{XYZ}$, respectively. Then, in the moving frame, the corresponding force vectors can

be represented as

$$\{\mathbf{F}_{k1}\}_{xyz} = \begin{Bmatrix} (F_{k1})_x \\ (F_{k1})_y \\ (F_{k1})_z \end{Bmatrix} = [DCM] \begin{Bmatrix} (F_{k1})_X \\ (F_{k1})_Y \\ (F_{k1})_Z \end{Bmatrix} \quad (28)$$

$$\{\mathbf{F}_{k2}\}_{xyz} = \begin{Bmatrix} (F_{k2})_x \\ (F_{k2})_y \\ (F_{k2})_z \end{Bmatrix} = [DCM] \begin{Bmatrix} (F_{k2})_X \\ (F_{k2})_Y \\ (F_{k2})_Z \end{Bmatrix} \quad (29)$$

The torque about O' due to the stiffness of radial MB can be expressed as

$$\mathbf{T}_k = [(F_{k1})_y l_1 + (F_{k2})_y l_2] \mathbf{i} - [(F_{k1})_x l_1 + (F_{k2})_x l_2] \mathbf{j} \quad (30)$$

where

$\Delta X_1, \Delta X_2$ = upper and lower MB displacement relative to the CM in the X direction

(these two variables can be further expressed in terms of the unknown variables Eulerian angles)

$\Delta Y_1, \Delta Y_2$ = upper and lower MB displacement relative to the CM in the Y direction

(these two variables can be further expressed in terms of the unknown variables Eulerian angles)

k_X = radial MB stiffness in X direction

k_Y = radial MB stiffness in Y direction

$(F_{k1})_X, (F_{k2})_X$ = upper and lower MB forces in X direction

$(F_{k1})_Y, (F_{k2})_Y$ = upper and lower MB forces in Y direction

$(F_{k1})_Z, (F_{k2})_Z$ = upper and lower MB forces in Z direction

$(F_{k1})_x, (F_{k2})_x$ = upper and lower MB forces in x direction

$(F_{k1})_y, (F_{k2})_y$ = upper and lower MB forces in y direction

$(F_{k1})_z, (F_{k2})_z$ = upper and lower MB forces in z direction

$l_1 (l_2)$ = axial distance between upper (lower) MB and CM of rotor (see [Fig. 2- 3](#))

T_k = torque about O' due to radial MB stiffness

F_k = radial MB force

(3) Unbalance force

The unbalance force relative to the moving frame can be expressed as follows:

$$\{\mathbf{F}_e\}_{xyz} \equiv \begin{Bmatrix} (F_e)_x \\ (F_e)_y \\ (F_e)_z \end{Bmatrix} = \begin{Bmatrix} \bar{m}e\dot{\psi}^2 \cdot \cos(\dot{\psi}t) \\ \bar{m}e\dot{\psi}^2 \cdot \sin(\dot{\psi}t) \\ 0 \end{Bmatrix} \quad (31)$$

By applying the inverse transformation $[DCM]^{-1}$ to $\{\mathbf{F}_e\}_{xyz}$, in the XYZ coordinate system, $\{\mathbf{F}_e\}_{XYZ}$ can be expressed as

$$\{\mathbf{F}_e\}_{XYZ} \equiv \begin{Bmatrix} (F_e)_X \\ (F_e)_Y \\ (F_e)_Z \end{Bmatrix} = [DCM]^{-1} \begin{Bmatrix} (F_e)_x \\ (F_e)_y \\ (F_e)_z \end{Bmatrix} \quad (32)$$

The torque about O' due to unbalance force is then as

$$\mathbf{T}_e = \bar{m}e\dot{\psi}^2 \cdot \sin(\dot{\psi}t) l_e \mathbf{i} - \bar{m}e\dot{\psi}^2 \cdot \cos(\dot{\psi}t) l_e \mathbf{j} \quad (33)$$

where

t = time

\bar{m} = mass unbalance of rotor

l_e = radial distance from the location of mass unbalance of rotor to CM (see Fig. 2- 3).

$(F_e)_x, (F_e)_y, (F_e)_z$ = unbalance force in $x, y,$ and z directions

$(F_e)_X, (F_e)_Y, (F_e)_Z$ = unbalance force in $X, Y,$ and Z directions

\mathbf{T}_e = torque about O' due to mass unbalance

F_e = unbalance force

After performing the derivation of the external forces $\sum F_X$, $\sum F_Y$, and $\sum F_Z$ in equations (3)-(5) and torques $\sum T_x$, $\sum T_y$, and $\sum T_z$ in equations (6)-(8), the total reaction force and torque can be determined by

$$\sum \mathbf{F} = \{\mathbf{F}_3\}_{XYZ} + \{\mathbf{F}_e\}_{XYZ} + \{\mathbf{F}_k\}_{XYZ} \quad (34)$$

$$\sum \mathbf{T} = \{\mathbf{T}_3\}_{xyz} + \{\mathbf{T}_e\}_{xyz} + \{\mathbf{T}_k\}_{xyz} \quad (35)$$

Thus, equations (3)-(8) can be rearranged as the following equation (37) because

$\sum \mathbf{F}$ and $\sum \mathbf{T}$ are all in terms of X_{CM} , Y_{CM} , Z_{CM} , Eulerian angles, and their derivatives.

The demon friction force generated at the contact pivot point leads the system of equations to be highly nonlinear. Particularly, each of the two parameters will be known, only if the other one of them is given. Thus, an iteration procedure was developed by Wang et al. [27] in order to determine these two parameters.

It is not difficult to reduce the above second-order differential equations to a set of coupled first-order differential equations by defining a set of new variables, q_1, q_2, \dots , and q_{12} , and they are defined as follows.

$$\begin{Bmatrix} X_{CM} \\ Y_{CM} \\ Z_{CM} \\ \theta \\ \phi \\ \psi \\ \dot{X}_{CM} \\ \dot{Y}_{CM} \\ \dot{Z}_{CM} \\ \dot{\theta} \\ \dot{\phi} \\ \dot{\psi} \end{Bmatrix} \equiv \begin{Bmatrix} q_1 \\ q_2 \\ q_3 \\ q_4 \\ q_5 \\ q_6 \\ q_7 \\ q_8 \\ q_9 \\ q_{10} \\ q_{11} \\ q_{12} \end{Bmatrix} \quad (36)$$

It follows that

$$\{Q(t)\}_{12 \times 1} = \begin{Bmatrix} \dot{X}_{CM} \\ \dot{Y}_{CM} \\ \dot{Z}_{CM} \\ \dot{\theta} \\ \dot{\phi} \\ \dot{\psi} \\ \ddot{X}_{CM} \\ \ddot{Y}_{CM} \\ \ddot{Z}_{CM} \\ \ddot{\theta} \\ \ddot{\phi} \\ \ddot{\psi} \end{Bmatrix} = \begin{Bmatrix} \cdot \\ q_1 \\ \cdot \\ q_2 \\ \cdot \\ q_3 \\ \cdot \\ q_4 \\ \cdot \\ q_5 \\ \cdot \\ q_6 \\ \cdot \\ q_7 \\ \cdot \\ q_8 \\ \cdot \\ q_9 \\ \cdot \\ q_{10} \\ \cdot \\ q_{11} \\ \cdot \\ q_{12} \end{Bmatrix} = \begin{Bmatrix} q_7 \\ q_8 \\ q_9 \\ q_{10} \\ q_{11} \\ q_{12} \\ y_1(t, q_1, q_2, q_3, q_4, q_5, q_6, q_7, q_8, q_9, q_{10}, q_{11}, q_{12}) \\ y_2(t, q_1, q_2, q_3, q_4, q_5, q_6, q_7, q_8, q_9, q_{10}, q_{11}, q_{12}) \\ y_3(t, q_1, q_2, q_3, q_4, q_5, q_6, q_7, q_8, q_9, q_{10}, q_{11}, q_{12}) \\ y_4(t, q_1, q_2, q_3, q_4, q_5, q_6, q_7, q_8, q_9, q_{10}, q_{11}, q_{12}) \\ y_5(t, q_1, q_2, q_3, q_4, q_5, q_6, q_7, q_8, q_9, q_{10}, q_{11}, q_{12}) \\ y_6(t, q_1, q_2, q_3, q_4, q_5, q_6, q_7, q_8, q_9, q_{10}, q_{11}, q_{12}) \end{Bmatrix} = \{Y(t, q_n)\}_{12 \times 1} \quad (37)$$

Referring to the fourth-order Runge-Kutta formula, the RK4 approximation of $\{Q(t_{i+1})\}$

can be given by the following equations:

$$\{Q(t_{i+1})\} \approx \{Q(t_i)\} + \frac{1}{6} (\{K_1\} + 2\{K_2\} + 2\{K_3\} + \{K_4\}) \quad (38)$$

$$t_{i+1} = t_i + \Delta t \quad (39)$$

where

$$\{K_1\} = \Delta t \{Y(t_i, q_n(t_i))\} \quad (40)$$

$$\{K_2\} = \Delta t \left\{ Y \left(t_i + \frac{\Delta t}{2}, q_n(t_i) + \frac{1}{2} \{K_1\} \right) \right\} \quad (41)$$

$$\{K_3\} = \Delta t \left\{ Y \left(t_i + \frac{\Delta t}{2}, q_n(t_i) + \frac{1}{2} \{K_2\} \right) \right\} \quad (42)$$

$$\{K_4\} = \Delta t \left\{ Y \left(t_i + \Delta t, q_n(t_i) + \frac{1}{2} \{K_3\} \right) \right\} \quad (43)$$

where subscript i and Δt are the time at i -th instant and step size of time increment, respectively. Thus, the next value $\{Q(t_{i+1})\}$ is determined by the current value $\{Q(t_i)\}$ plus the product of the interval Δt and an calculated slope $\frac{1}{6}(\{K_1\} + 2\{K_2\} + 2\{K_3\} + \{K_4\})$.

To investigate the dynamic characteristics of the MB motor, a physical model of the MB is used. Each of the MBs is represented in terms of stiffness and damping coefficients k and c . In order to simplify the model, the cross-coupled stiffness coefficients are ignored. The modeling parameters for solving the ordinary differential equations mentioned above are listed in [Table 2- 1](#).

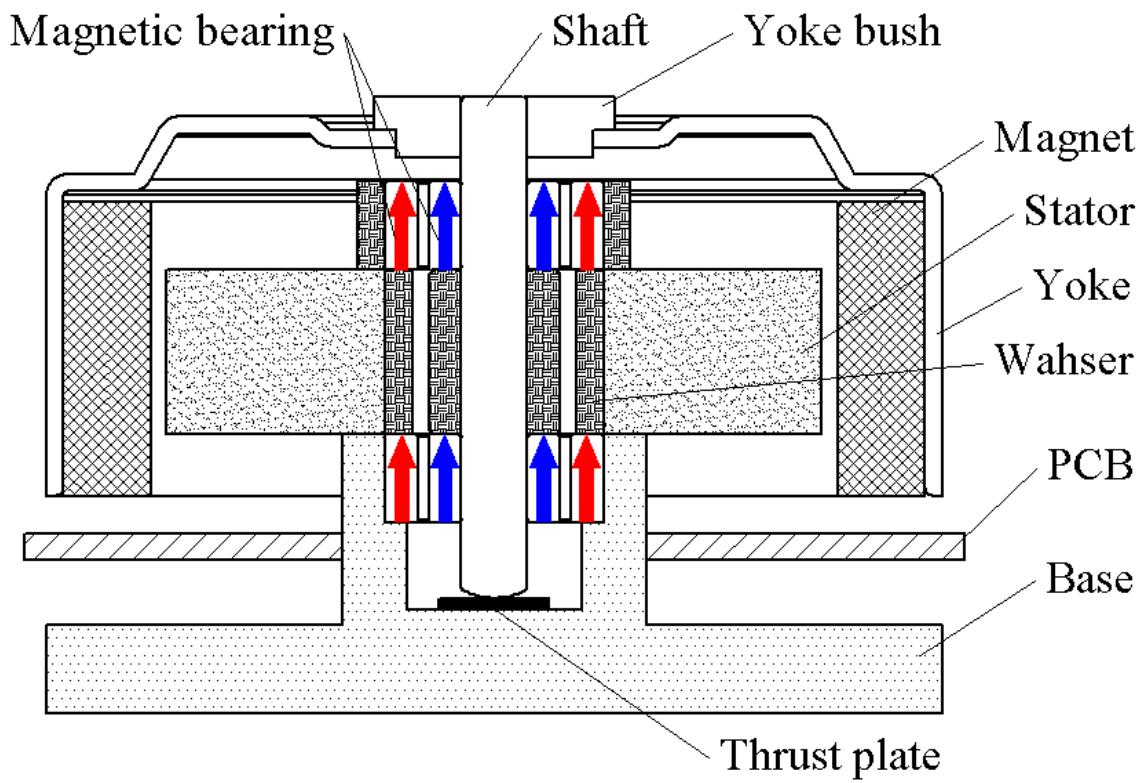
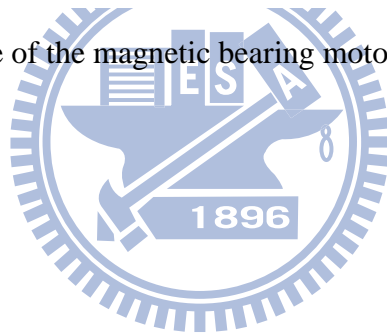


Fig. 2- 1 Schematic structure of the magnetic bearing motor.



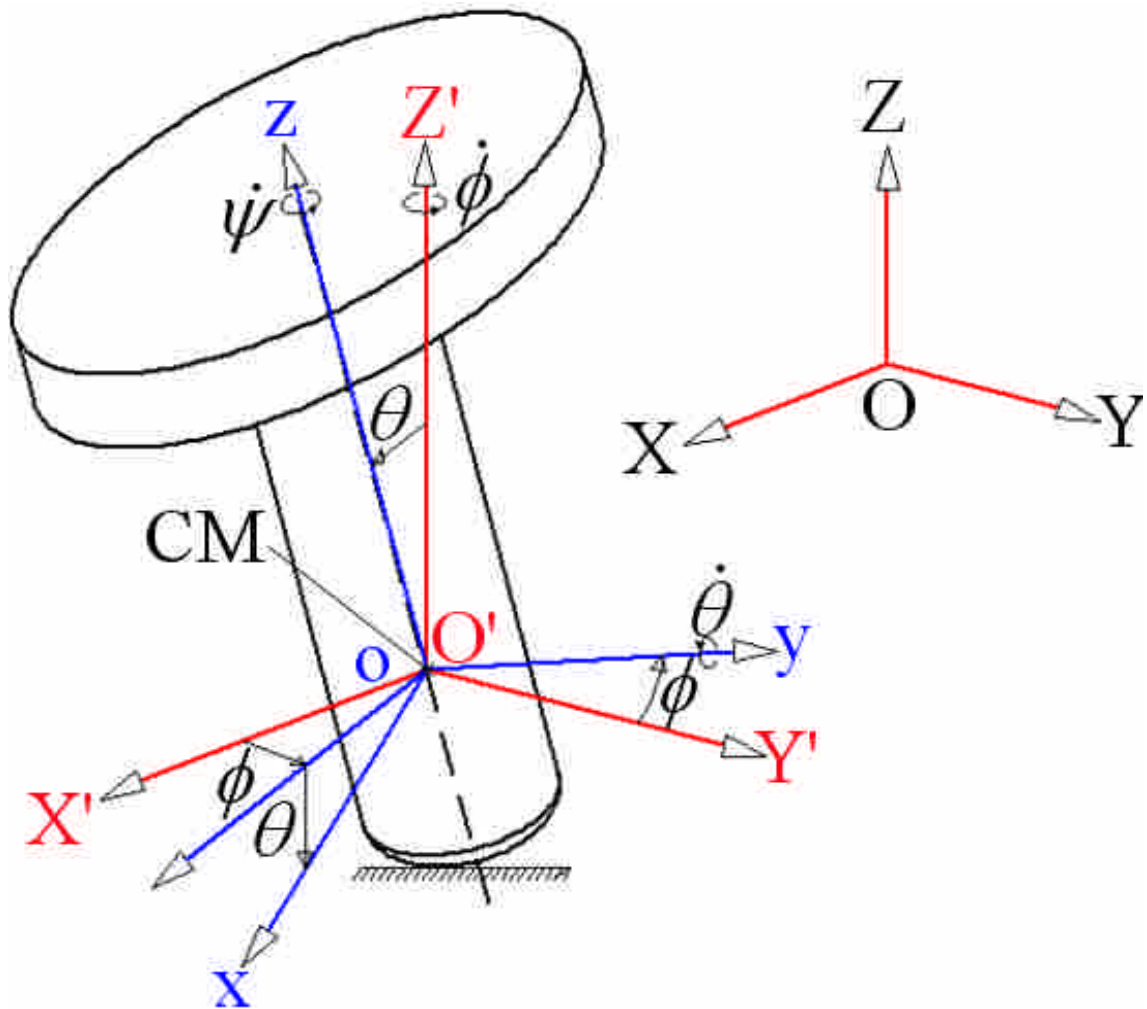


Fig. 2- 2 Frames of reference.

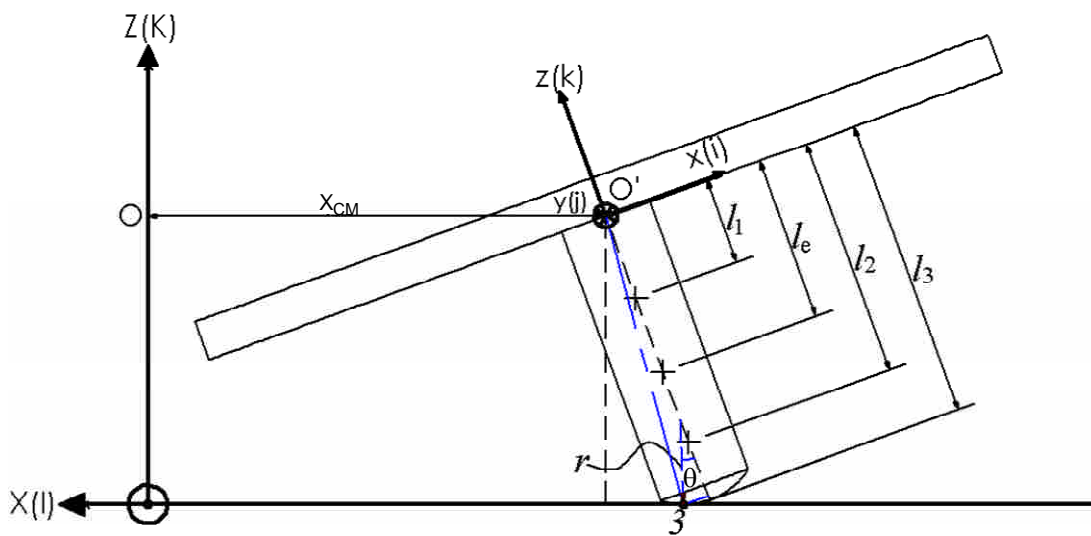


Fig. 2- 3 Geometry of the rotor

Table 2- 1 Parameters of the MB motor

Rotor mass, (kg)	0.071
Polar moment inertia, (kg·m ²)	2.092×10 ⁻⁵
Transverse moment of inertia, (kg·m ²)	1.254×10 ⁻⁵
Rotational speed of rotor, (Hz)	60.5
Friction coefficient thrust plate, (-)	0.01
Axial preload force, (N)	1.887
Clearance, (m)	5×10 ⁻⁴
Radial stiffness of MB, (N/m)	1548
Damping coefficient of MB, (N·s/m)	0
Damping ratio of the system, (-)	0.0655
Mass unbalance of rotor, (kg·m)	0.10×10 ⁻⁵

2.2 Procedures for prototyping the MB

As described in section 2.1, the mentioned MB prototype has been carried out using a developed procedure which will be thoroughly addressed in the following.

Finite element analysis was used to analyze the magnetic force of the magnetic bearing motor. To design a stable magnetic bearing motor system, there are three terms should be considered.

First, in the static state, the system should be stabilized in all axes when the rotor is tilted at a critical angle defined as Θ along the x -axis. Due to the geometry constraints of the radial air gap is 500 μm and the desired radial run-out should be smaller than 75 μm (peak). The force analysis is considered, in the critical condition when the Θ is equal to 1° shown as Fig. 2- 4(b).

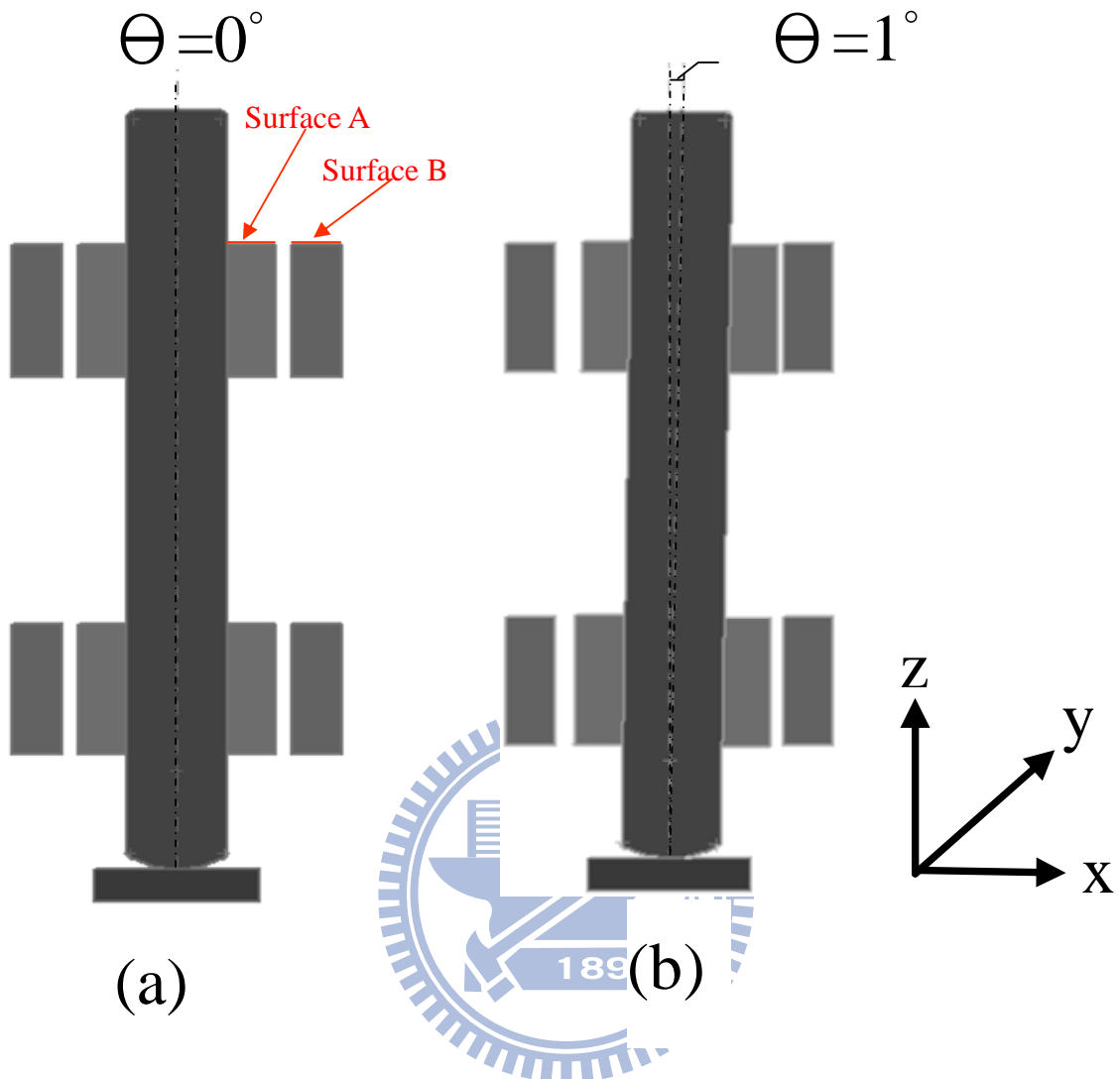


Fig. 2- 4 (a) Rotor is tilted at a critical angle 0° about positive x -axis. (b) Rotor is tilted at a critical angle 1° about positive x -axis.

The restoring torque about y -axis was defined as T_y and the axial force was defined as F_z . The 3D full model of the finite element analysis was constructed to compute these parameters, as shown in Fig. 2- 4. For each variation of the axial displacement defined as D_{zz} (When the surface A of the inner annular magnet is lower than the surface B of the outer one along the positive z -axis, it was specified with $D_{zz} > 0$) of inner and outer magnetic annular rings, the rotor was rotated 1° about the y -axis. Then T_y and F_z were calculated and shown as Table 2- 2. It was clear that the state of the system with $0 \leq D_{zz} \leq 3 \times 10^{-4}$ m was stable.

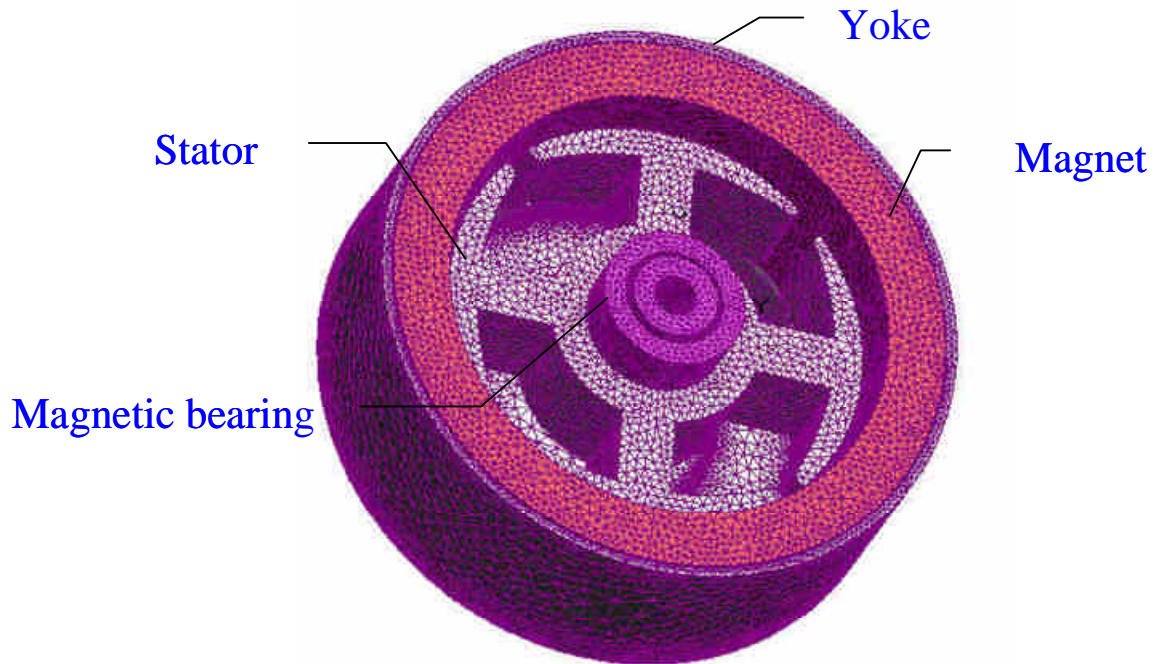


Fig. 2- 5 3D solid model mesh of the magnetic bearing motor.



Table 2- 2 T_y and F_z versus various D_{zz} .

D_{zz} (10^{-5} m)	T_y (Nm)	F_z (N)	State
- 10	- 0.01658	2.420	Unstable
0	- 0.01525	- 1.997	Stable
10	- 0.01219	- 4.086	Stable
20	- 0.00788	- 5.719	Stable
30	- 0.00487	- 7.070	Stable

Secondly, in the dynamic state, the system should be stabilized in all axes when the rotor is loading the unbalance 9.8×10^{-6} Nm, rotated in the rated speed 3840 rpm and the centrifugal force 0.1617N is generated. For supporting the dynamic load (0.1617N), the

radial magnetic force is considered two times as it. That is equivalent to 0.3234N. The target of the radial run-out was supposed to be lower than 150 μm (peak to peak) in this prototype. To achieve the stable zone of D_{zz} , whenever the radial displacement was greater than 75 μm , the radial force must be greater than 0.3234 N. Approach to this computation of radial force of the development system, the stator was fixed and the rotor was shifted along the positive x -axis as the following five different positions, 0, 1×10^{-4} m, 2×10^{-4} m, 3×10^{-4} m, 4×10^{-4} m and 4.9×10^{-4} m for each D_{zz} . Three relative positions of magnetic inner and outer ring were shown as Fig. 2- 5, in which Fig. 2- 5 (a-1) showed the radial displacement of the rotor along positive x -axis was 0. Fig. 2- 5 (a-2) showed the displacement of the rotor along positive x -axis was 3×10^{-4} m. And Fig. 2- 5 (a-3) showed the radial displacement of the rotor along positive x -axis was 4.9×10^{-4} m.

From these locations, arrangement of the rotor and stator, the radial force could be obtained as a function of the radial displacement during the force calculation. In order to analyze the radial force as a function of radial displacement at various D_{zz} values, the variation of D_{zz} is chosen as follows 0, 1×10^{-4} m, 2×10^{-4} m, 3×10^{-4} m, and 4×10^{-4} m. And its 3D structure distribution at $D_{zz} = 0$ was shown as Fig. 2- 6, in which, ①, ②, ③ and ④ showed upper magnetic outer ring, lower magnetic outer ring, upper magnetic inner ring, lower magnetic inner ring, respectively. The rotor was shifted along negative

axis. Both in Fig. 2- 5 and Fig. 2- 6 only the magnetic inner and outer rings were demonstrated.

Both radial force and axial force were known, and then the stiffness of the magnetic bearing is perfectly determined. Because of the axial symmetry and the magnetic bearings made exclusively of permanent magnets, the axial stiffness is twice as radial stiffness according to Earnshaw's theorem [7].

After computations were performed, we found the value of radial force for each radial displacement. And the radial force as a function of D_{zz} could be obtained. Also, use the same process for F_z as a function of radial displacement was calculated. The final results were presented in Fig. 2- 8 (a) and Fig. 2- 8 (b). Fig. 2- 8 (a) shows the radial force as a function of radial displacement of the rotor. The radial force is linearly proportional to radial displacement at $D_{zz} = 0$. Also as the $D_{zz} = 1 \times 10^{-4}$ m, 2×10^{-4} m, 3×10^{-4} m, and 4×10^{-4} m, the radial force versus radial displacement have the same characteristic, except the radial displacement is greater than 4×10^{-4} m. Graphically the equation $F_r = - 0.3234$ N and radial displacement = $75 \mu\text{m}$ give two lines A and B, as shown in Fig. 2- 8 (a). It is manifest that in the fourth quadrant of line A crosses line B, the F_r is greater than the rated load whenever the radial displacement is greater than $75 \mu\text{m}$. From the data analysis of radial force and the results of Table 2- 2, it indicates that the stable zone of D_{zz} is between 0 and 3×10^{-4} m. The rotor can be levitated in the radial

direction without any frictional contact when the radial run-out (peak to peak) is less than $150\ \mu\text{m}$. Fig. 2- 8 (b) shows the axial force as a function of radial displacement of rotor. The number of axial force at $D_{zz} = 0$ was around zero from radial displacement = 0 to 4.9×10^{-4} m. For a fixed value of D_{zz} , the axial force rose slowly in the same radial displacement scope. For a fixed value of radial displacement of rotor, the axial force increased with increasing D_{zz} . The axial force of the magnetic bearing motor with radial displacement = 4.9×10^{-4} m increase from 0 N for $D_{zz} = 0$ to $- 6.543$ N for $D_{zz} = 4 \times 10^{-4}$ m.

Thirdly, the axial force of the development system should be controlled under a proper value. The upper limit of this scope could be decided by two constraints. One is the friction torque produced by the MB system in the dynamic state has to smaller than the ball bearing one. The other is the capacity of the thrust plate, with loading capacity defined as P , which must be smaller than $10000\ \text{kg/m}^2$, the maximum speed defined as V , which must be smaller than $7\ \text{m/sec}$, and the capacity of $P \times V$ value must be smaller than $1000\ \text{kg}/(\text{m} \cdot \text{sec})$ (The coefficient of kinetic friction 0.08). Referring to the friction loss of ball bearing type spindle motor as shown in Fig. 2- 9, the cross points were the data of measurement. After curve fitting of these data points the friction equation was obtained. And it shows that friction torque is $4.209 \times 10^{-4}\ \text{Nm}$ at the speed $3840\ \text{rpm}$. Then the upper limit of the axial load is equal to $10.388\ \text{N}$.

Suppose one third in diameter of shaft is contacted with the thrust plate. Then the V is $0.2037\ \text{m/sec}$ and the upper limit of magnetic bearing axial force is $7.904\ \text{N}$. From the results of calculated value, it follows that the final limit value of the axial force should be controlled smaller than $7.904\ \text{N}$. It shows that in the stable zone of D_{zz} mentioned

above, the development system has the lower friction than the ball bearing type one.

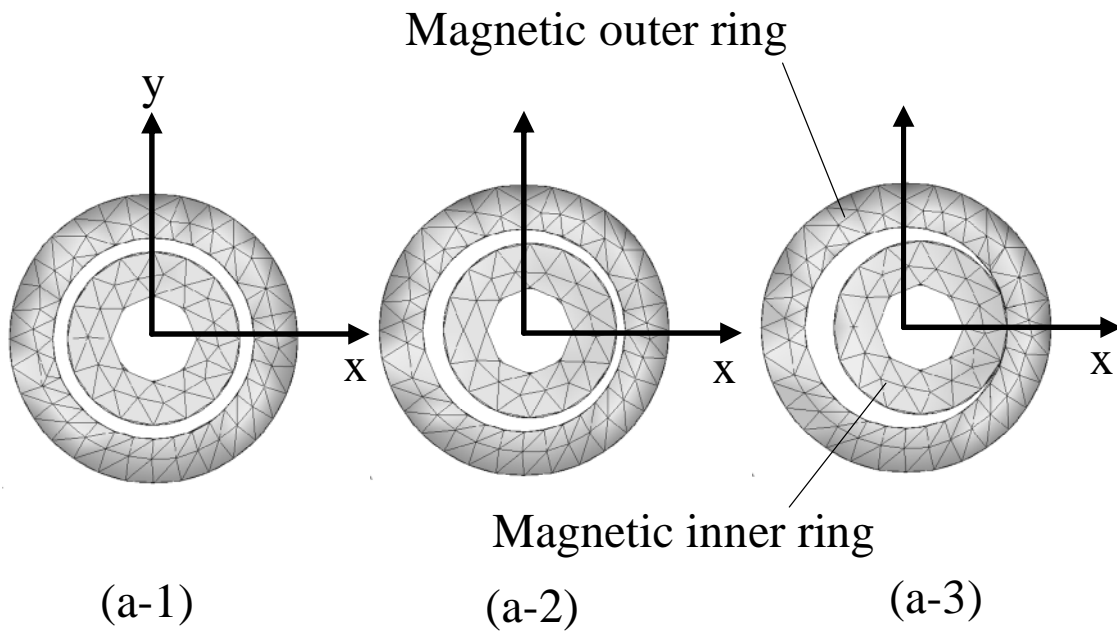


Fig. 2- 6 2D top view of relative location of the rotor and stator.



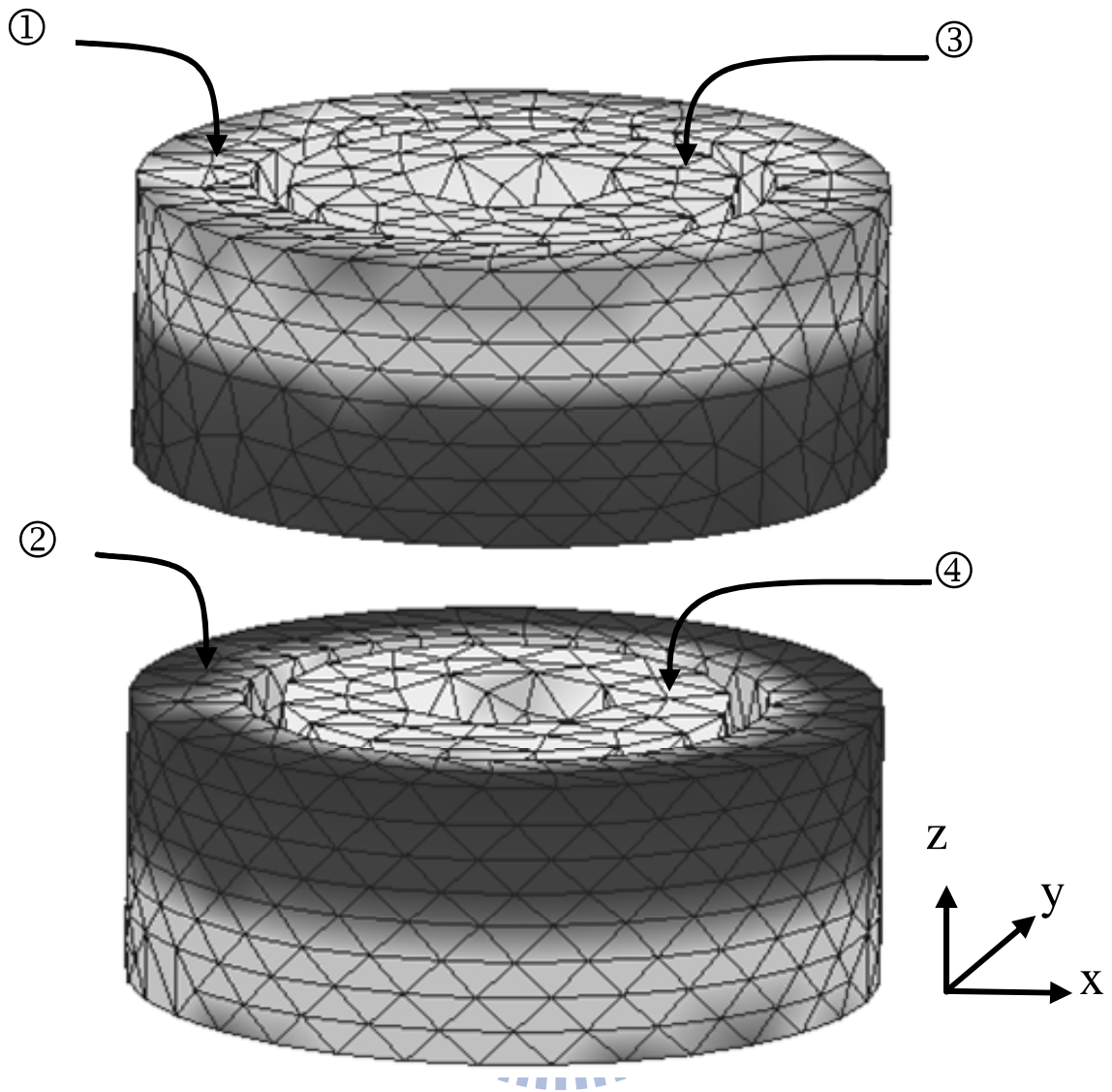


Fig. 2- 7 3D distribution of rotor and stator.

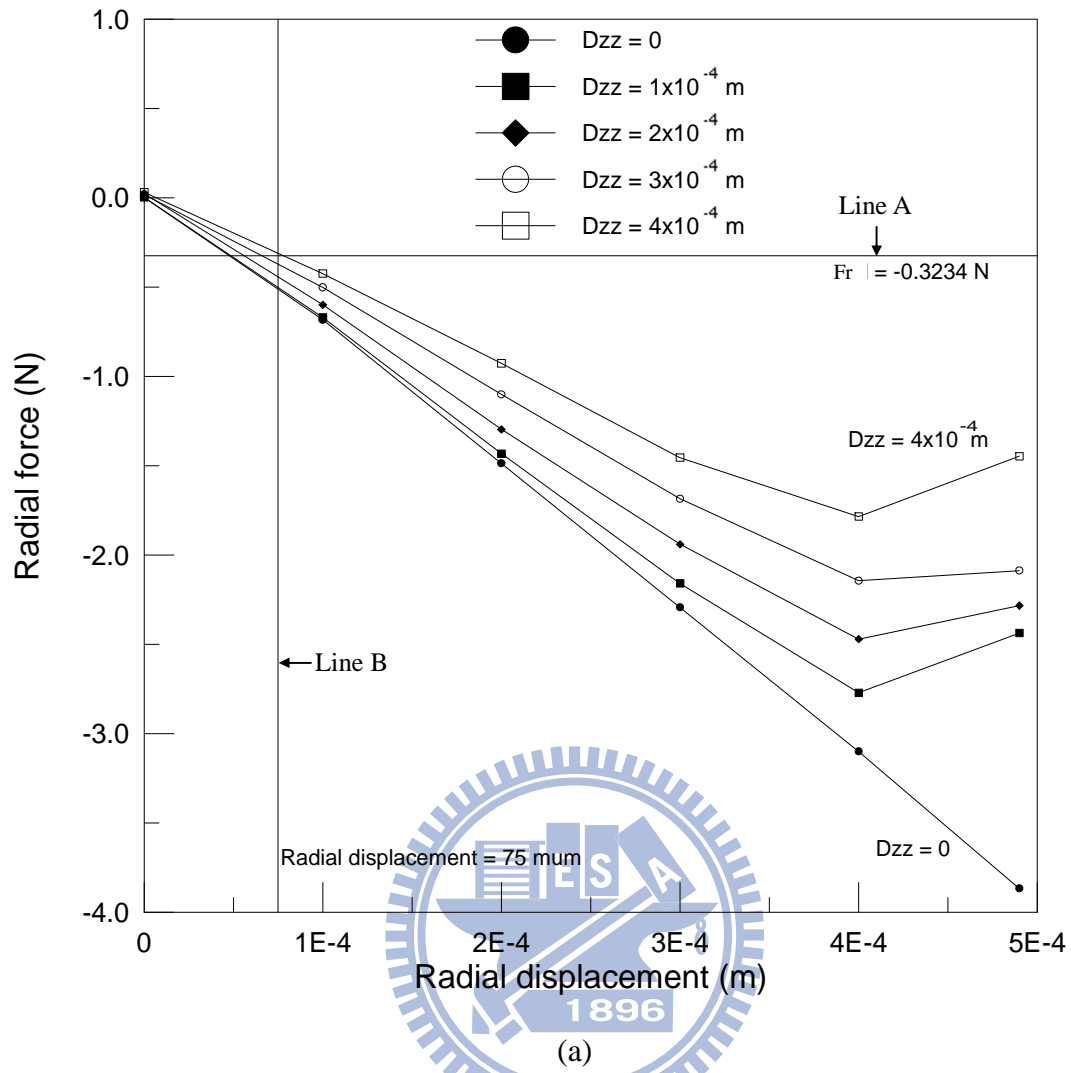
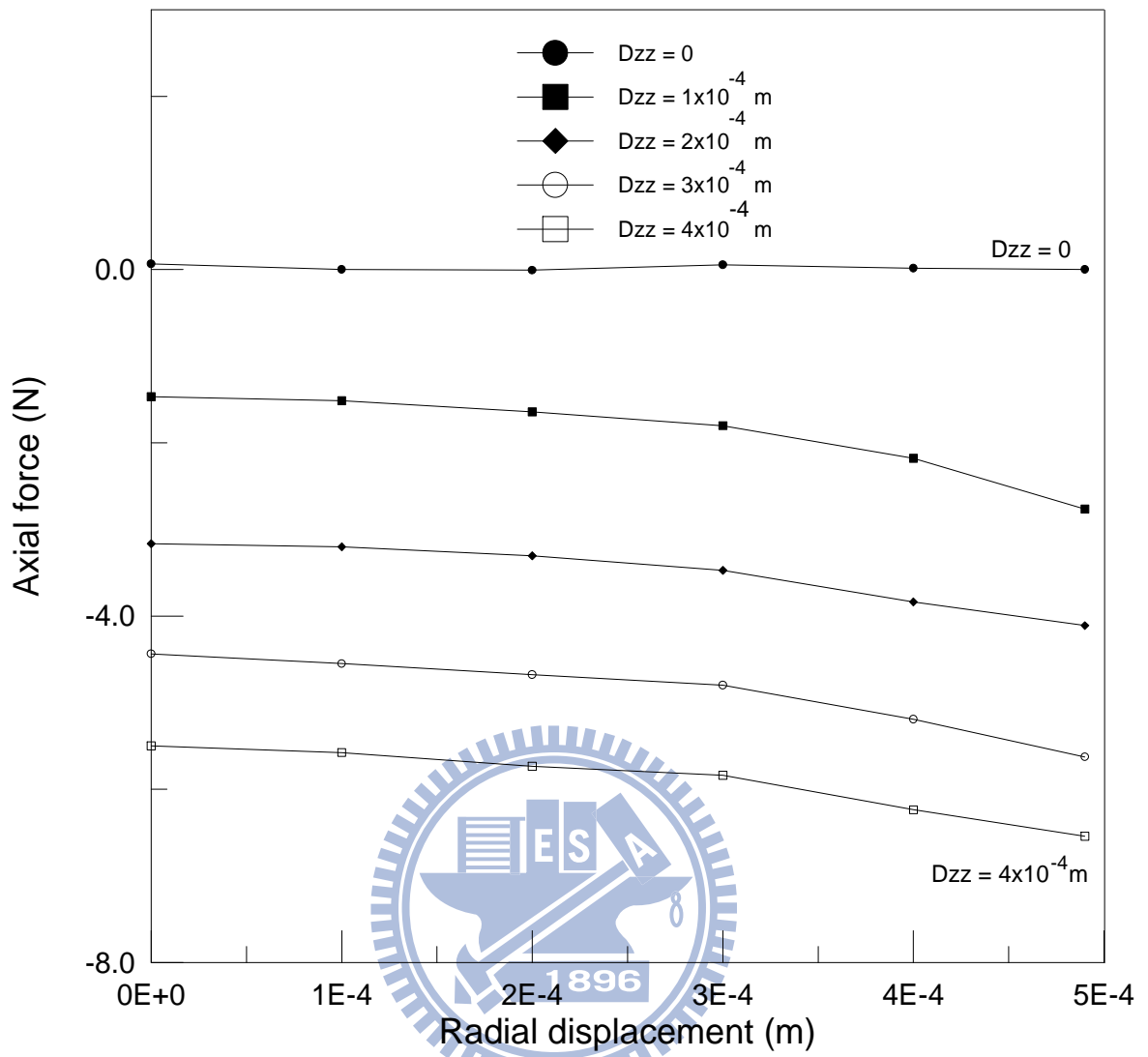


Fig. 2- 8 (a) Simulated radial force as a function of radial displacement of rotor. (b) The axial force as a function of radial displacement of rotor.



(b)

(Continued).

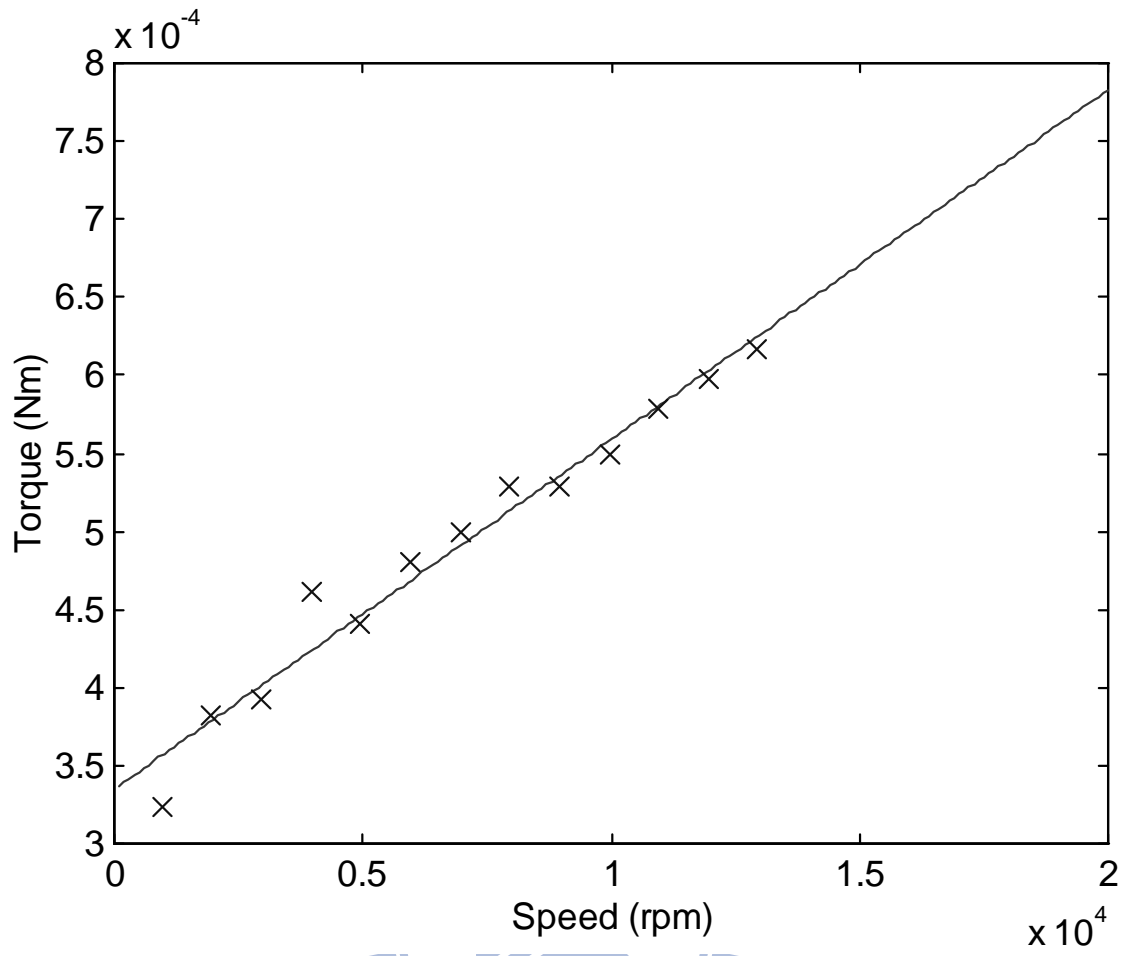
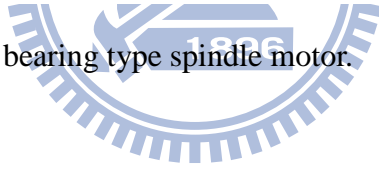


Fig. 2- 9 Friction loss of ball bearing type spindle motor.



2.3 Experiment

An accelerometer with a resolution of 1.6×10^{-4} G was attached to the rotor in the radial direction while an impulse shock was given to initiate free vibration of the rotor, and the time response of the rotor vibration was detected and recorded. The corresponding frequency spectrum of the radial runout (RRO) can be determined by fast Fourier transform (FFT). Accordingly, the damping ratio ζ was experimentally determined using the general formulation $\zeta = \delta / (\omega_n \tau_d)$, where δ is the logarithmic decrement, the definition of which is the ratio of any two successive amplitude peak values of the response curve in the time domain; τ_d is the time between these two peaks; and ω_n is the natural frequency of the rotor. In addition, the natural frequency of the rotor can be identified from the mentioned frequency spectrum curve of the rotor; this frequency was also confirmed by implementing the well known sine sweep method. Since an infinitesimal motion is imposed on the rotor, it is believed that the system can be approximated as a one-dimensional force free oscillation of a second-order model. Thus, it is possible to calculate the unknown parameters of the system: $c_c = 2m\omega_n$, the critical damping coefficient; $c = \zeta c_c$, the damping coefficient; and $k = m\omega_n^2$, the radial stiffness coefficient of the MB. While the motor was spun at the desired speed, a high-accuracy laser displacement sensor with a resolution of $0.5 \mu\text{m}$ was used to measure the RRO. The testing plan was constructed shown as [Fig. 2- 10](#). The laser beam,

emitted from the transmitter and reflected by the surface of the yoke bush, was received by the detector, and the signal was processed by a spectrum analyzer which was connected to the testing circuit. A personal computer (PC) was connected to both the driver of the laser sensor and the spectrum analyzer in order to completing the post-processing of the signals. Thus, the evolution of the responses in the time and frequency domains was collected and recorded.

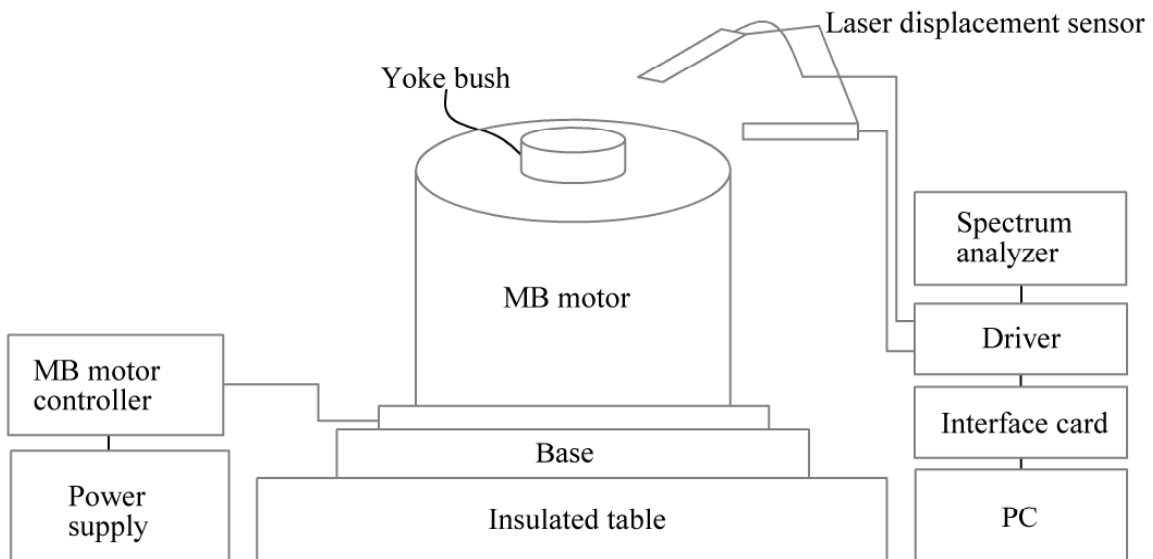


Fig. 2- 10 Sketch of test rig for the measurement of RRO

2.4 Results and discussion

Fig. 2- 11 shows the free oscillation motion of the rotor, of which the time and frequency spectrum of the radial vibration is demonstrated. From the calculation, it can be seen that the radial stiffness and the damping ratio of the system and the natural

frequency of the rotor are 1548 N/m, 0.0655 and 23.5 Hz, respectively. Fig. 2- 12 displays the experimental curve for the RRO measurement in the time and frequency domains. Comparing the results of Fig. 2- 12 (a) and Fig. 2- 12 (b), the simulated RRO of 56 μm has a good agreement with the experimental one of 60 μm . In addition, the spectral analysis of the RRO of the yoke bush, the magnitude of which is dominated by the 1X component, where X (60.5 Hz) designates the rotational frequency of the motor, and the primary 1X RRO harmonic in magnitude indicate that the mass unbalance of the rotor is the main contributor to the RRO because the force profile of the unbalance repeats every revolution; nevertheless, it can be found that 2X and 3X amplitudes exist in the experimental frequency spectrum curve. Since the ratio of pole number to slot number of the designed motor is 4:4, these frequency components could be seen as resulting from the unbalanced magnetic force [28]-[29], which is not considered in the proposed model. By considering the parameters of the MB motor listed in Table I, the differential equations can be numerically solved by the developed computer code. The corresponding three-dimensional trajectories of the rotor under three different rotational speeds, 3000, 4500, and 6000 rpm, are shown in Fig. 2- 13, in which the top and bottom loci are the locations of the yoke bush and shaft bottom, respectively; the related RROs for the yoke bush are 64, 51, and 47 μm , respectively. After the coordinate transformation between the body and fixed coordinates is performed, the 3D trajectory

can be generated, demonstrating that the working mode of the dynamic rotor is in cylindrical in nature. It is clear that both the RROs of the shaft bottom and the yoke bush are close to each other for each trajectory, meaning that there is no contact between the rotor and the stator; furthermore, an increased rotational speed results in a decreased RRO, suggesting that the gyroscopic effect is active; also, this effect is experimentally observed.

Mass unbalance caused by the rotor's centre of mass not coinciding with the centre of rotation will lead to the most common unbalance force, which is in the form of centrifugal force, and the magnitude of this force will increase by the square of rotation speed of a rotor multiplies the rotor mass unbalance. Fig. 2- 14 shows simulation results of the mass unbalance effect, while the motor was spun at the speed of 3000 rpm with a mass unbalance of the rotor 0.1×10^{-5} kg-m, and other parameters of the motor are shown as Table I. Fig. 2- 14 (a) represents the RRO of radial surface (see Fig. 2- 10) of the yoke bush along X and Y axes, and Fig. 2- 14 (b) shows the corresponding 3D loci of the dynamic rotor. The RRO_X and RRO_Y designate the RRO along X and Y axes, respectively, i.e., $RRO = [(RRO_X)^2 + (RRO_Y)^2]^{0.5}$. The RRO in time and frequency domains with regards to Fig. 2- 14 (a) are demonstrated in Fig. 2- 14 (c) and Fig. 2- 14 (d), respectively. Obviously, the amplitude of the RRO is sensitively affected by the magnitude of 1X RRO harmonic, i.e., the mass unbalance is the main contribution to the

RRO. The comparison of simulated different mass unbalance 0.1×10^{-5} , 0.2×10^{-5} , and 0.3×10^{-5} kg·m at the rotation speed of 3000 rpm are represented in Fig. 2- 15. While the above mentioned mass unbalances were applied to the rotor, the RROs of the yoke bush are 40.2, 87.4, and 134.0 μm , respectively. The RRO is roughly proportional to the mass unbalance, and this reveals that the validation the proposed model.

Fig. 2- 16 shows the comparison of the friction torque for the proposed MB and conventional ball bearing motors. For examination of the torque loss due to these two bearing types, without altering the mechanical, magnetic, and electrical properties of the motor, the MB was replaced with two conventional ball bearings, and the friction torque was measured by a torque meter.

The torque meter with maximum capacity of 5×10^{-3} Nm and an accuracy of 10^{-5} Nm was used to measure the friction torque loss of magnetic motor and ball bearing motor.

The method of measuring friction torque loss generated by the objective motor was that the motor's rotor was coupled to the shaft of the torque meter, then the motor was rotated by the torque meter to the expected four speeds 3000, 4000, 5000 and 6000 rpm. The torque loss caused by un-centering of the coupling had to be accounted. And the friction torque loss as a function of the speed was obtained.

The torque losses of both motor types linearly increase with respect to the increased rotational speed of the spindle; nevertheless, the MB motor exhibits a lower friction

torque.

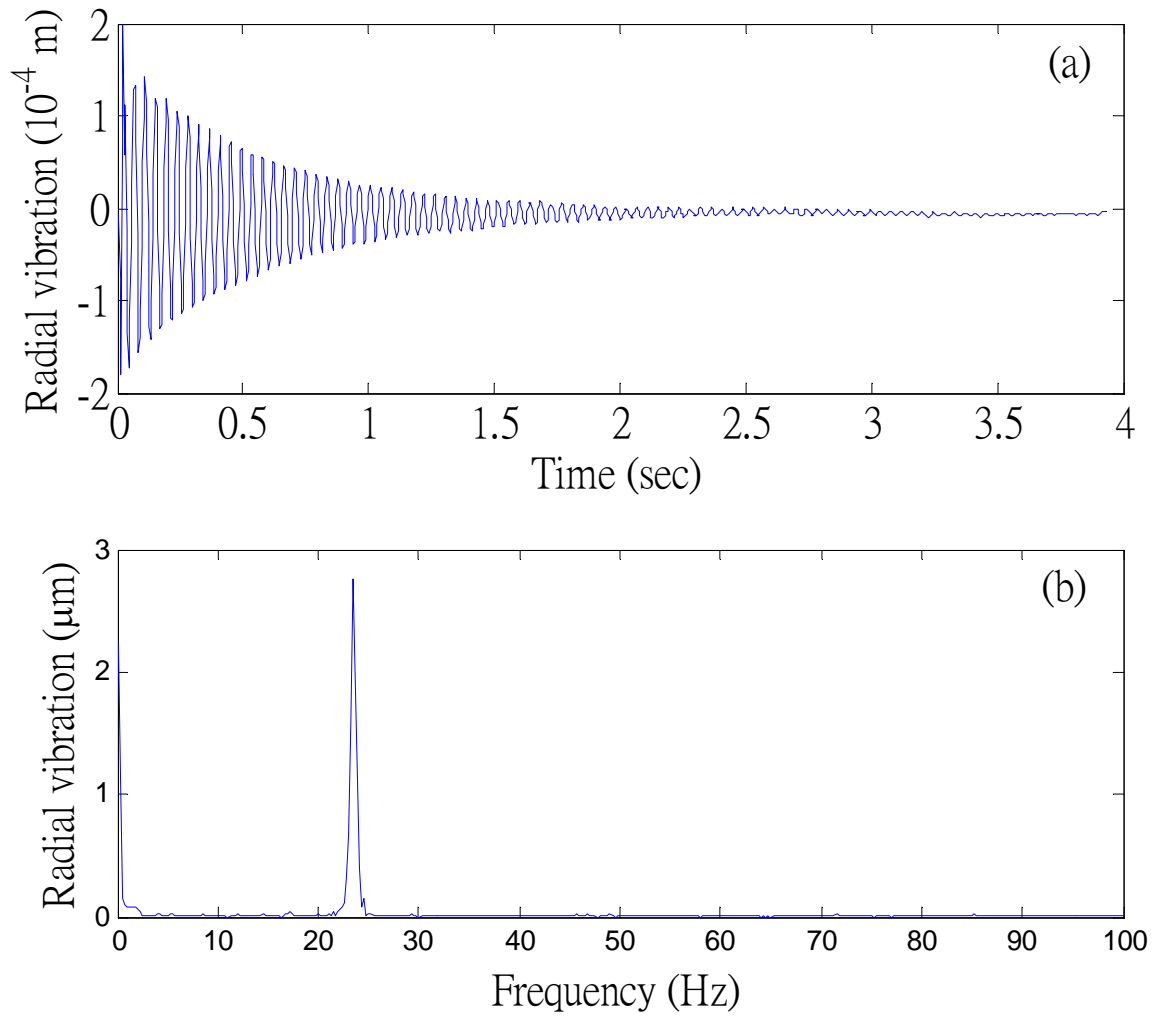


Fig. 2- 11 Force free response of the rotor in (a) time and (b) frequency domains.

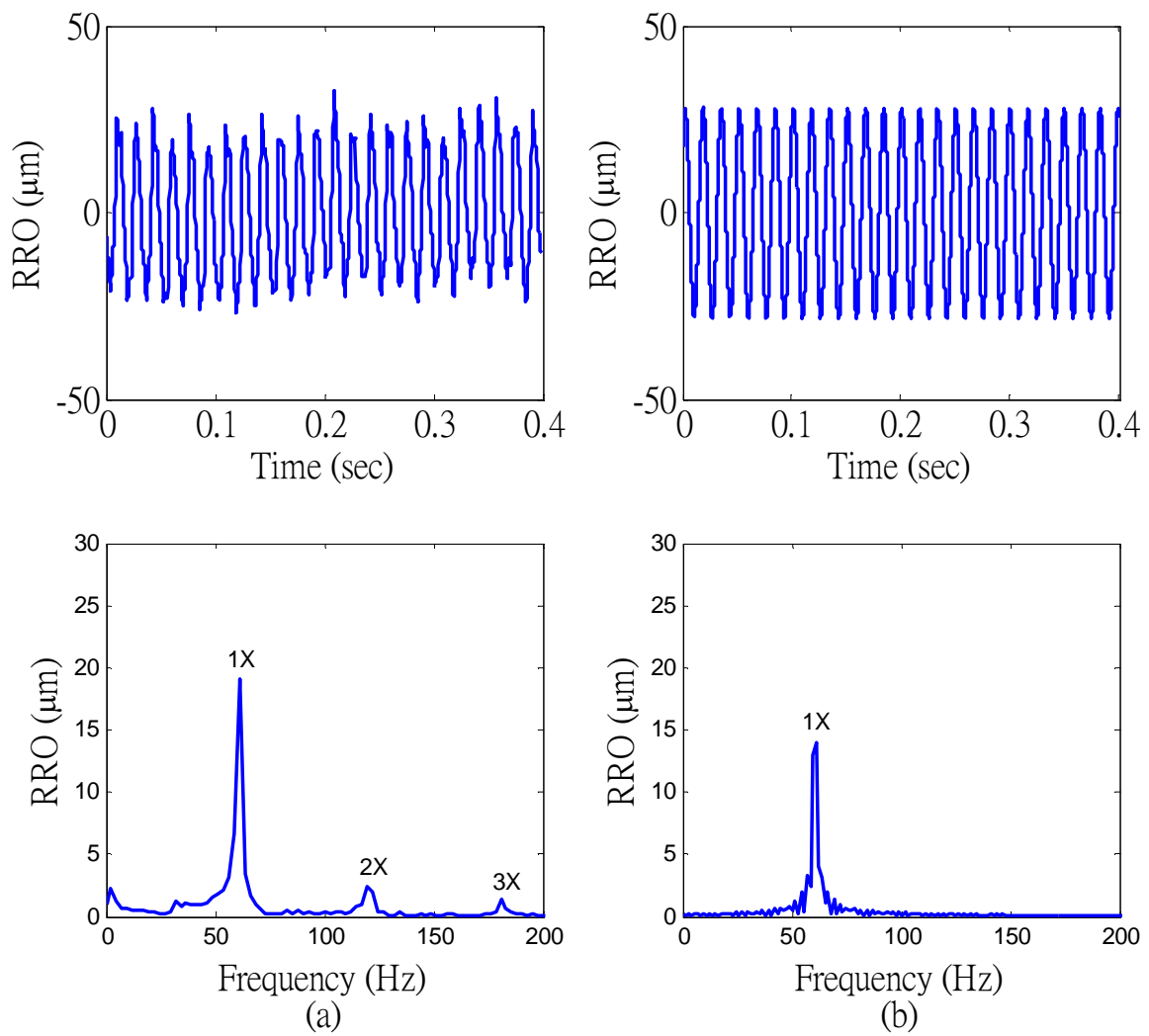


Fig. 2- 12 (a) Experimental and (b) simulated time response and frequency spectrum of RRO.

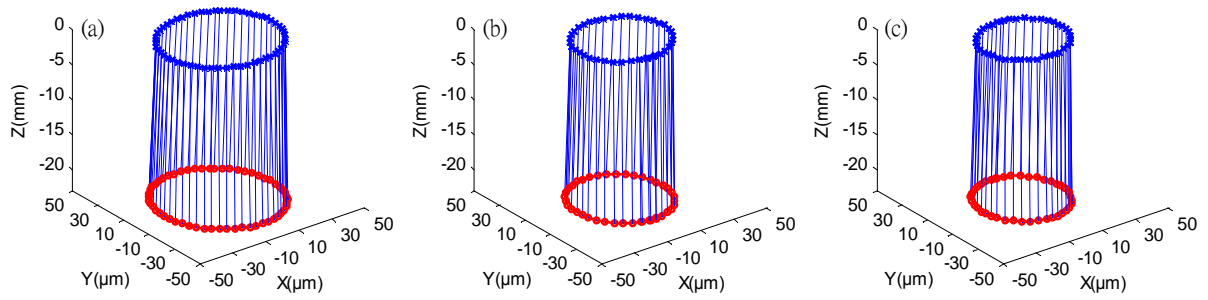


Fig. 2- 13 Simulated three dimensional trajectories of the rotor under the rotational speeds of (a) 3000, (b) 4500, and (c) 6000 rpm.

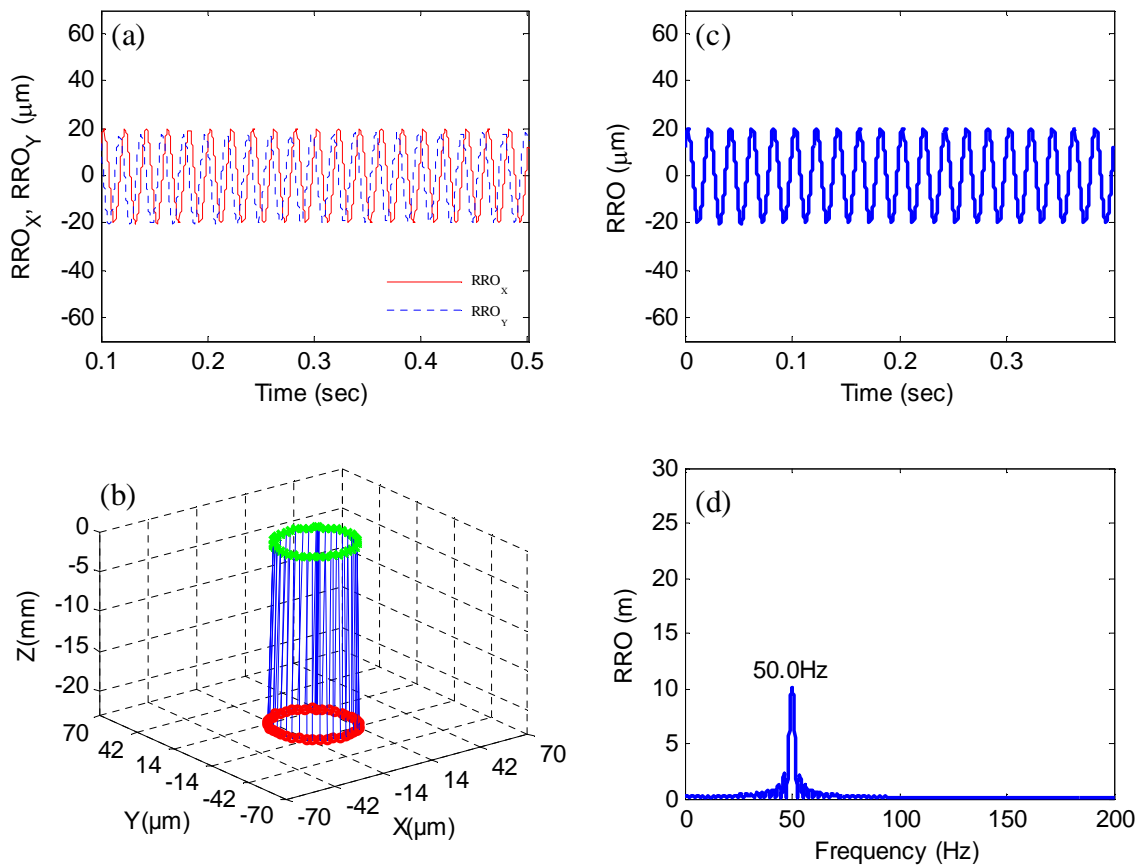


Fig. 2- 14 Simulated RRO excited by mass unbalance: (a) RRO_x and RRO_y ; (b) 3D trajectory of the rotor; (c) time response of RRO; (d) frequency spectrum of RRO.

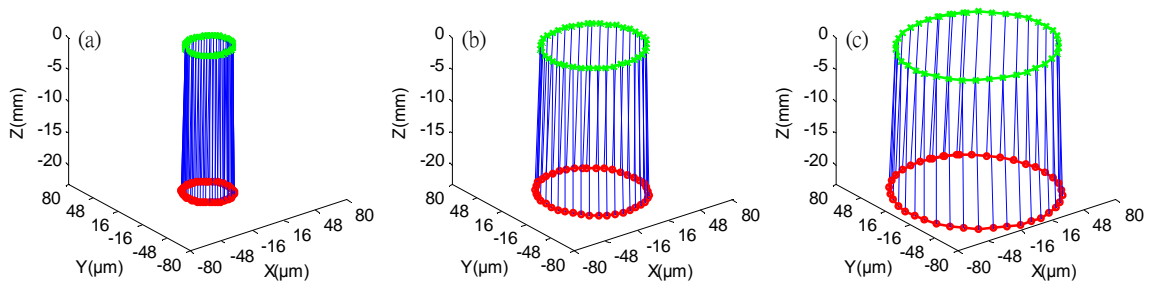


Fig. 2- 15 Simulated three dimensional trajectories of the rotor with the mass unbalances: (a) 0.1×10^{-5} kg·m, (b) 0.2×10^{-5} kg·m, and (c) 0.3×10^{-5} kg·m under the rotational speed of 3000 rpm.

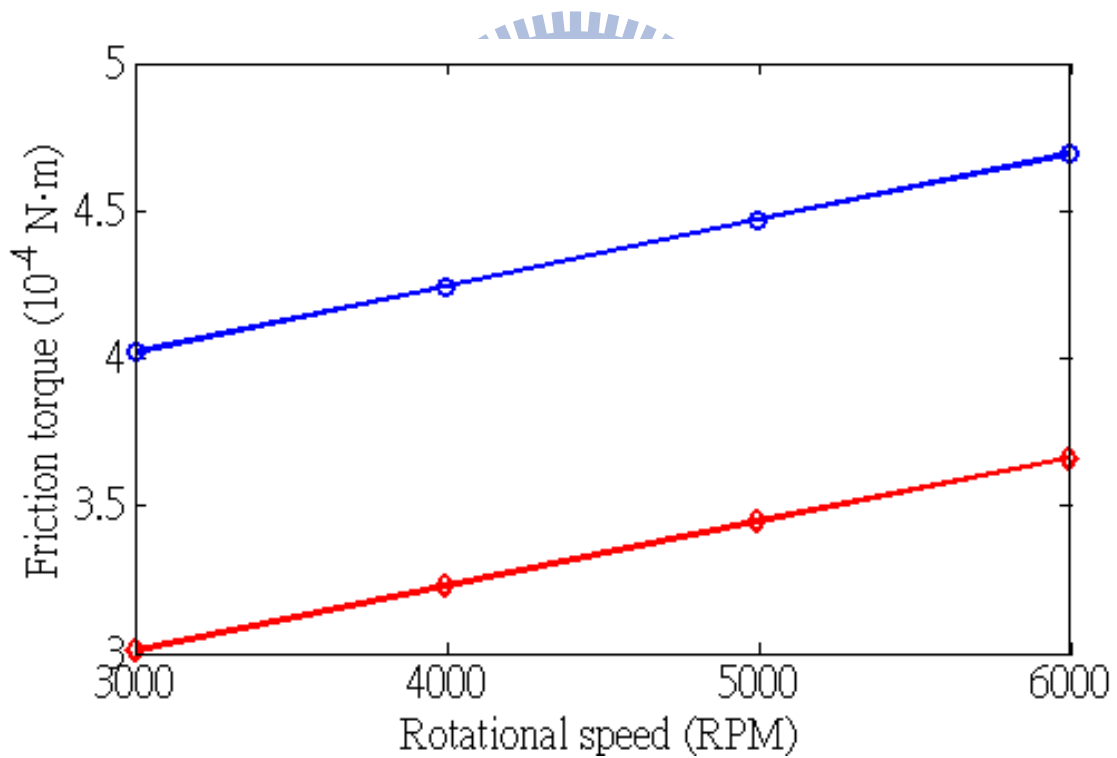


Fig. 2- 16 Comparison of friction torque of Ball bearing and MB motors.

Chapter 3

Damping effect

3.1 Introduction

Passive MBs is one of the solutions to achieve low noise and long life span of the spindle motors that are applied in the data storage disk drives such as HDD and DVD devices. Few researchers have taken into account the effects due to motor design, and treated both the MB and motor as a whole system when developing the MBs [30]-[33]. For example, the magnetic flux density resulting from the permanent magnet of the motor may couple with the MB's one. However, the magnetic bearing system has a disadvantage that is a lack of damping. Therefore, in the spindle motor systems which support on these bearings can be expected likewise to show very small damping. This condition is revealed by very large amplitudes as rotors transverse their critical speeds, great sensitivity to unbalances conditions and poor resistance to instability. There are some methods [34]-[40] for introducing damping into passive magnetic bearing systems by using a resilient material. In general, these configurations rely on constructing an intermediate housing that is supported by a ball between the rotor and stator. The damping material is positioned between the housing and the stator. Due to the housing that is added to system complexity and it causes a reduction in the resonant frequency.

In addition, the stiffness and damping are coupled. In this study, an innovative damping induced by a magnetic force is investigated for the magnetic bearing motor systems.

3.2 Design and simulation

Fig. 3- 1 shows the configurations of the magnetic bearing motor. The ratio of slot number to pole number is 4: 4. The radial air gap between the stator and the rotor was fixed to 7×10^{-4} m. A Ba-ferrite ring with inner diameter of 3.14×10^{-2} m, axial length of 1.34×10^{-2} m, and outer diameter of 3.94×10^{-2} m were used for the magnetic rotor. Outside of the Ba-ferrite ring, an iron yoke with outer diameter of 4.1×10^{-2} m was attached. The magnetic bearing spindle motor was designed under the conditions of the rated speed is 3840 rpm. Two permanent magnetic annular magnetic rings were mounted on a shaft and two annular magnetic rings were mounted on a stator. The shaft bottom contacted the thrust plate. The magnet geometry has been optimized in order to increase the restoring force in radial direction. NdFeB magnets with $(BH)_{\max}$ of 45 MGOe were used. The dimensions of the rotating and stationary magnets are as follows. The OD of the rotating magnet is 6×10^{-3} m and the ID is 3×10^{-3} m. The stationary magnet OD is 1×10^{-2} m and ID is 7×10^{-3} m. The thickness of magnet used in both rotor and stator is 4×10^{-3} m. The rotating and stationary magnets had a slight 5×10^{-4} m radial air gap. Both rotating and stationary magnets had the same magnetization

direction along axial axis. The axial distance between upper magnetic bearing and lower one is 7.5×10^{-3} m.

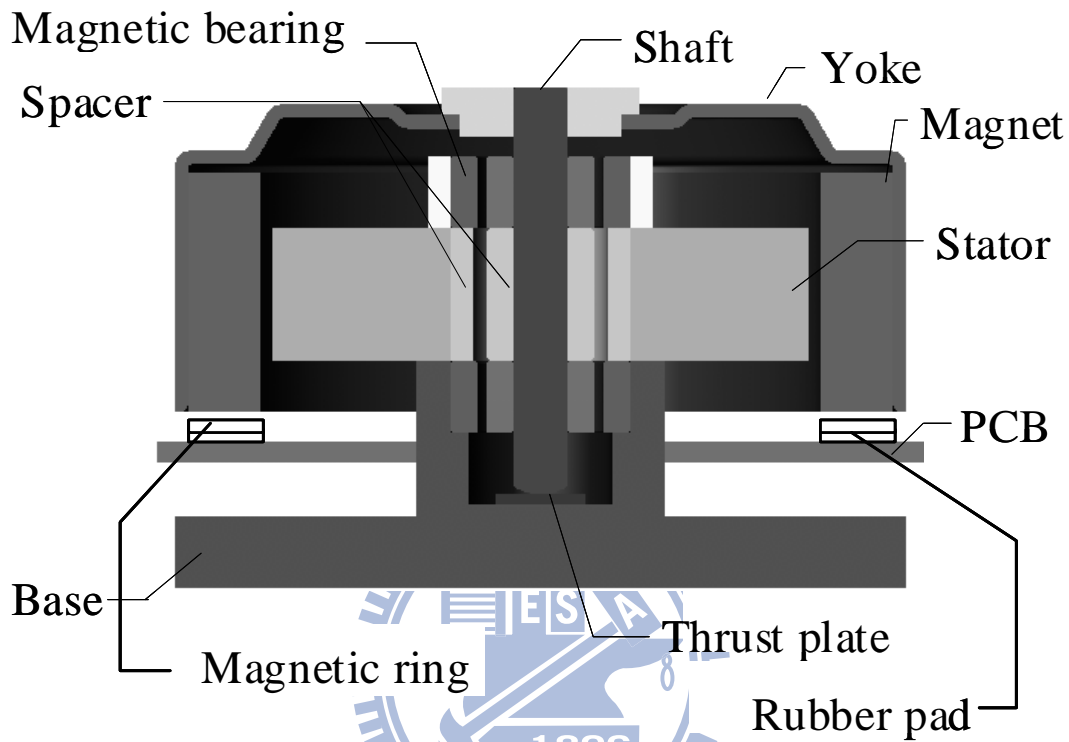


Fig. 3- 1. Magnetic bearing motor.

In order to improve the damping of the magnetic bearing motors, a novel configuration has been designed. The damping device is comprised of a magnetic ring with high permeability and an annular rubber pad (the damping is $0.2 \text{ N} \cdot \text{s/m}$), which is attached to the stator. It has the same outer and inner diameters with the permanent magnet of the motor and is 0.55 mm below it. The undesired rotor vibration forces are transmitted from the rotor permanent magnet through the magnetic field. The resistance of the rubber pad to the vibrations results in frictional forces, thus dissipating the vibration energy.

The damping ratio ξ is chosen as an index to evaluate the improvement of the damping. The static state of the rotor is considered. To carry out the analytic analysis easily, the simplified model is assumed as shown in Fig. 3- 2. It shows the rotor supported by two magnetic bearings. Suppose that the rotor can do the translation and rotation motions in only one degree of freedom. The damping can be adjusted by varying the material of the rubber pad. And the thrust plate is frictionless. Refer to the Newton's second law, a mass distribution m in the equation of motion is as following.

$$m\ddot{x} + (k_1 + k_2)x + (k_2l_2 - k_1l_1)\theta + (c_1 + c_2)\dot{x} + (c_2l_2 - c_1l_1)\dot{\theta} = 0 \quad (44)$$

$$J\ddot{\theta} + (k_2l_2 - k_1l_1)x + (k_2l_2^2 + k_1l_1^2)\theta + (c_2l_2 - c_1l_1)\dot{x} + (c_1l_1^2 + c_2l_2^2)\dot{\theta} = 0 \quad (45)$$

Each of the two magnetic bearings is linked to an elasticity and damping parameter k and c , respectively with the index 1 and 2. The l_1 and l_2 represent the length from the position of the center of mass to the lower and upper magnetic bearing. The x denotes the displacement for the simplified case of translation displacement along the x -axis. θ is the angle of the rotor rotated about the center of mass position relative to the y -axis.

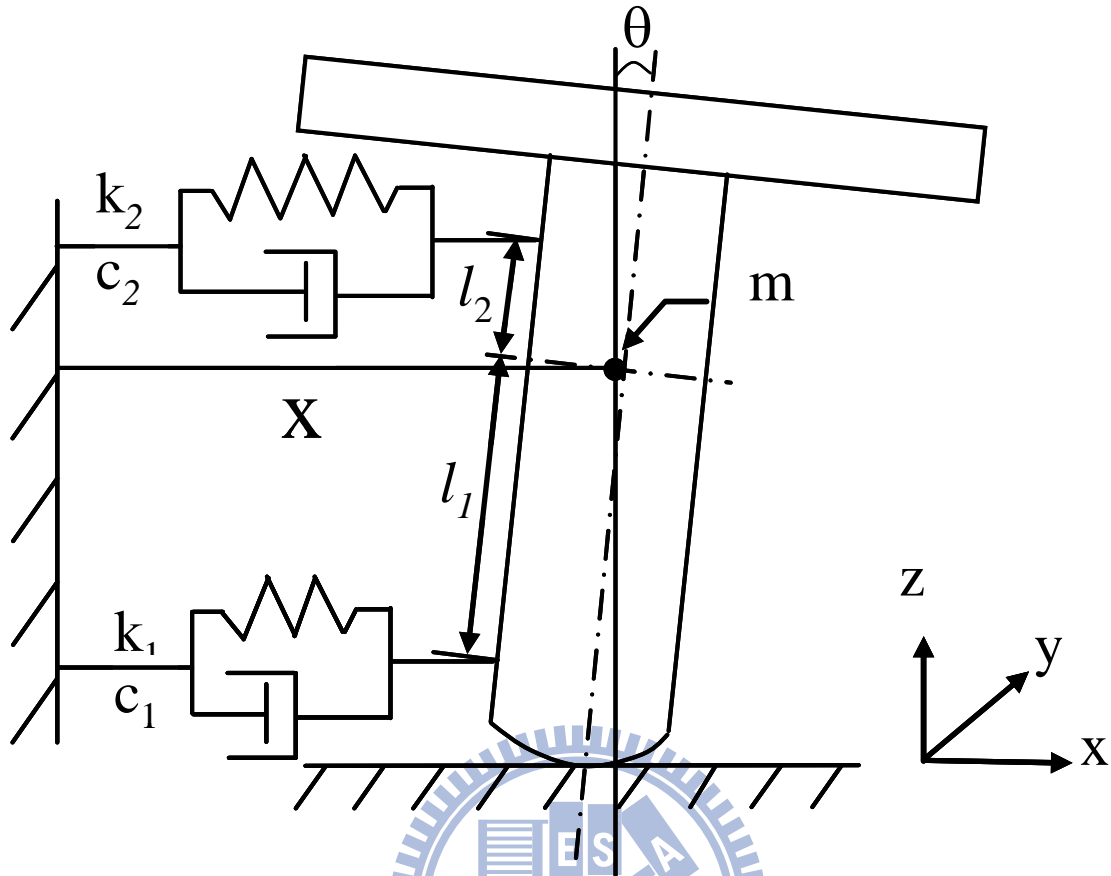


Fig. 3- 2. The simplified physical model of the magnetic bearing motor system.

Finite element analysis (FEA) was used to analyze the magnetic force of the magnetic bearing motor. Approach to this computation of radial force of the development system, the stator was fixed and the rotor was shifted along the positive x -axis as the following five different positions, 0 , 1×10^{-4} m, 2×10^{-4} m, 3×10^{-4} m, 4×10^{-4} m and 4.9×10^{-4} m. Three relative positions of magnetic inner and outer ring were shown in Fig. 2- 6. Since radial force was known and then the radial stiffness 1288 N/m of the magnetic bearing is perfectly determined. The B-H curves, namely 35AH440, spcc, ferrite, and N45, for the elements used in the system, i.e., stator, yoke, magnet, and MB, are shown as Fig. 3- 3 – Fig. 3- 6.

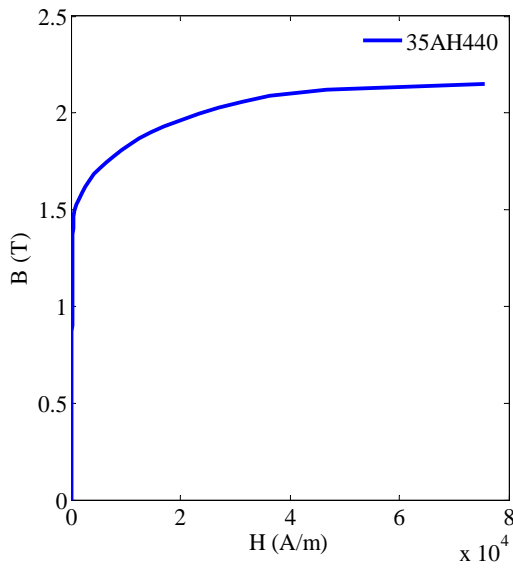


Fig. 3- 3. B-H curve of stator.

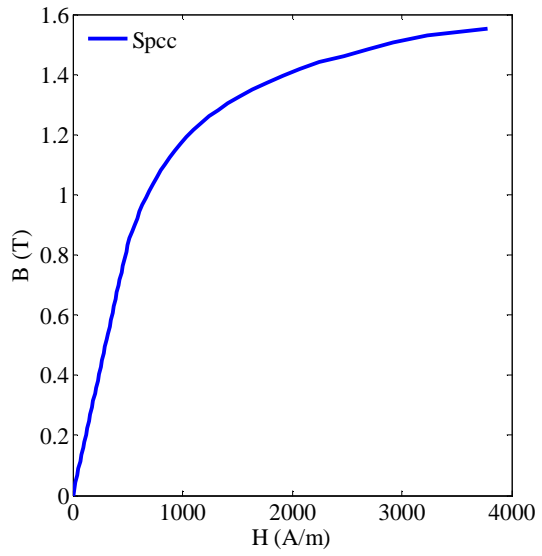


Fig. 3- 4. B-H curve of yoke.

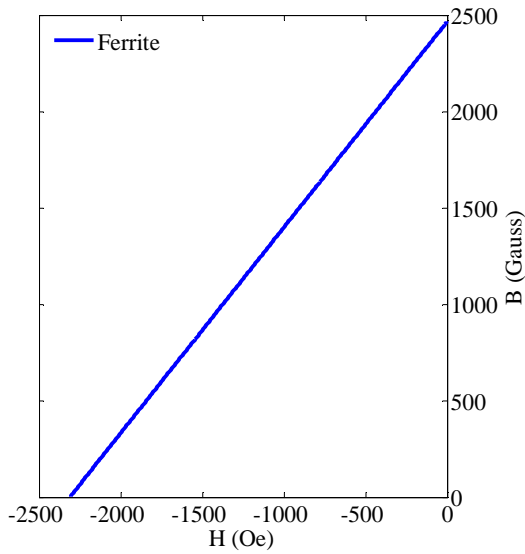


Fig. 3- 5 B-H curve of magnet.

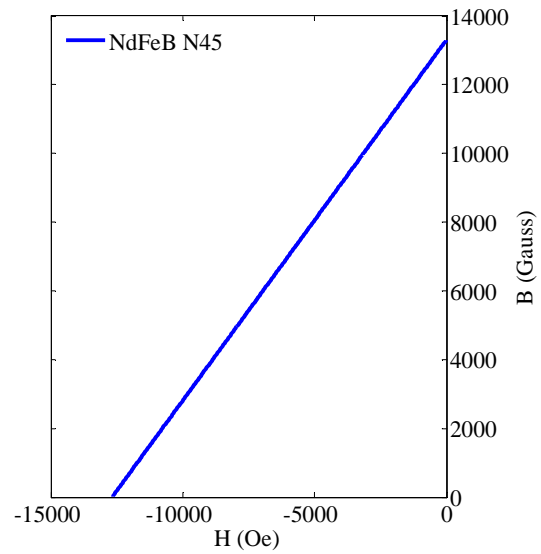


Fig. 3- 6 B-H curve of MB

3.3 Experimental testing

For measuring the damping ratio, a miniature hammer is included in this testing system. When magnetic motor was in its static state, an accelerometer was attached to the rotor in the radial direction. The hammer gave an impact shock in radial direction of

the rotor as the input driving force and the rotor of the magnetic bearing motor was excited and vibrated. The radial acceleration of the rotor was measured by using the accelerometer and the time response of the rotor was recorded. By using the FFT (Fast Fourier Transform), the frequency domain of the radial run-out could be obtained. From the frequency impulse method the damping ratio ξ was calculated by the general equation, $\xi = \delta / \omega_n \tau_d$. The δ was equal to $\ln(x_1/x_2)$, where the x_1 and x_2 were the peaks amplitudes chosen from the time response profile.

3.4 Results and discussion

Fig. 3- 7 shows the time response and frequency spectrum without the damping device from the experiment. Without the damping device, the damping ratio measured is 0.0655. From the experiment data it indicates that the natural frequency of original magnetic bearing motor is 23.5 Hz. To perform the calculating of the damping ratio with the damping device, the values of parameters as following are considered. Damping $c = 0.2 \text{ N} \cdot \text{s/m}$ was chosen, $l_1 = 7.85 \times 10^{-3} \text{ m}$, $l_2 = 3.65 \times 10^{-3} \text{ m}$, $c_1 = c_2 = 0.2 \text{ N} \cdot \text{s/m}$, $k_1 = k_2 = 1288 \text{ N/m}$, $m = 7.1 \times 10^{-2} \text{ kg}$. Then the differential equation (1) and (2) was solved. According to the same parameters that are used in the analytical analysis, the experiment was performed. The damping ratio of the experimental and analytical model is 0.1401 and 0.1170 respectively. It has the same significant levels of passive radial damping.

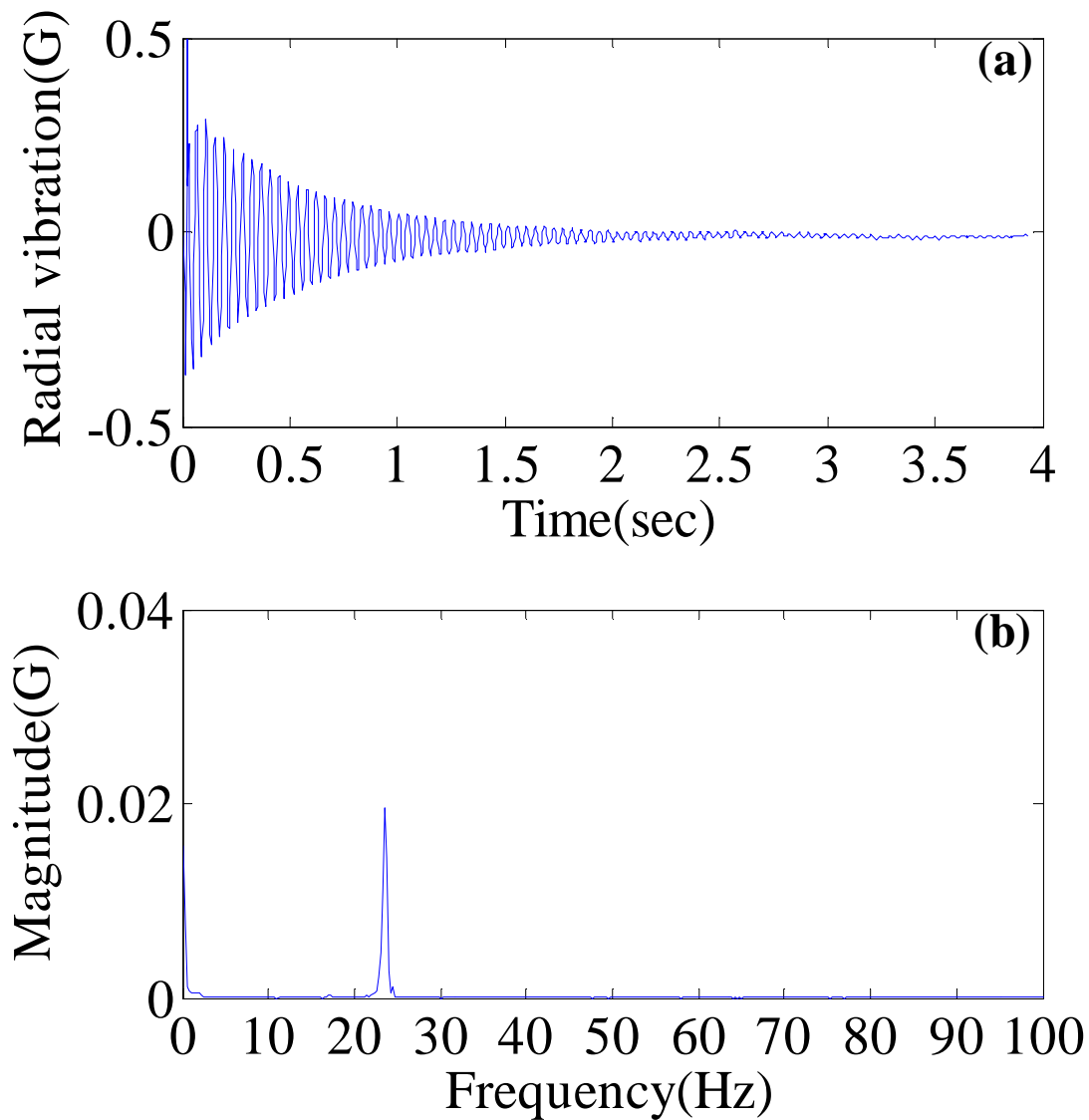


Fig. 3- 7. (a) Time response and (b) Frequency spectrum without damping device.

Both the results obtained from the two methods in damping ratio are greater than 0.1. The corresponding natural frequencies are 21.75 Hz and 19 Hz respectively. It has the same agreement in damping ratio and the natural frequency. The system resonance is avoided. Because of the rated speed is around 64 Hz, and the experimental and analytical model data in natural frequency is 42.25 Hz and 45 Hz below 64 Hz respectively. Fig. 3- 8 shows the time response and frequency spectrum with the

damping device from the experiment. The damping device applied in the developed magnetic bearing system, the ratio in damping ratio of our device to original device is

214 %.

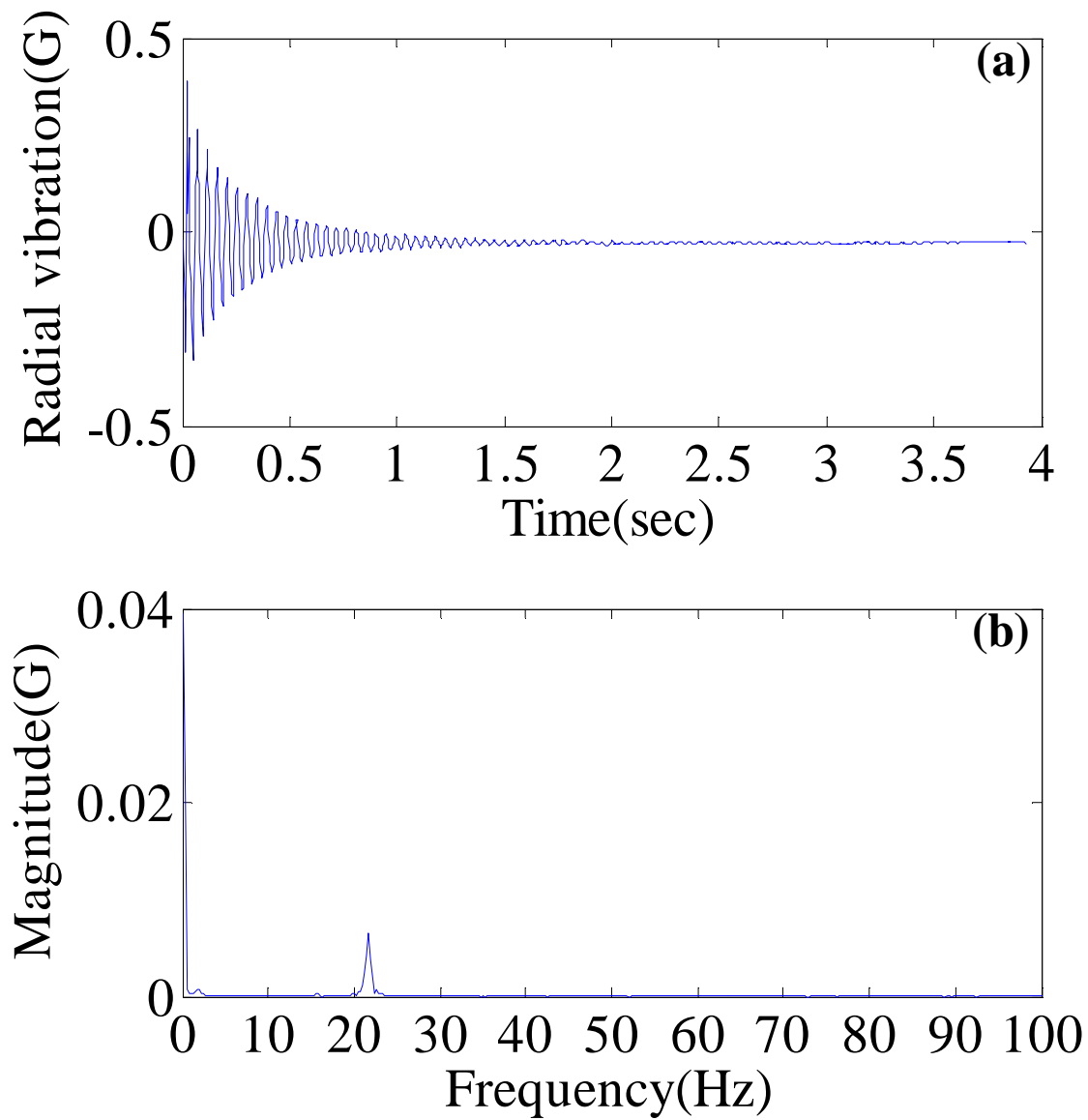


Fig. 3- 8. (a) Time response and (b) Frequency spectrum with damping device.

Chapter 4

Effect of bias-magnetic force

4.1 Preview

Passive MB motors present good potential for using in high efficiency, low power consumption, and extremely high speed devices such as hard disk drive spindle motors [41], polygon motors [42]-[43], optical disc drives, and fan motors [44]-[45] etc. In the design of the MB motor, it is crucial to design adequate axial stiffness of the MB for maintaining the minimum mechanical friction loss below a specified level and for minimizing the radial vibration due to the dynamic rotor system. However, many studies [46]-[47] have been focused on the MB motor design, but little research [48] has been done on the reduction of the radial vibration by considering the control of the axial force.

In this paper the axial forces composed of the preload, wind force, and bias-magnetic force are reported by both finite element analysis (FEA) and experimental measurement. The variation of radial vibration of the developed spindle motor is determined as a function of the effectiveness of axial force.

4.2 Design and force calculation

Fig. 4- 1 shows the MB motor with a bias magnet. The motor consists of a spindle

motor, a MB system, a PCB, and a Base. The motor has 4 slots and 4 poles. The radial air gap between the stator and magnet made of Ba-ferrite with an inner radius of 1.57×10^{-2} m, axial length of 1.34×10^{-2} m, and a radial thickness of 2×10^{-3} m is designed to be 7×10^{-4} m. Outside the ferrite ring an iron yoke with a radial thickness of 8×10^{-4} m is mounted. The principle electrical parameters for the MB motor are 3720 rpm under a current of 0.27 A. The MB system consists of two MB units assembled in lower and upper end of the shaft, and separated by an axial length of 7.5×10^{-3} m. Each unit designed with a radial air gap of 5×10^{-4} m and bearing length of 4×10^{-3} m consists of one inner and outer ring magnet made of Nd-Fe-B with $(BH)_{\max}$ of 45 MGOes, and magnetized in the same axial direction along the shaft. The inner ring with an inner diameter of 3×10^{-3} m is rotated with the shaft, and the outer one is fixed on the stator. Both of these two rings are designed with the identical radial thickness of 1.5×10^{-3} m. In order to generate the adequate radial restoring force to support the radial load, the geometry of the MB system has been optimal designed. Therefore, the MB can stably maintain the slight radial air gap between the rotating and stationary parts of the motor. However, to avoid the inherent stability problem [49], a single conjunctive pivot point is employed between the shaft and the thrust plate.

The novel bias-magnet made of $(BH)_{\max}$ of 33 MGOes with an outer diameter of 3.09×10^{-4} m, inner diameter of 6×10^{-3} m, and axial length of 7×10^{-3} m is employed above

the motor as a dynamic vibration absorber [50]. The B-H curve of the bias-magnet is shown as Fig. 4- 2.

To calculate these axial forces, FEA software of MAGNET 6.18 is applied. First, the estimation of downward force. This force, called preload, is the axial force generated due to the offset axis displacement between the stator and magnet. Also, the offset axis displacement between the inner and outer ring of the MB unit contributes to it (see Fig. 4- 1). To compute the force, the rotor is shifted along the negative z axis with a displacement interval of 5×10^{-5} m when the D_z ranges from zero (the balanced position) to 4×10^{-4} m. The D_z is the axial gap between the lateral axis of the inner and outer ring magnet of the MB unit (see enlargement top left in Fig. 4- 1). After performing the FEA calculation, the preload as a function of the D_z can be gained. Second, the computation of upward force. This force consists of bias-magnetic force and wind force. For determining the bias-magnetic force, the bias magnet with the same axis of the shaft is arranged above the MB motor, and the axial distance from the top surface of the shaft to the bottom surface of the bias magnet corresponds to D_{bs} (see Fig. 4- 3). When the D_{bs} ranges from 1.77×10^{-2} to 5.27×10^{-2} m, the bias magnet is shifted along the positive Z axis with a displacement interval of 5×10^{-3} m, so the bias-magnetic force varies with the D_{bs} is successfully estimated subtracting the net axial force from preload. The wind force is determined by experimental approach, and supposed to be independent of the

D_z or D_{bs} . Since the downward and upward forces are estimated, the calculation of the net axial force of the proposed system in dynamic state can be completely performed.

4.3 Experiment and results

Fig. 4- 3 shows the configuration of the test set-up for the axial force measurement. The MB motor supported by a load shaft with a single conjunction point is fixed on a base B that is tightly fixed to a base A. The load shaft is locked to a load cell used to measure the axial force, and fixed to a z stage. For applying a bias-magnetic force to the motor, the bias magnet is fixed to a micrometer locked to a xy table. Then the table is assembled to a base B. The running speed and current of the motor are collected from power supply and RPM meter, respectively. After the desired forces are completely measured, the MB motor is re-assembled with a base, and an accelerometer is attached to the base of the motor in the radial direction to record the radial vibration.

The mean value of measured wind force of the motor is around 0.596 N upward. The predicted preload of the motor is compared with experimental preload, as shown in Fig. 4- 4(a). Fig. 4- 4(b) displays the comparison of predicted net axial force of the motor in dynamic state with experimental net axial force. Since these three axial forces discussed above are determined, the bias-magnetic force of the motor can be successfully calculated deducting the wind force and preload from the net axial force, as shown in Fig. 4- 4(c). For effectively achieving the radial vibration reduction of the

motor, the distribution of the bias-magnetic force as a function of the D_{bs} is specially designed, so the frequency of the bias magnet can be exactly tuned to the same frequency as the rated speed of the MB motor. To get the profiles, Fig. 4-4(b) and Fig. 4-4(c), the D_z of the motor is set at 3×10^{-4} m. The above results reveal that predicted axial forces, the net axial and bias-magnetic forces, have the good agreement with the experimental data. This suggests that the FEA could be considered utilizing in the prediction of the key axial forces, essentially affecting the radial vibration of the developed MB motor. For evaluating the bias-magnetic force effect under the case of the varied preload of the MB motor, the net axial force of the motor in rotating state is measured corresponding to different positions of D_z , the initial and end positions are 1.5×10^{-4} , and 4×10^{-4} m, respectively, and the sampling interval between the two positions is 5×10^{-5} m, as shown in Fig. 4-4(d).

Without the bias-magnetic force, the radial vibration of the motor is probed as D_z is in three different positions, 2×10^{-4} , 3×10^{-4} , and 4×10^{-4} m, as shown in Fig. 4-5. The related net axial forces of these three concerned positions are -2.981, -4.804, and -6.803 N, respectively. The distribution of the radial vibration as a function of the net axial force indicates that the radial vibration is decreased when the net axial force is increased.

However, when the bias-magnetic force is applied to the MB motor, the radial

vibration of the motor can be sharply diminished, as shown in Fig. 4- 6. To investigate the behavior of bias-magnetic force in reducing the radial vibration of the MB motor, the D_z is fixed at three selected positions, 2×10^{-4} , 3×10^{-4} , and 4×10^{-4} m, then the bias-magnetic force is applied to each condition; however, the point with the maximum net axial force of each individual curve is in the case of the proposed motor without the bias-magnetic force. According to the discussion of the Fig. 4- 5, normally, the decrease of the net axial force of the MB motor will result in increasing the radial vibration of the motor; however, there exists three local minimum radial vibrations of the MB motor as the net axial force is gradually decreased in each curve (see Fig. 4- 6). This demonstrates that the proper bias-magnetic force distributions generating the exact axial stiffness to make the natural frequency of the bias magnet equivalent to the rotating speed of the MB motor are significantly useful for reducing the radial vibration of the motor. When the motor is operated, and generates these three minimum radial vibration waveforms, each of these dominant magnitudes in frequency domain corresponding to the waveforms shows the same frequency with the rated rotational speed, 62 Hz, as shown in Fig. 4- 7. Fig. 4- 8(b) shows that the time response of the local optimal radial vibration of the MB motor operated with the bias-magnetic force of 0.539 N and the net axial force of -6.735 N is around 0.197 g (peak-peak), and the ratio in the radial vibration of the MB motor under this condition to the one eliminating the bias force

shown in Fig. 4- 8(a) is around 89 percent, and it saves around 0.24 W of driving power.

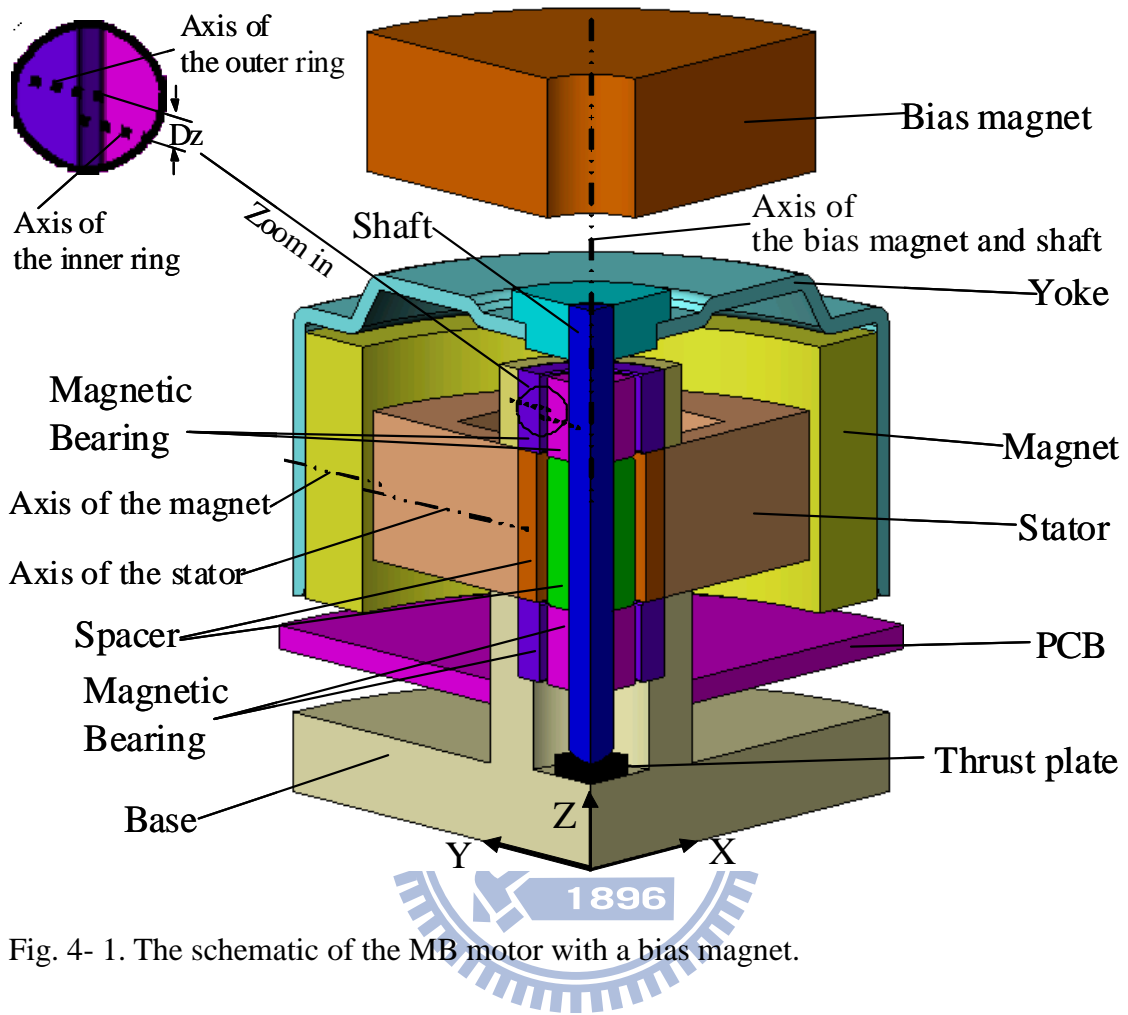


Fig. 4- 1. The schematic of the MB motor with a bias magnet.

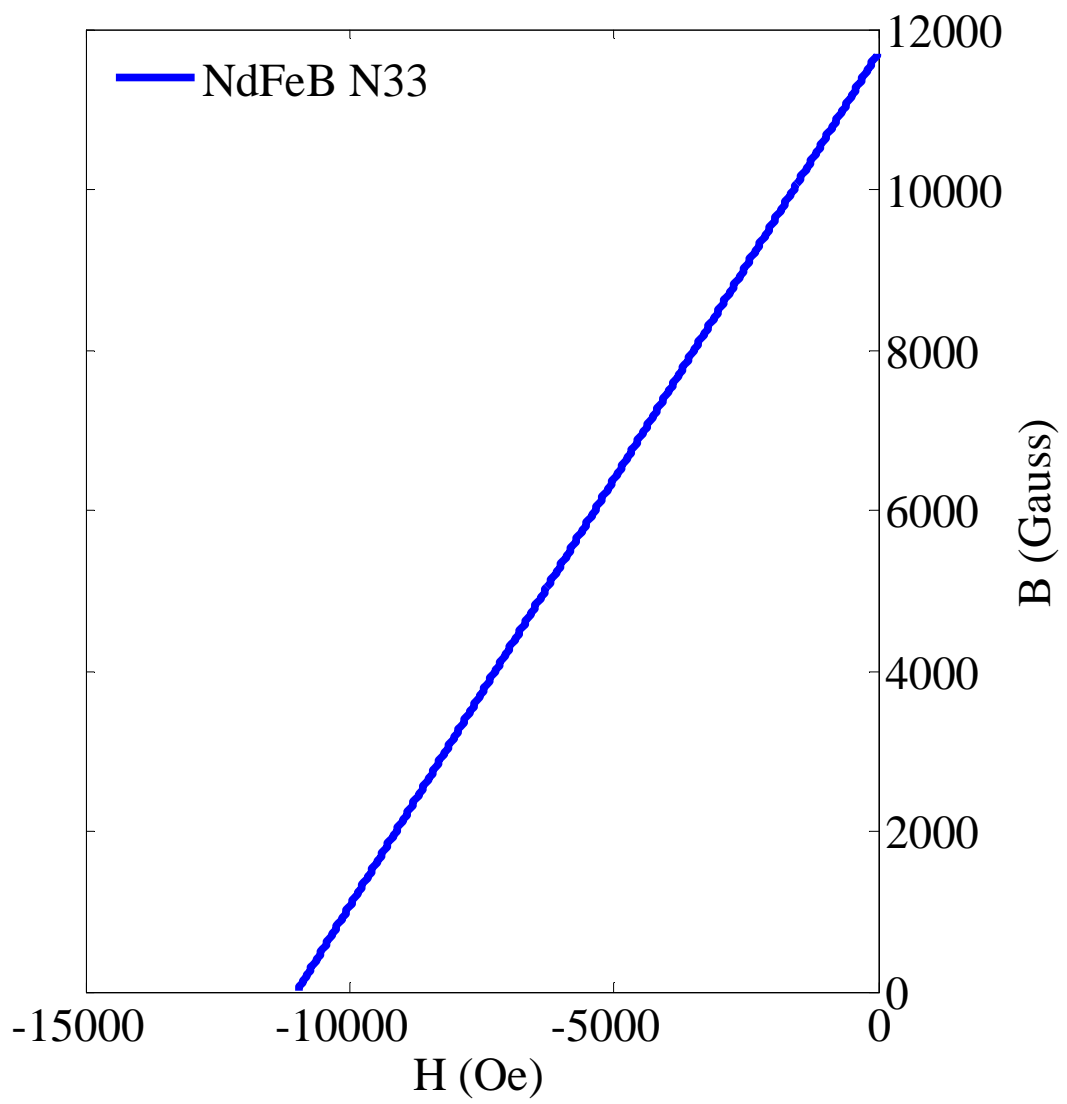


Fig. 4- 2. B-H curve of bias-magnet.

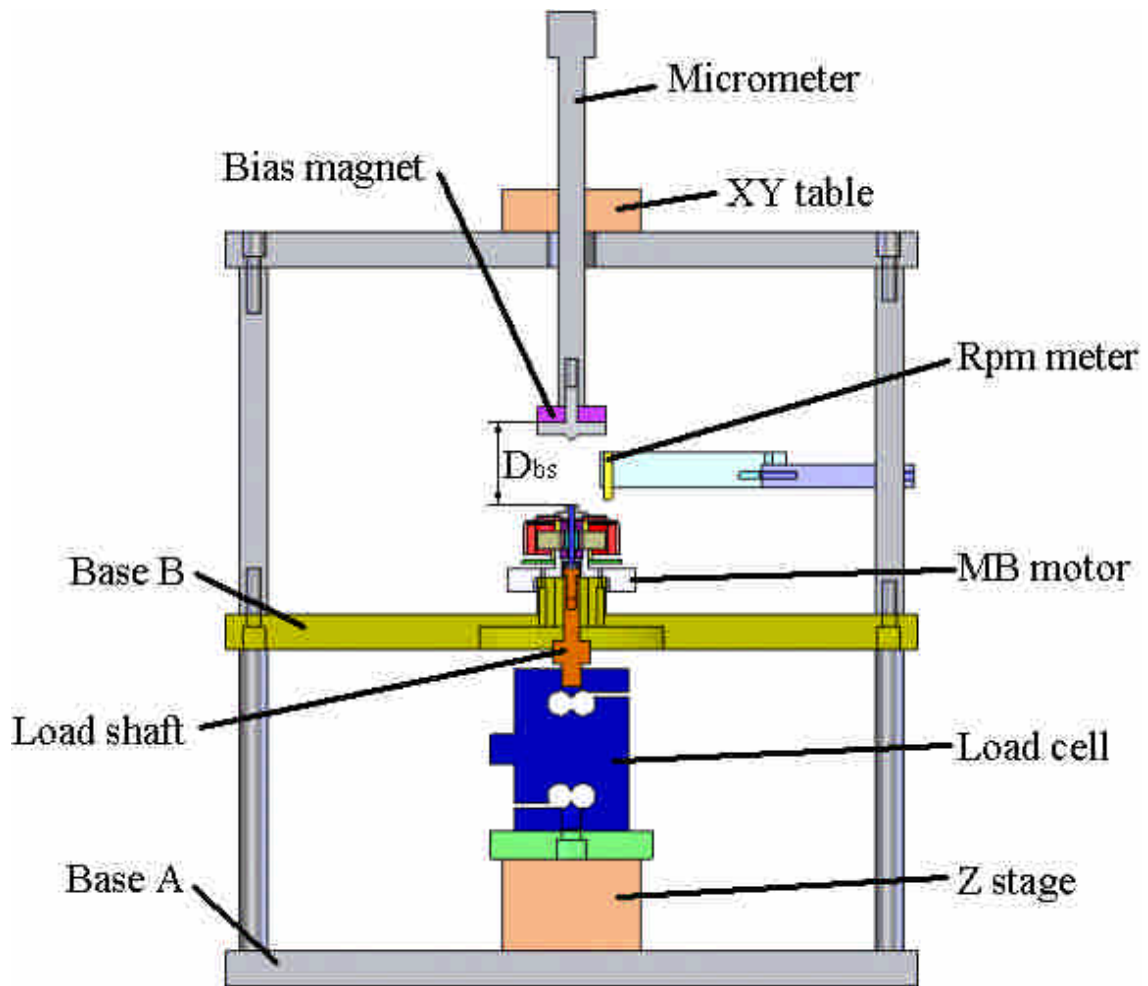


Fig. 4- 3. Configuration of the test set-up for axial force measurement.

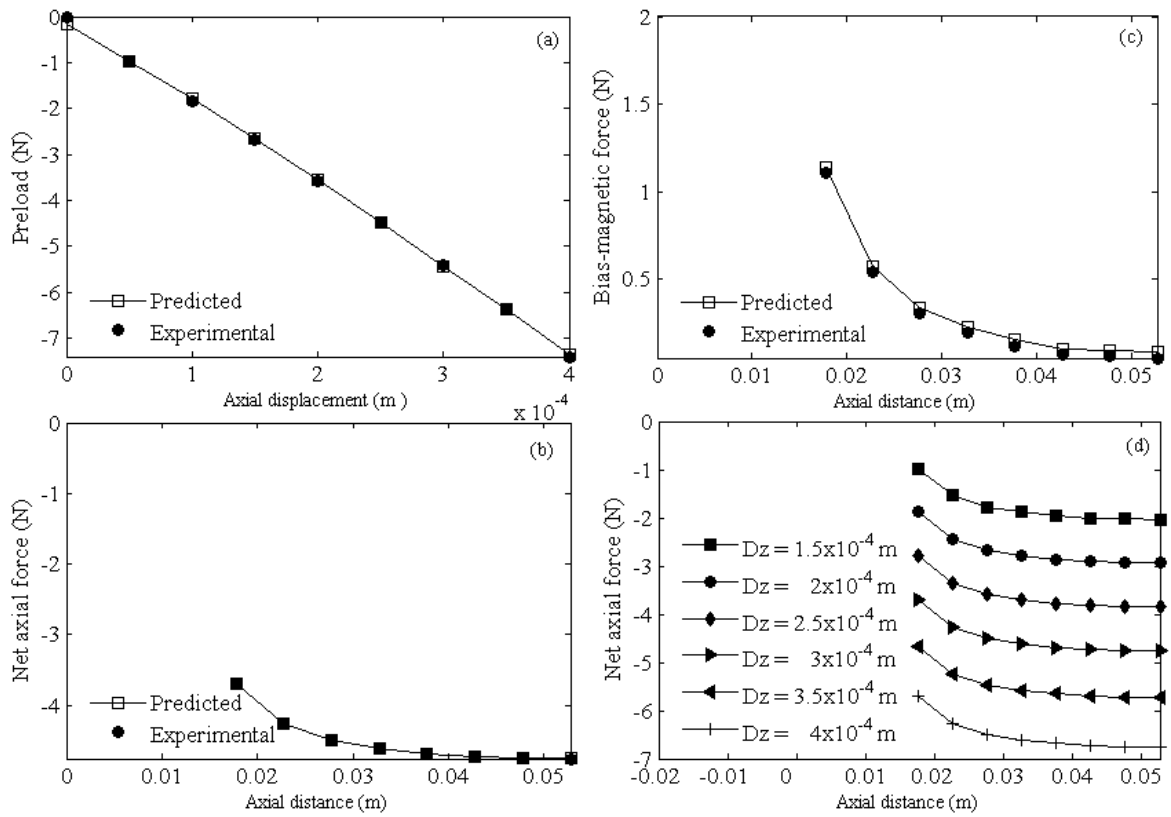


Fig. 4- 4. (a) The comparison of predicted preload of the MB motor with experimental preload. (b) The comparison of predicted net axial force of the MB motor with experimental net axial force. (c) The comparison of predicted bias-magnetic force of the MB motor and experimental bias-magnetic force. (d) Measured net axial force of the MB motor with bias magnetic force for Dz in different positions.

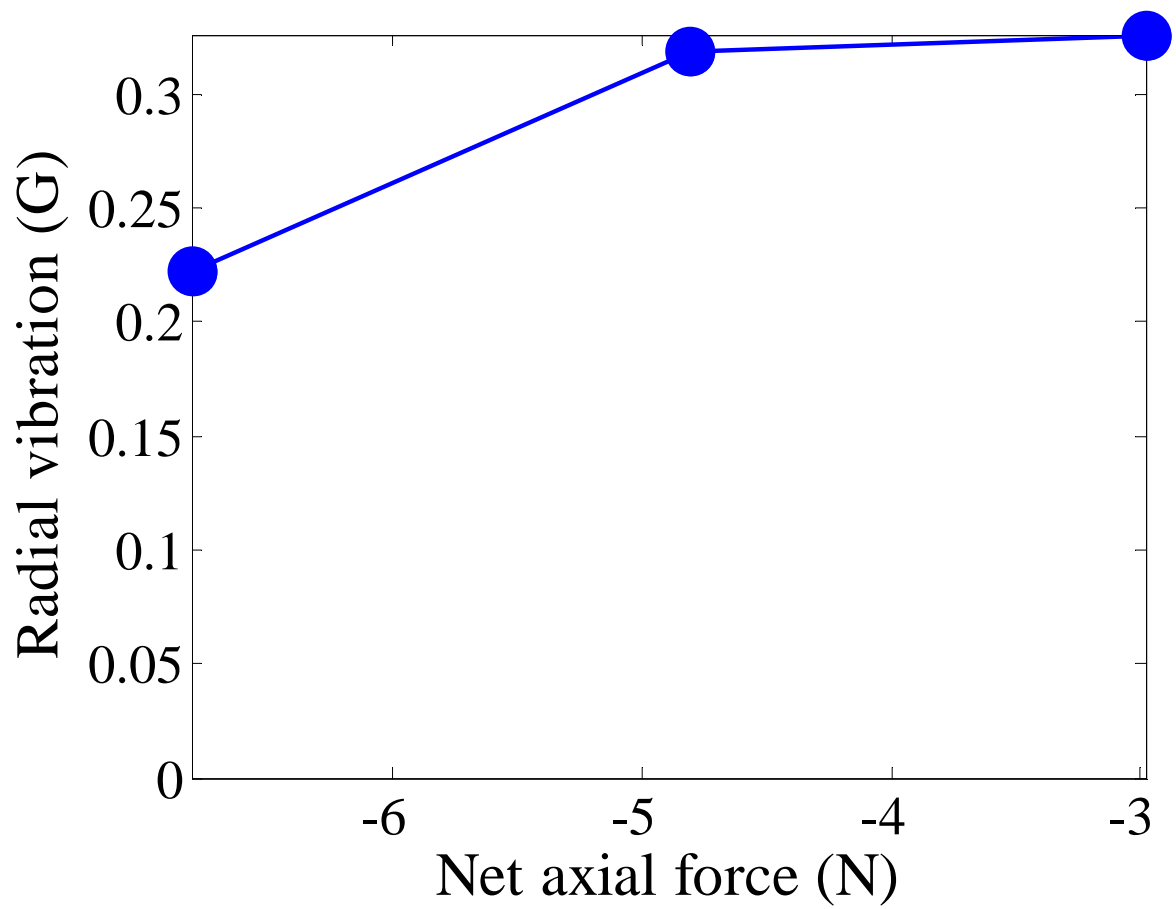


Fig. 4- 5. The radial vibration of the MB motor as a function of the net axial force.

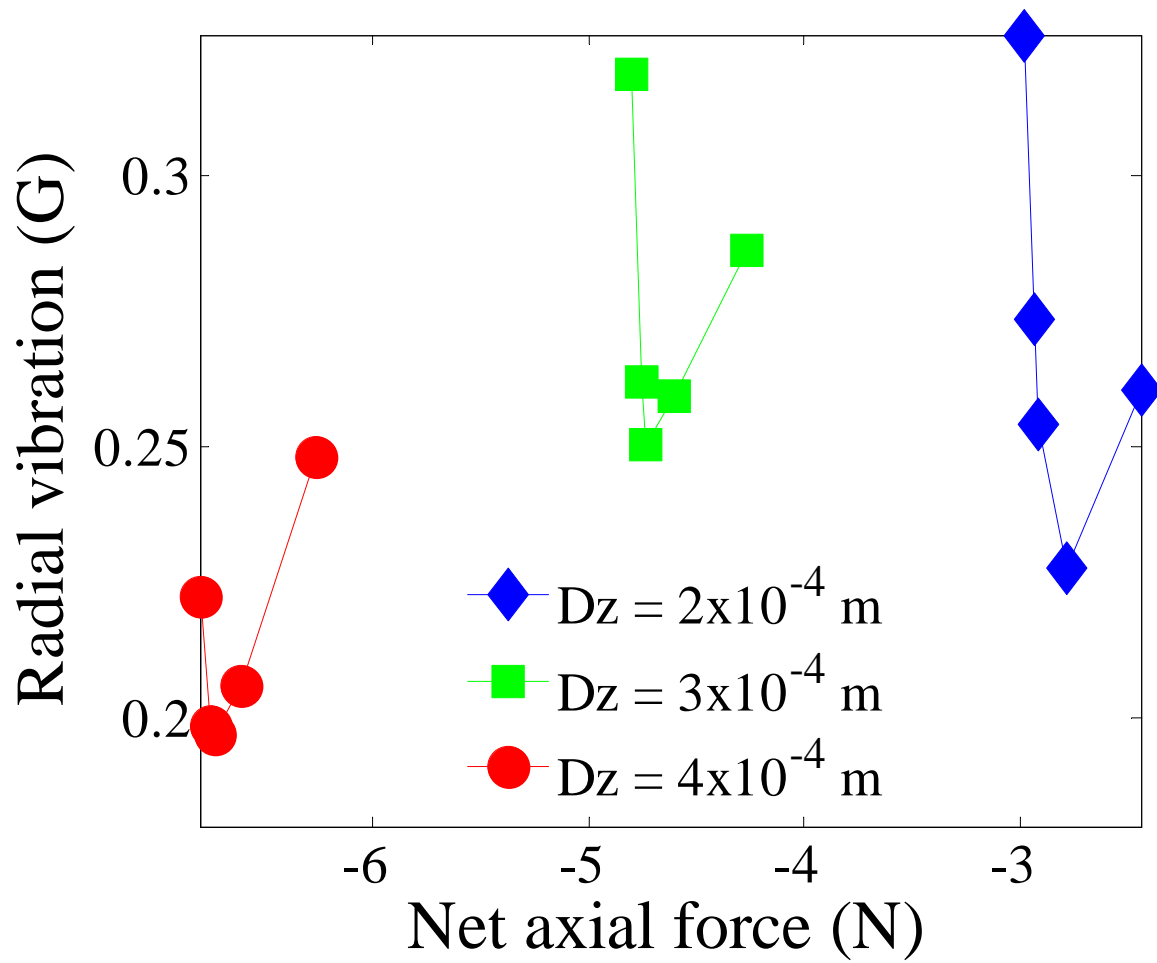


Fig. 4- 6. The Radial vibration of the MB motor as a function of the net axial force and Dz .

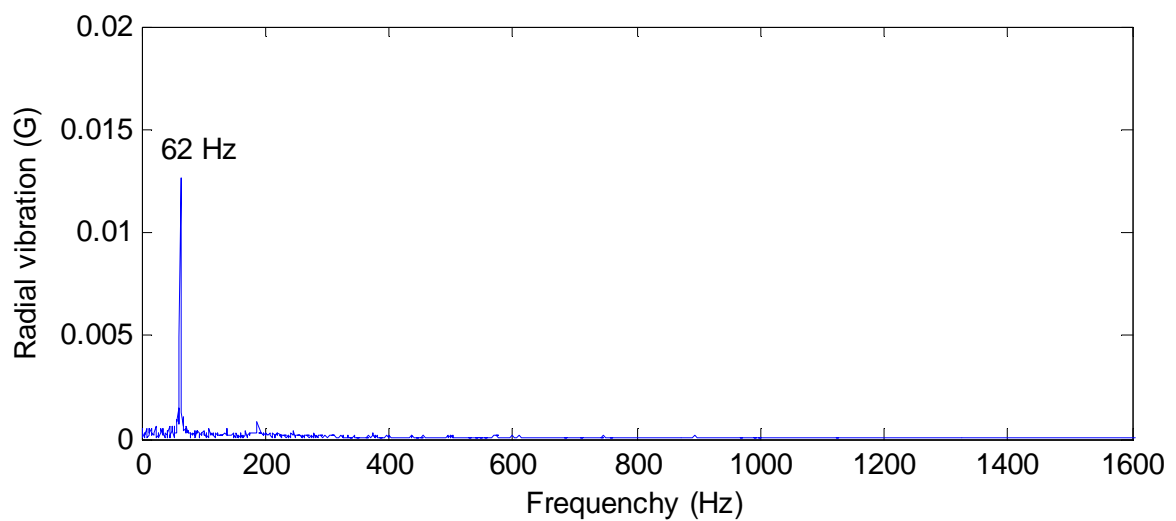


Fig. 4- 7. The dominant magnitude of the radial vibration in frequency domain measured on the bias magnet.

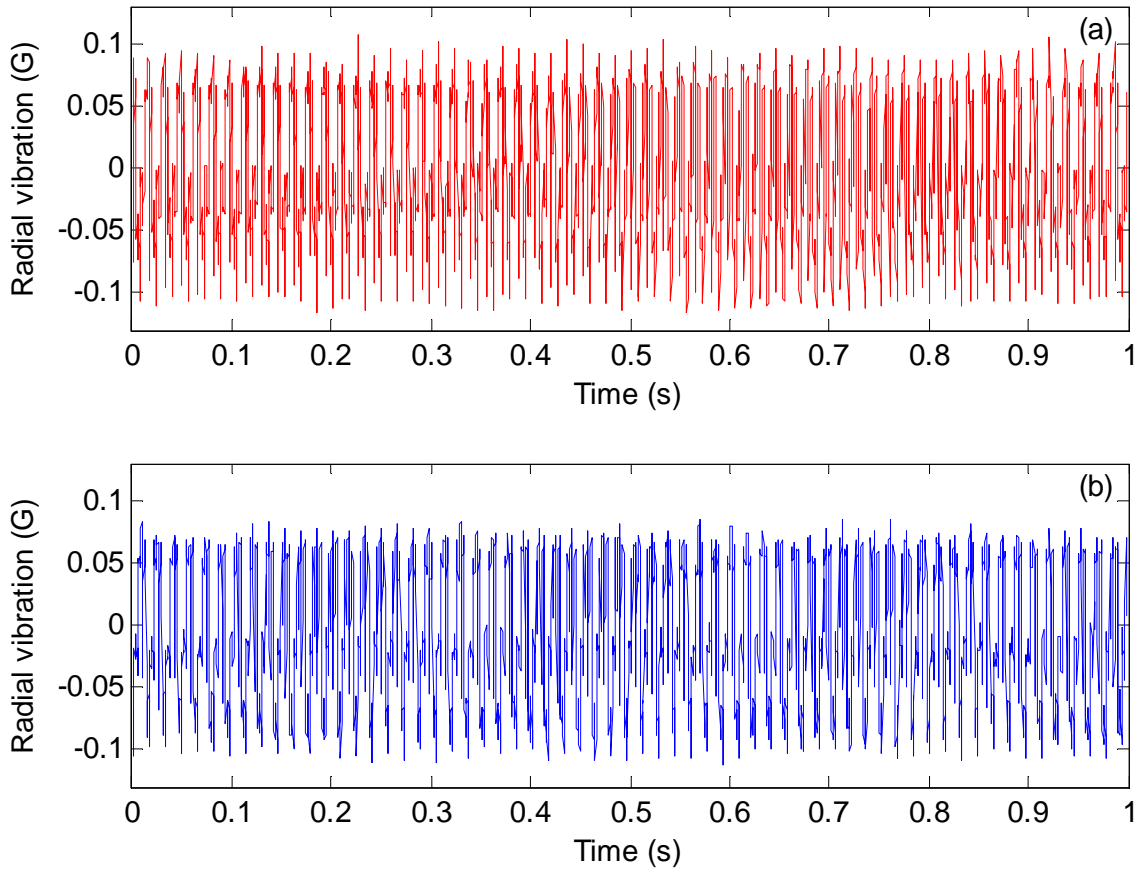


Fig. 4- 8. Time responses of radial vibration of the MB motor (a) without (b) with bias-magnetic force.

Chapter 5

Design of a scaled-down MB motor for portable disk drives

5.1 Preview

To achieve the low cost, simple, and high density in the trend of the optical data storage drives, the most important issue is to obtain the high performance key elements of the drives. To develop these new micro optical drives, recently, few papers have focused on the key components of SFFO drives [50]-[53], such as optical actuators, try to improve the performances of miniature optical devices by applying the novel magnetic circuit designs [54] due to the advantage of these designs that result in producing magnetic force without any contact between two objective components and this may lead to low friction loss, long life-span and high speed micro motors successfully.

Several researchers have been focused on the magnetic bearing design [55]-[56] to decrease the torque loss of a motor, but no work has been done on the miniature magnetic bearing development. The magnetic bearing may be a good approach of challenging the tribology, the elimination of the friction loss, which dominated the mechanical friction torque loss in the spindles. However, the additional magnetic bearing to be constructed in a micro motor will induce the magnetic coupling effect

between the stator and rotor that may increase the cogging torque [57]-[62] of the motor.

The main purpose of this paper is to design a simple and compact MMB motor with the well control dragging-torque that achieves the low friction loss for using in a miniature optical drive.

5.2 Configuration of the MMB system

The developed MMB motor was constructed by replacing the two micro ball bearings of a conventional BLDC 3 phase MBB motor with unbalance 0.002 g-cm. The original motor had the rated speed 1850 rpm and current 0.18 Amp. The slot number and pole number were 12 and 9 respectively. The configuration of the MMB is shown in Fig. 5- 1. The micro motor consisted of a rotor and stator. The shaft that had a pivot point contacted with the thrust plate was located in the center of the motor. The MQ ring was fixed at the lower end of the shaft and a radial air gap 0.2 mm was assigned between the stator and rotor. The B-H curve of the MQ is shown as Fig. 5- 2. The outer diameter, inner diameter and high of this ring were 9.4, 7 and 1.5 mm. The yoke with outer diameter 9.8 mm high and high 0.4 mm was attached below this ring. The proposed MMB system was composed of an inner and outer annular permanent magnetic ring that was made of NdFeB N45. The outer, inner diameter and height of the inner ring were 4, 1 and 3.6 mm; those for the outer ring were 8, 5 and 3.6 mm respectively. Each of these

two rings contained the two same sub magnetic rings that were provided with anti-parallel magnetization directions along the axial-axis.

5.3 Design and analysis

For identifying the proposed system, the magnetic forces were calculated by applying the Maxwell stress method, according to the govern equation of magnetic field that is Maxwell's equation. To perform these calculations, the FEA software Magnet 6.18 was used. The 3D half model of the design motor shown in Fig. 5- 3 was provided with the number of tetrahedral 252987.

To design a stable micro magnetic bearing system, there were three main subjects that must be considered. These subjects were as follows. (1) Static stable state. (2) Dynamic stable state. (3) Well-controlled axial force. First, to achieve the static stable state, the system must induce the enough restoring torque when it suffered an additional tilt torque. Suppose that the shaft was tilted at an angle θ , relative to the pivot point, in the clockwise direction along the positive y-axis refer to the coordinate system in Fig. 5- 3. Since it was a critical condition when the θ was 2 degree, the principle parameters that were sensitive to the stable state of the proposed system were estimated when the θ was chosen to this value. To analyze the distribution profile of the restoring torque T_y , the fluctuation of the T_y due to the axial gap Z_{gap} and the rotation angle was calculated as shown in Fig. 5- 4. The Z_{gap} was positive when outer one higher than inner

one magnetic ring of the MMB in positive axial direction. The initial rotation angle between the rotor and stator is shown in Fig. 5- 5. The Fig. 5- 4 revealed that the stable region of the micro magnetic bearing system appeared when the Z_{gap} ranged from 0.1 to 0.3 mm.

Second, to obtain the dynamic stable state, the develop bearing must generate the enough radial restoring force which was two times the radial loading at the rated speed and this was referred to our laboratory data base. For the radial run-out (RRO) of this prototype was assigned to $10\mu\text{m}$ (peak), the restoring force must greater than 7.506×10^{-4} N. This corresponding RRO-constrain the tilt angle was 0.0785 degree and the desired RRO could be maintained according to the FEA estimation of magnetic radial forces that were -0.02956 and -0.02215 N when the Z_{gap} were 0.1 and 0.3 mm respectively. To verify the dynamic stable state could be maintained under the magnetic coupling effect, the restoring radial force changed due to the rotation angle and Z_{gap} was calculated as shown in Fig. 5- 6. It is manifest that the restoring force is high enough to resist the radial loading force when the Z_{gap} are operated between 0.1 and 0.3 mm. This guarantees that the target RRO could be satisfied and the system could be stable in the dynamic state.

Third, for achieving the well-controlled axial force, four constrains should be specified as follows. $P < 10^6 \text{ kg/m}^2$, $V < 7 \text{ m/sec}$, $P \times V < 10^5 \text{ kg/(m} \cdot \text{sec)}$ and the target

friction loss $< 2.926 \times 10^{-4}$ Nm. The first three and the last items were constrained due to the specification of the thrust plate and the desired friction loss must be lower than the MBB type motor respectively. According to these considerations, the corresponding final axial force criterion that must be smaller than 5.081 N was decided. The calculation shows that the axial force varies with the rotation angle steadily for each chosen Z_{gap} (0.1, 0.2 and 0.3 mm) and each maximum value of these axial forces is smaller than 5.081 N when the Z_{gap} ranges from 0.1 to 0.3 mm and the maximum goes from 1.339 to 3.599 N.

Refer to earlier mention that it is manifest that the restoring torque and radial force are not highly related to the variation of the rotation angle, but the friction loss is. According to FEM estimation the friction loss due to the magnetic axial force is shown in the Fig. 5- 7. Fig. 5- 8 shows the original cogging torque represented by crosses, after the magnetic bearing system was assembled into the motor, the cogging torque was increased and deformed to the dragging-torque curves when $Z_{\text{gap}} = 0 \sim 0.3$ mm, i.e., the dragging-torque is equivalent to the friction loss plus the cogging torque. However, the absolute peak values of these profiles were well controlled smaller than 1.93×10^{-4} Nm.

It was assumed that the thrust plate contacted with the shaft in 1/4 times the shaft diameter. The kinetic friction coefficient of the thrust plate was 0.06. The total friction loss caused by the MMB was equivalent to the friction loss contributed by the magnetic

axial force added by the dragging torque, then the total friction torque loss (peak) generated by the MMB were -1.16×10^{-4} , -1.49×10^{-4} , -1.73×10^{-4} and -1.93×10^{-4} Nm when the Z_{gap} were 0, 0.1, 0.2, and 0.3 mm respectively. This leads to that design motor has the lower friction loss than the MBB type perfectly.

5.4 Experiment

Based on the analytical simulation that the stable state of the MMB motor appears when the $Z_{\text{gap}} = 0.1, 0.2$ and 0.3 mm. During this region, the experimental data of the MMB motor shows that motor speed ≥ 1850 rpm and the running current ≤ 0.18 A and this is consisted with the prediction. As the $Z_{\text{gap}} = 0.2$ mm, the total friction loss and radial vibration of the MMB motor were measured and represented in the following.

To measure the friction loss of a micro motor, the motor was operated at various constant speeds, then the friction loss was equivalent to the running current times the torque constant of the motor. The torque loss varies with the speed are shown in [Fig. 5-](#)

9. It is apparently that the MMB motor had a lower friction loss than ball bearing type.

For observing the radial vibration of the micro motor, the motor was fixed to a free table, an accelerometer was attached to the motor in the radial direction and a spectrum analyzer was employed to detect the output signal of the accelerometer. The time response signals were probed as shown in [Fig. 5- 10](#), when the rotor was rotated at the speed around 1850 rpm and running current around 0.18 Amp. The radial vibration

(peak-peak) of MBB and MMB motor were 5.954 mG and 4.668 mG, respectively.

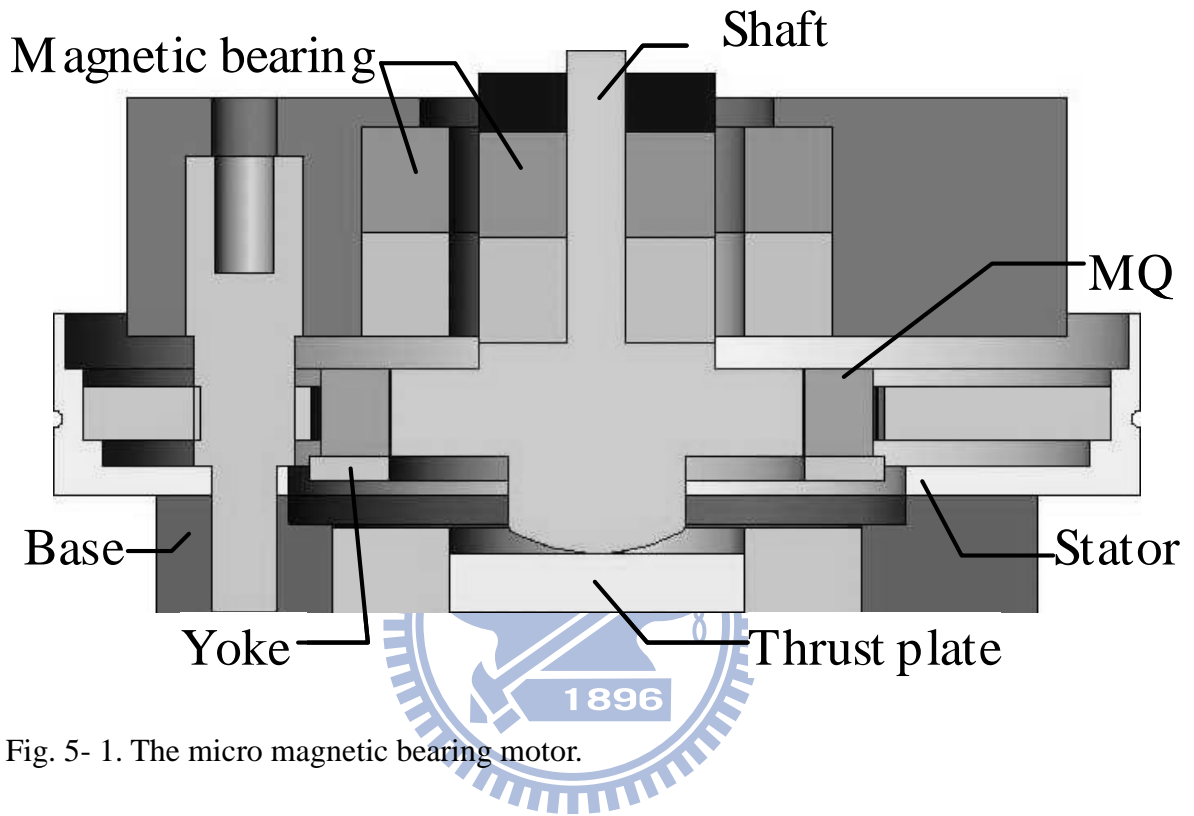


Fig. 5- 1. The micro magnetic bearing motor.

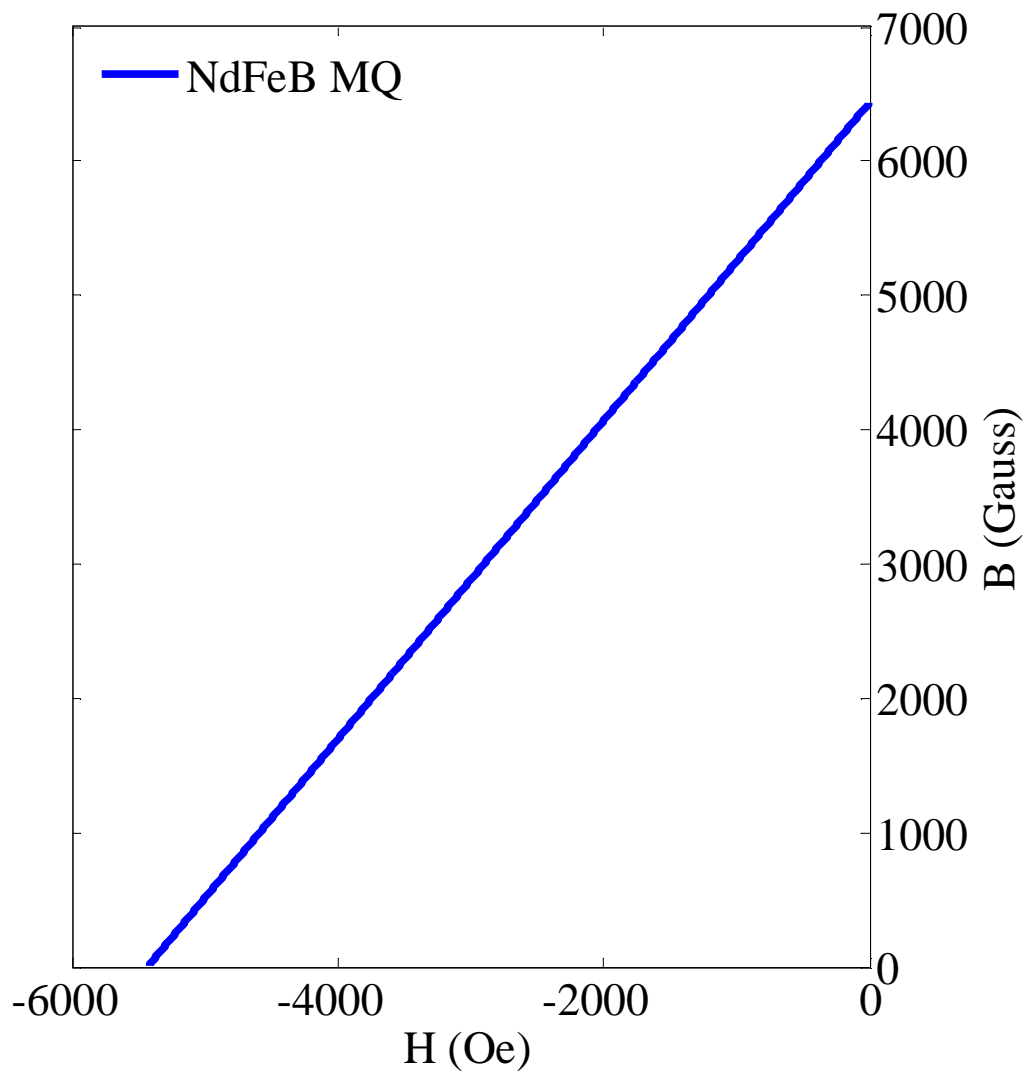


Fig. 5- 2. B-H curve of MQ.

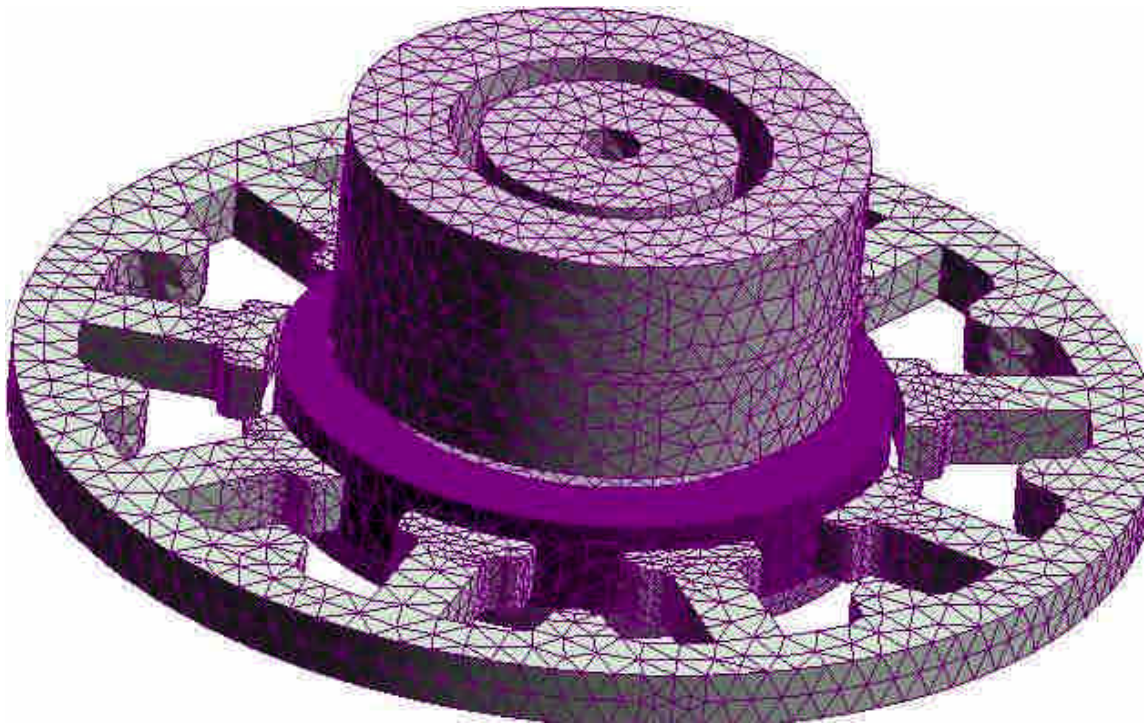


Fig. 5- 3. The 3D mesh model of the MMB motor.

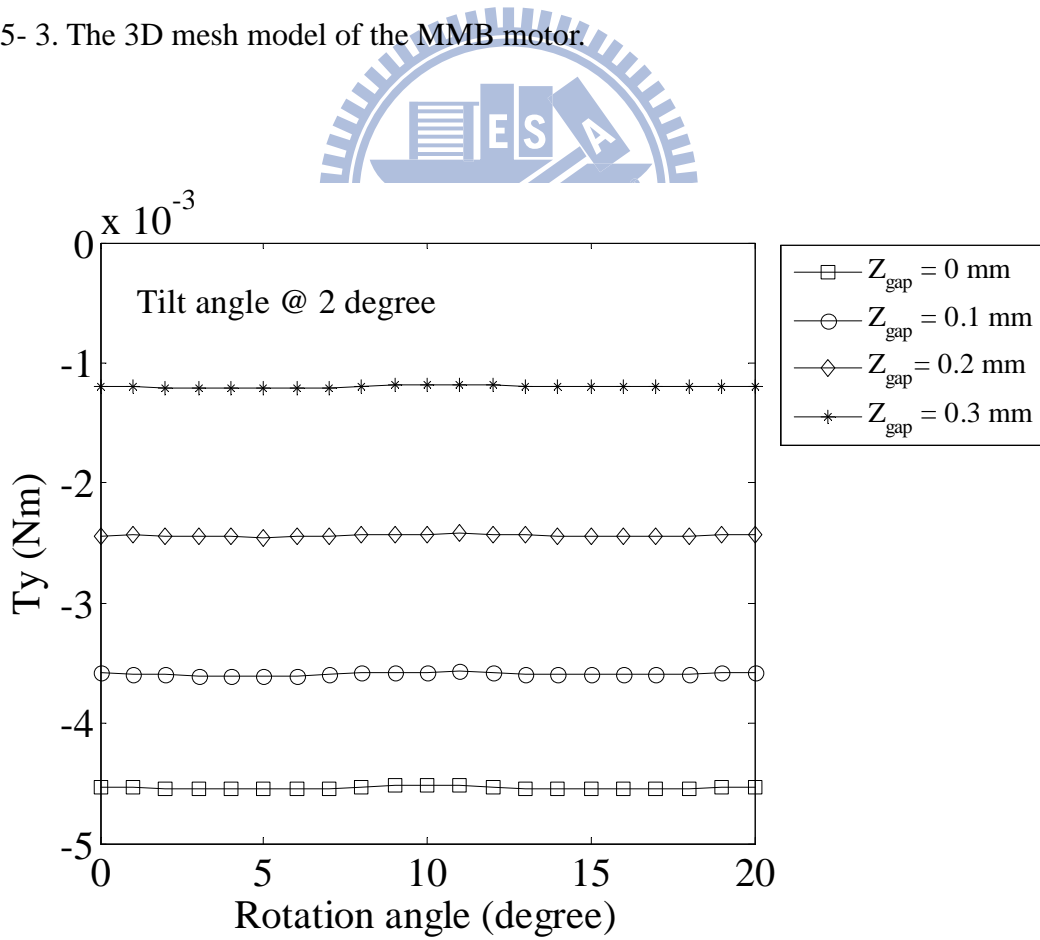


Fig. 5- 4. Restoring torque varies with the rotation angle and Z_{gap} .

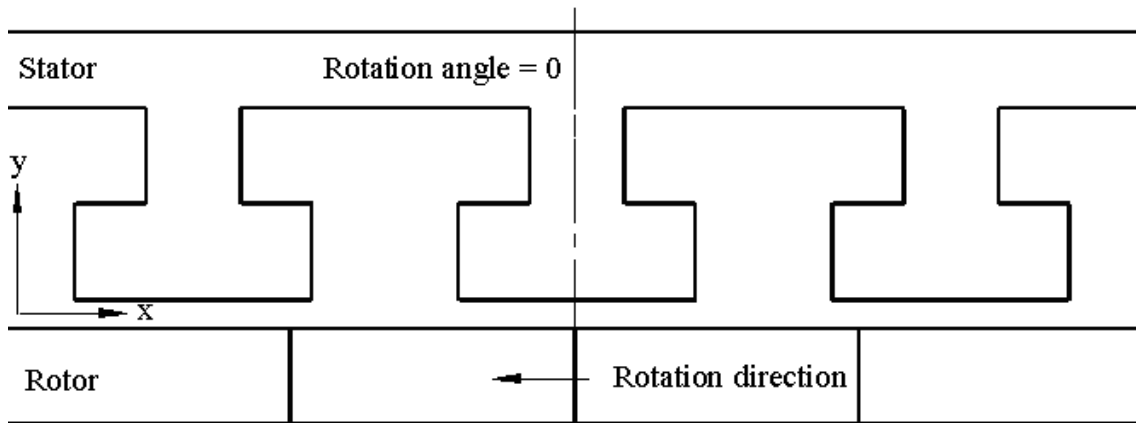


Fig. 5- 5. Schema of the initial rotation angle between the rotor and stator.

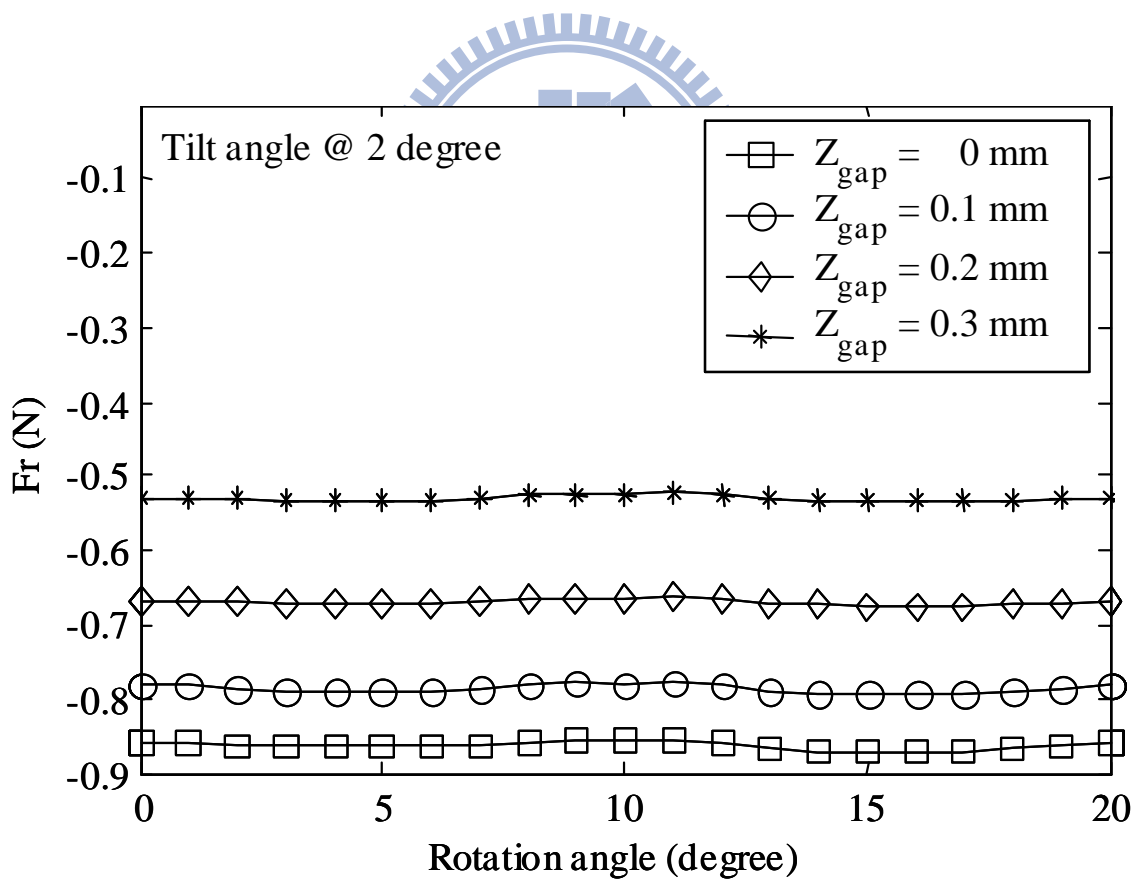


Fig. 5- 6. Restoring radial force varies with the rotation angle.

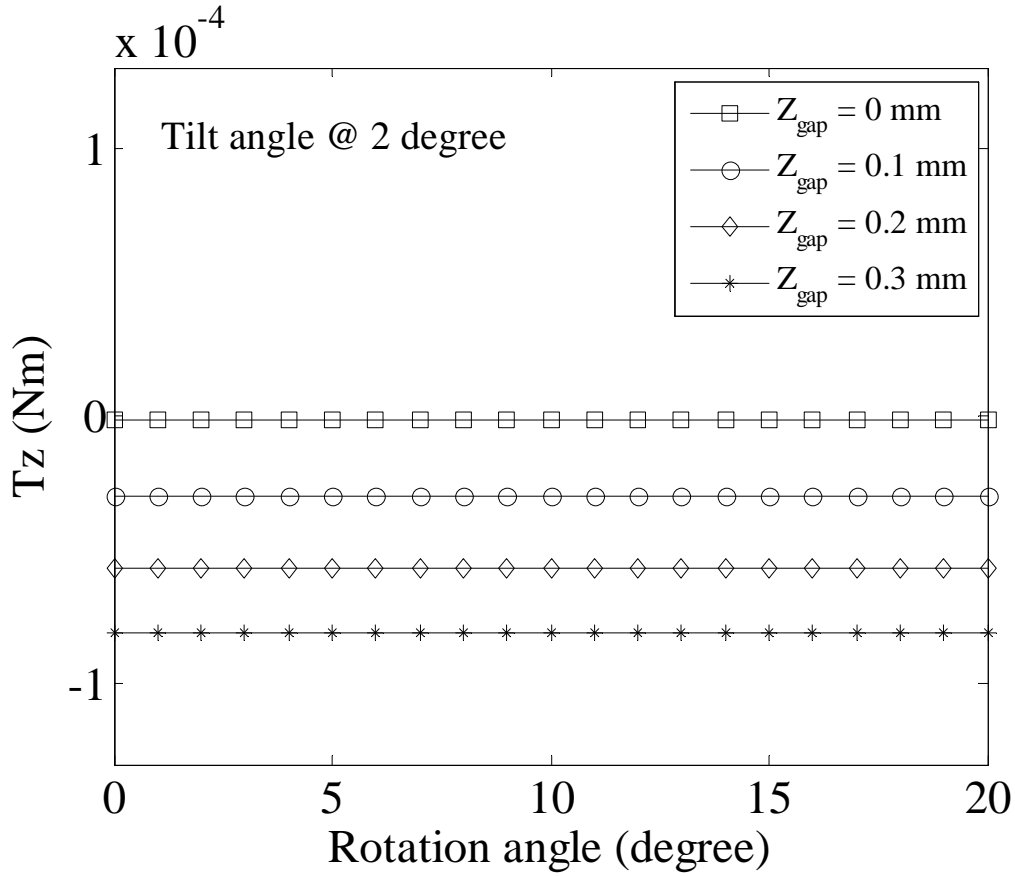


Fig. 5- 7 Friction loss due to magnetic axial force

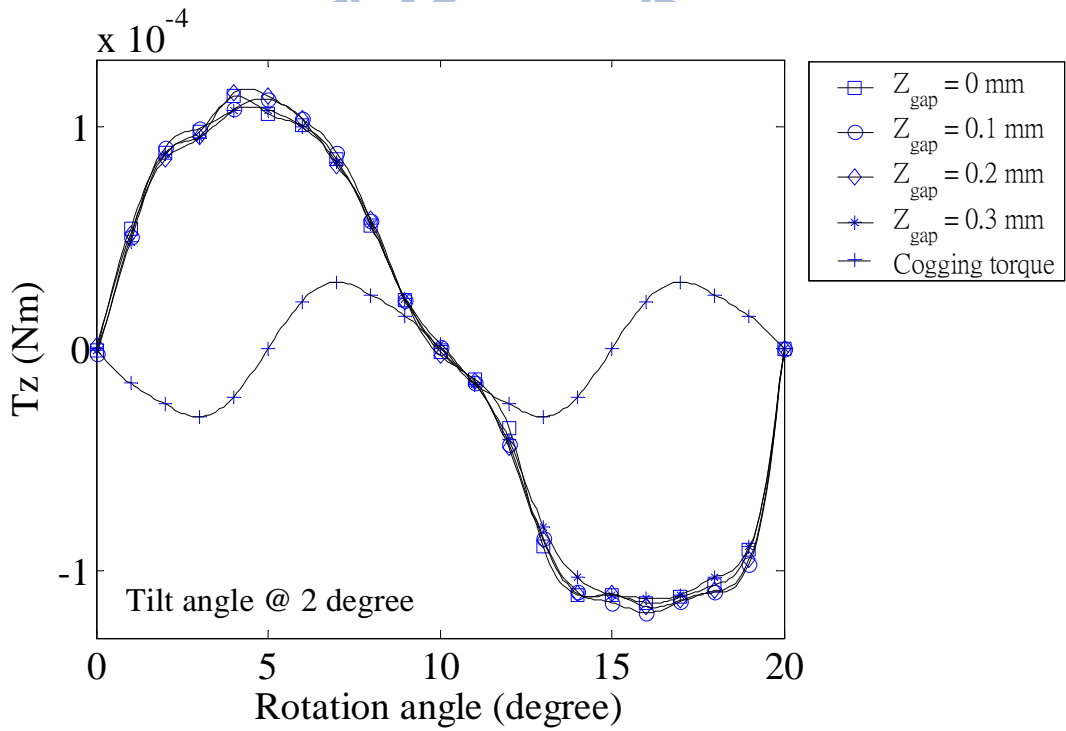


Fig. 5- 8. Total friction loss as a function of the rotation angle.

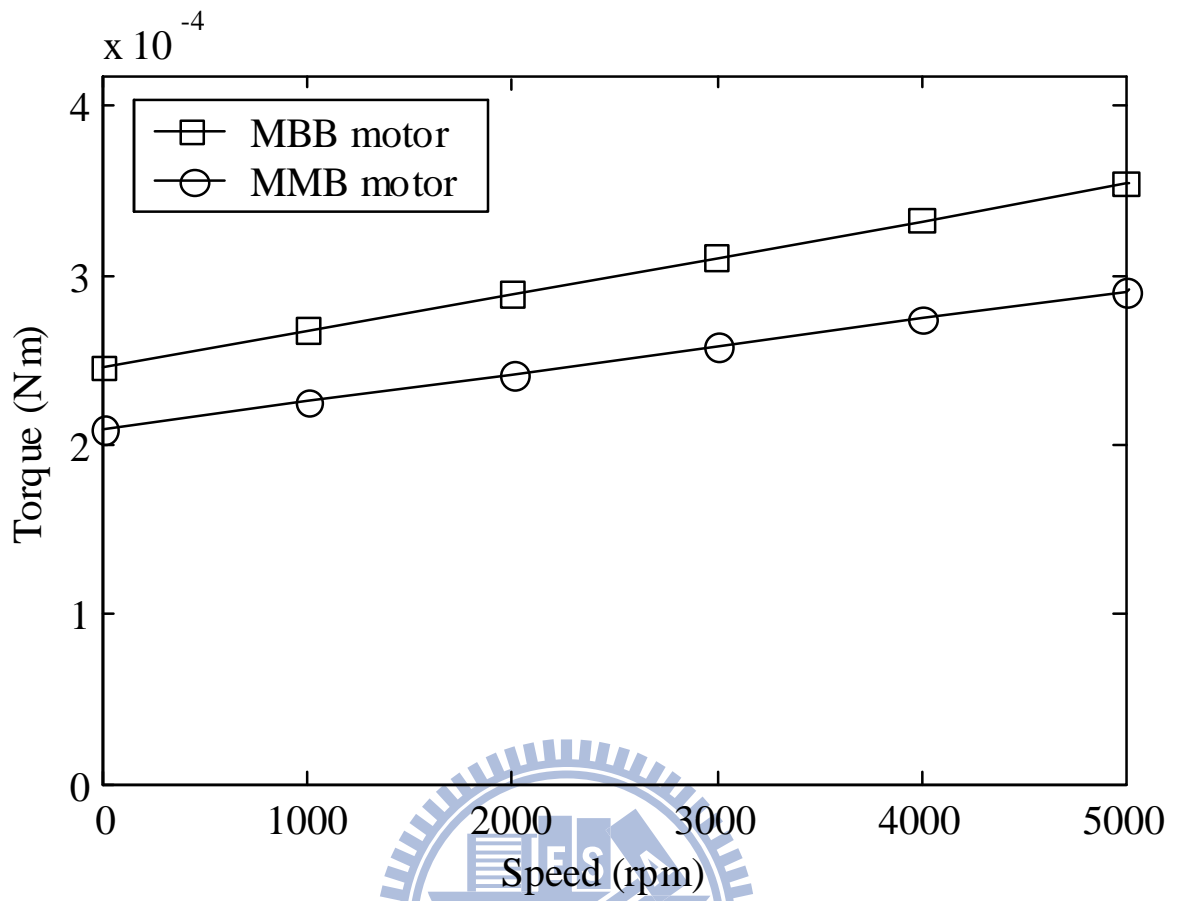


Fig. 5- 9. The comparison of friction loss of the MBB and MMB motor.

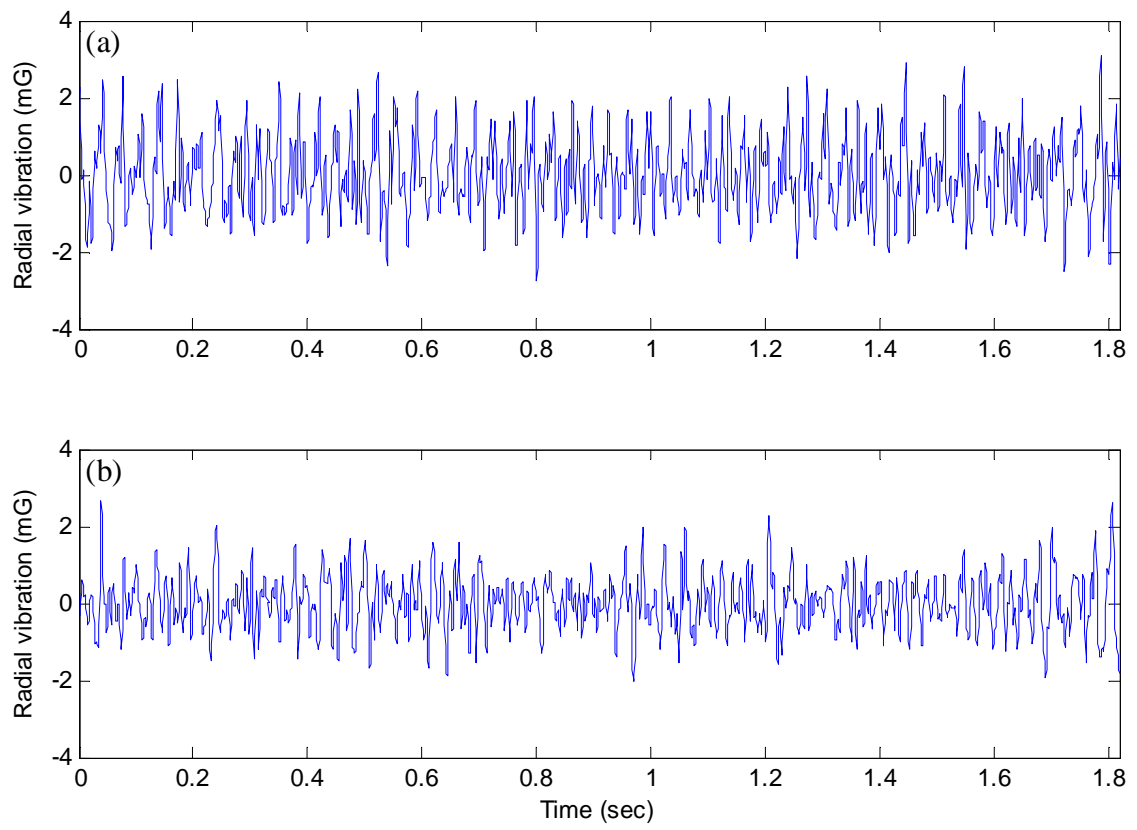
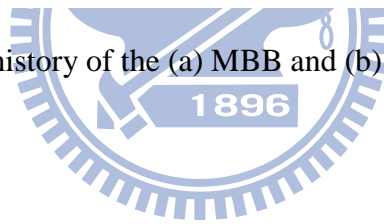


Fig. 5- 10. Radial vibration history of the (a) MBB and (b) MMB motor.



Chapter 6

Axial vibration study of a mobile fan motor

6.1 Introduction

A mobile fan motor for use in portable devices such as cell phones, ultra-mobile PCs, and mobile internet devices must be designed with low power consumption, low noise, and low vibration. Since the small fan is used for cooling the main digital signal processor chips or other integrated circuits, large vibration of the fan may become confused with an intentional vibration indicating a paging signal. So, ideally, the vibration should be reduced as much as possible. Therefore, the issue of suppressing the vibration of a mobile fan motor is very important.

From the view of bearing design, in this case a sleeve bearing, the axial load functions as an attractive force to prevent the rotor from jumping out of the micro motor when it encounters an external shock in the static or dynamic status. In general, for a flat-type motor, the axial preload is introduced using the magnetic attraction force between a permanent magnet (PM) and a magnetic sheet. Unfortunately, along with the axial thrust force, an Unbalanced Magnetic Force (UMF) is simultaneously created; i.e., they can not be decoupled for this type of motor. As is known, UMF and cogging torque

are main factors contributing to magnetically induced vibration. Jang *et al.* [63] performed an experimental study to show that rotor and stator eccentricities mainly generate a radial vibration at the first harmonic frequency and at the harmonics of the pole number. Hartman *et al.* [64] reported that the sources of UMF fall into the following categories: an eccentric rotor, an eccentric stator, and uneven magnetization. Yao *et al.* [65]-[66] showed that the mechanism of the reduction of cogging is illustrated by the minimum net integral of the product of normal and tangential magnetic flux with respect to the contour between the stator and rotor; and they proposed a method achieving a high efficiency and low cogging torque motor by altering the magnetization profiles of the permanent magnet and the design of the teeth of the stator in a motor. A few researchers [67]-[68] have focused on the characteristics of UMF related to a motor, adopting numerical and analytical approaches. However, the axial load effect, which accompanies UMF and results in the vibration of a miniature motor, is not addressed. The main goal of this paper is to understand the axial load effect related to the axial vibration in the development of a mobile fan motor.

The axial vibration of the micro motor is due to three essential factors: the radial vibration, the UMF, and the axial load. These are studied and analyzed. First, this paper deals with a simple physical model of the sleeve bearing motor to determine the relation between radial and axial vibrations, and it is presumed that the magnitude in the 1X

(where X designates the fundamental frequency) axial vibration harmonic should be a fraction of the radial one because the axial one is only a sine of a tilt angle times the magnitude of the 1X radial vibration harmonic due to the mass unbalance of the rotor. This assumption is experimentally validated. In addition, the frequency contents of the axial load coupled with the UMF for micro motors are numerically analyzed using FEM and compared with the experimental results. Furthermore, both the axial load effect with and without excited UMF are reported.

6.2 Design and force calculation

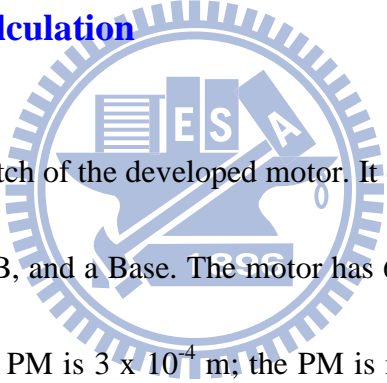


Fig. 6- 1 (a) shows the sketch of the developed motor. It consists of a spindle motor, a sleeve bearing system, a PCB, and a Base. The motor has 6 slots and 8 poles. The axial air gap between the coil and PM is 3×10^{-4} m; the PM is made of high energy product NdFeB with an inner radius of 2×10^{-3} m, an axial length of 5×10^{-3} m, and an outer radius of 4×10^{-3} m. Outside the PM, an iron yoke with a radial thickness of 6×10^{-4} m is mounted. The rotational speed of the micro motor is 6360 rpm, and the rated current is below 25 mA. The sleeve bearing has an inner radius of 4×10^{-4} m, an outer radius of 8×10^{-4} m, and an axial length of 2.5×10^{-3} m, and the clearance is 4 micro meters. To identify the model mentioned above, identical motors, M1 to M3, are the type with a symmetric magnetic sheet to preload the rotor; also, motor M1 is utilized to study the

axial load effect without UMF (motor M1P). To investigate the axial load effect under UMF, the second type micro motor, M4, with an asymmetric magnetic sheet, has been fabricated; the ratio of pole number to slot number is 6:2, and the other mechanical constraints are the same as those of the first type. In general, the shape of the magnetic sheet in motor M4 should be asymmetric in order to avoid the dead point [69]. M1P and M4P designate motors M1 and M4 without the sheet, respectively.

Fig. 6- 1 (b) displays the simplified model of a rotating rotor of the small motor.

Referring to Newton's second law, the unbalance force of the rotor can be represented

as

$$F = \bar{m}\bar{e}\omega^2 \sin(\theta) \quad (46)$$

where \bar{m} , \bar{e} , and ω denote the mass unbalance of the rotor, the rotor eccentricity, and rotor rotational speed, respectively. Since the bearing clearance is only 4 μm , it is

believed that the tilt angle theta rotates about the Y-axis, as shown in Fig. 6- 1 (b), and

can be small enough to lead to the result that the undesired axial vibration force is only

a fraction of the radial one for a well designed sleeve bearing motor. Therefore, once the

axial vibration of a motor is greater than the radial one, then both the preload and UMF

may be regarded as the principal contributors to the vibration. Definitely, based on this

assumption, the mass unbalance of each motor has to be maintained close to a level

which avoids propagating radial vibration which, in turn, leads to the rise of the axial

vibration.

Fig. 6- 2 presents the FEM model of the proposed motor with 892,892 tetrahedral elements. The sampling mechanical angle interval of one degree is utilized in estimating the preload force distribution of the motor. The preload profiles versus mechanical rotation angles and the corresponding frequency spectra after the FEM calculation are shown in Fig. 6- 3.

The mean values of the axial forces for motors M1, M4, and M4P are 32.11, 27.95, and 3.07 mN, respectively. While the axial force curve for motor M1 contains only a DC term, those of motors M4 and M4P contain 6X and 12X axial force harmonics, and the first two peak values in magnitude for motors M4 and M4P both occur at 6X (M4: 1.66 mN; M4P: 1.10 mN) and 12X (M4: 0.12 mN; M4P: 0.10mN) harmonics. Nonetheless, the 1X component is not generated; i.e., although the UMFs are induced in the motors M4 and M4P, they do not contribute to the 1X harmonic. For motors M4 and M4P, mass unbalance of these two motors are almost the same, and the simulated result indicates that the UMFs of these two motors do not contain the 1X axial force harmonic (which dominates the axial vibration of time domain). These results suggest that the axial load will effectively affect the axial vibration of the motors.

6.3 Experimental measurements

For measurement of the axial load, the rotor was tightly fixed to an accurate balance (see Fig. 6- 4), and the magnetic sheet was arranged above and locked at a manual xyz stage. After a centering device was applied to center the rotor and the magnetic sheet, the axial attraction force versus different axial air gaps was obtained. As the working distance was reached, the axial forces for M1 and M4 were 32.48 mN and 26.83 mN, respectively, which is consistent with the numerical results. To verify the vibration properties of the mobile fan motor, the measurement plant was constructed as shown in Fig. 6- 5. A precise accelerometer was utilized to detect the vibration. While the testing was performed, the motor was rotating at the rated speed of 6360 rpm. The accelerometer was attached to the motor to sense the traveling vibration signals; then the vibration was calculated and recorded by a spectrum analyzer. Finally, the vibration harmonics can be determined by using the fast Fourier transform method.

Three motors, M1 to M3, were prepared for identifying the simple model mentioned above. The corresponding frequency spectra of radial and axial vibrations are shown in Fig. 6- 6. It is clear that the magnitudes of the 1X components are the dominant reasons for the vibrations of the motors in both the radial and axial directions.

Table 6- 1 summarizes the magnitudes of the 1X harmonics of the radial and axial vibrations for these motors; the ratio of the axial vibration to the radial one is between

65 and 75 percent, which supports the model that the axial vibration of the small motor is only a fraction of the radial one. In addition, the result reveals that mass unbalance of the rotor is a key factor affecting the vibration of the motors.

6.4 Results and discussion

Fig. 6- 7 shows frequency spectra of radial and axial vibrations for the motors M1P (motor M1 without the magnetic sheet), M1, M4P (motor M4 without the magnetic sheet), and M4. It indicates that the 1X harmonic of the axial vibration is slightly increased to a value of 0.99 mG (see Table I, where $1G = 9.8 \text{ m/s}^2$) after the symmetric magnetic sheet is installed; i.e., the preload has slightly increased the axial vibration and its 1X harmonic. Fig. 6- 8(a) and Fig. 6- 8(b) show the axial vibration of the motors M1P and M1, respectively, and the amplitudes in peak-to-peak (pk-pk) are 11 mG and 15 mG for the former and latter, respectively.

Comparing the two graphs in Fig. 6- 7 (d), the motor M4P (top graph) demonstrates the 6X and 12X axial vibration harmonics due to the UMF, while the motor M4 merely includes the latter harmonic (see Table 6- 2). However, these two harmonics (6X and 12X) in magnitude were predicted by FEM analysis. The unexpected disappearance of the 6X harmonic for the motor M4 is believed to be associated with its asymmetrical coil (this means some defects in the coil were developed during the fabrication process),

and the induced UMF harmonics due to the defects are related to the pole number of magnets [64].

As mentioned earlier, the axial vibration results from three primary contributors: the UMF, the radial vibration, and the axial load. According to the numerical results, the UMFs of these two motors do not contribute to the 1X axial vibration harmonic. In addition, the measured magnitudes of the 1X radial vibration harmonic for these two motors are maintained nearly the same (M4P:5.986 mG; and 6.266 mG). However, the measured magnitude of the 1X axial vibration harmonic is enormously raised, and the ratio of this harmonic of motor M4 to motor M4P is approximately 41 percent. The reason might be that the lack of axial load leads to the growth of the magnitude of the 1X axial vibration harmonic; i.e., a weak axial load may result in an increase in the magnitude of the 1X axial vibration harmonic if the shaft is loose. Therefore, the axial preload plays an essential function in the reduction of the 1X axial vibration harmonic of the micro motor. Furthermore, comparing the axial vibrations of motors M4 and M4P reveals that the axial vibration is significantly reduced for motor M4. The amplitudes (pk-pk) of the axial vibrations for the motors M4P and M4 are 38 mG and 21 mG, respectively (see Fig. 6- 8 (c) and Fig. 6- 8 (d)).

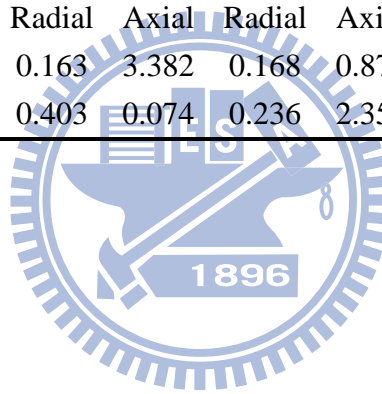
Table 6- 1 The magnitudes of 1X radial and axial vibration harmonics for motors M1P and M1 to M3.

Motor No.	Radial (mG)	Axial (mG)
M1P	6.279	3.051
M1	6.255	4.041
M2	5.850	4.124
M3	5.624	4.134

Table 6- 2 The magnitudes of radial and axial vibration harmonics for motors M4P and M4

Frequency	1X		6X		12X	
	Radial	Axial	Radial	Axial	Radial	Axial
M4P	5.986	9.083	0.163	3.382	0.168	0.879
M4	6.266	3.680	0.403	0.074	0.236	2.352

Unit (mG)



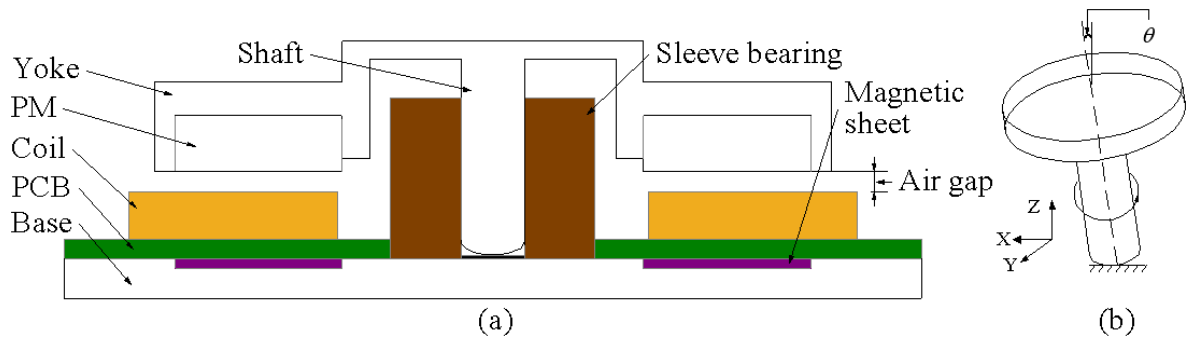


Fig. 6- 1. The sketch of (a) the micro motor and (b) the tilted rotor.

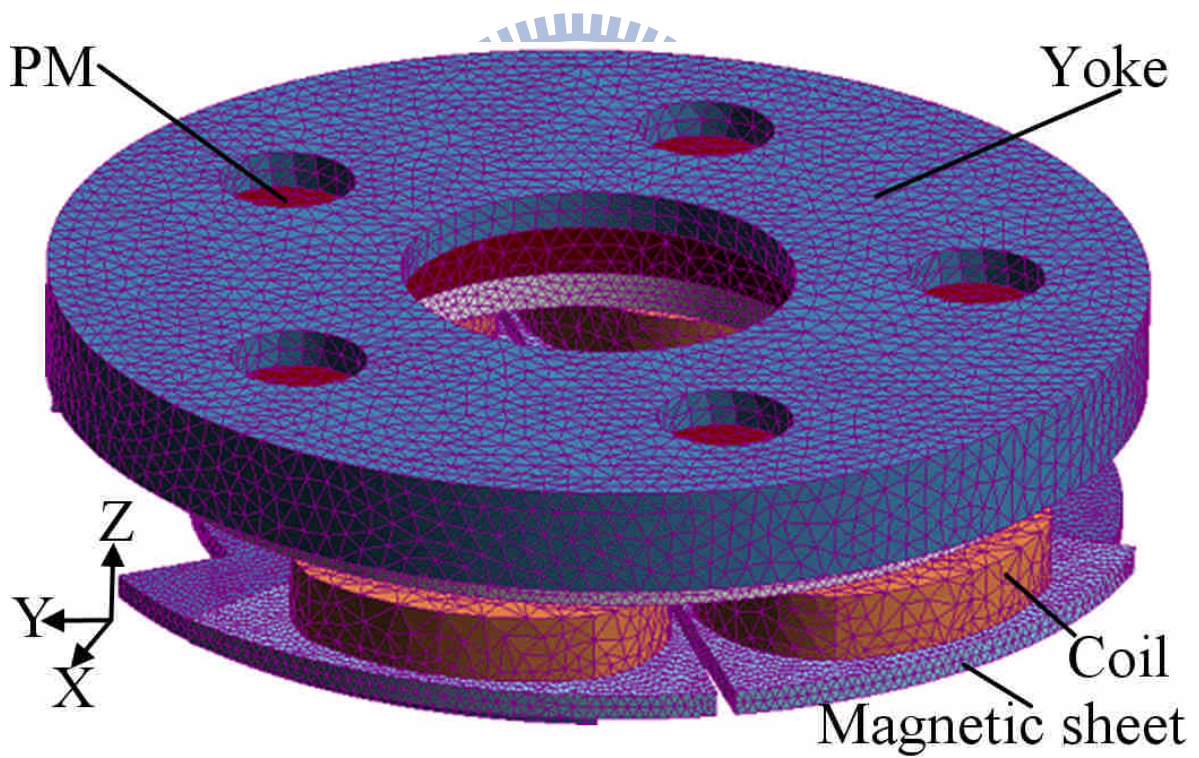


Fig. 6- 2. The FEM model of the mobile fan motor.

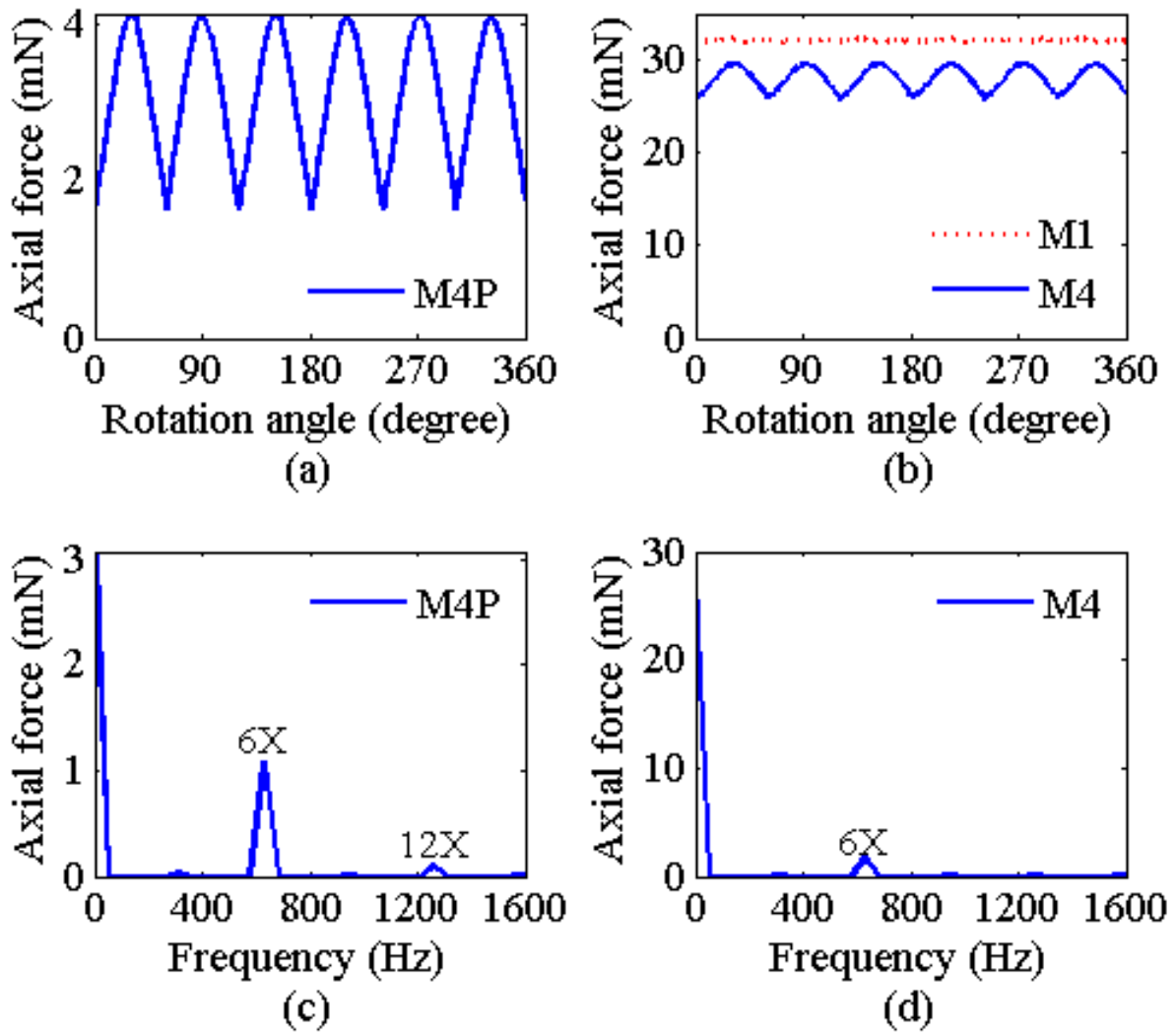


Fig. 6- 3.The simulated axial loads of spatial domain for motors: (a) M4P; and (b) M1 and M4; the frequency spectra for motors: (c) M4P; and (d) M4.

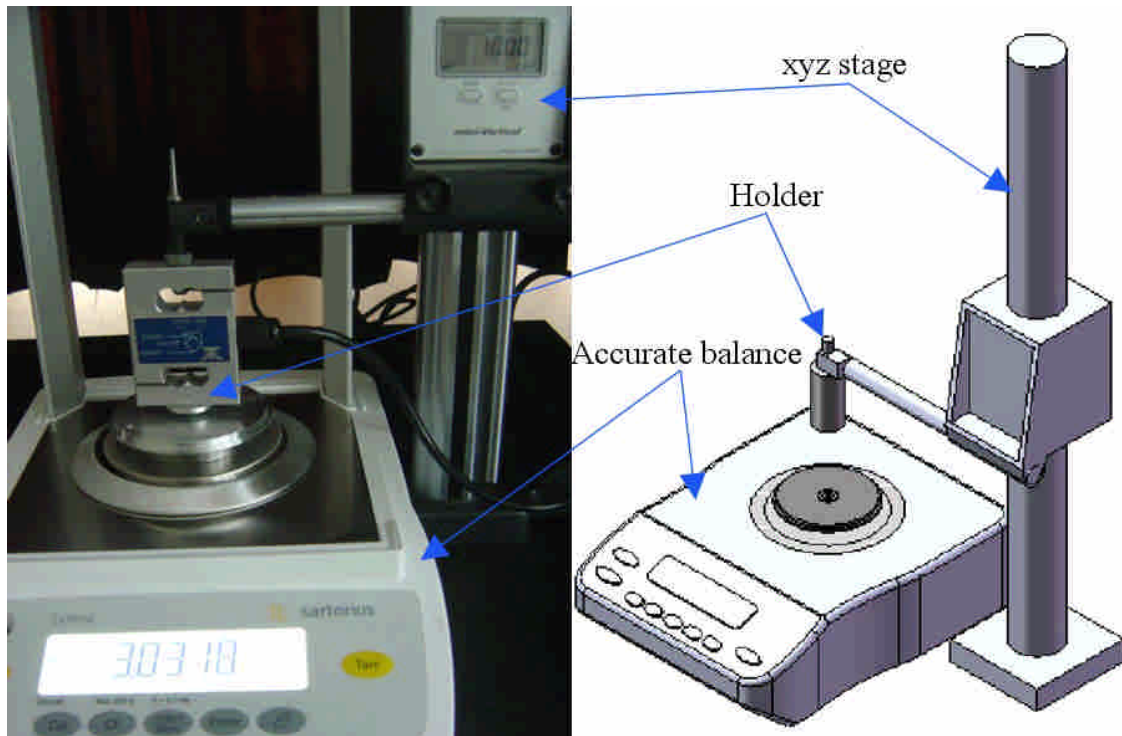


Fig. 6- 4. The structure of the test setup for the axial load measurement.

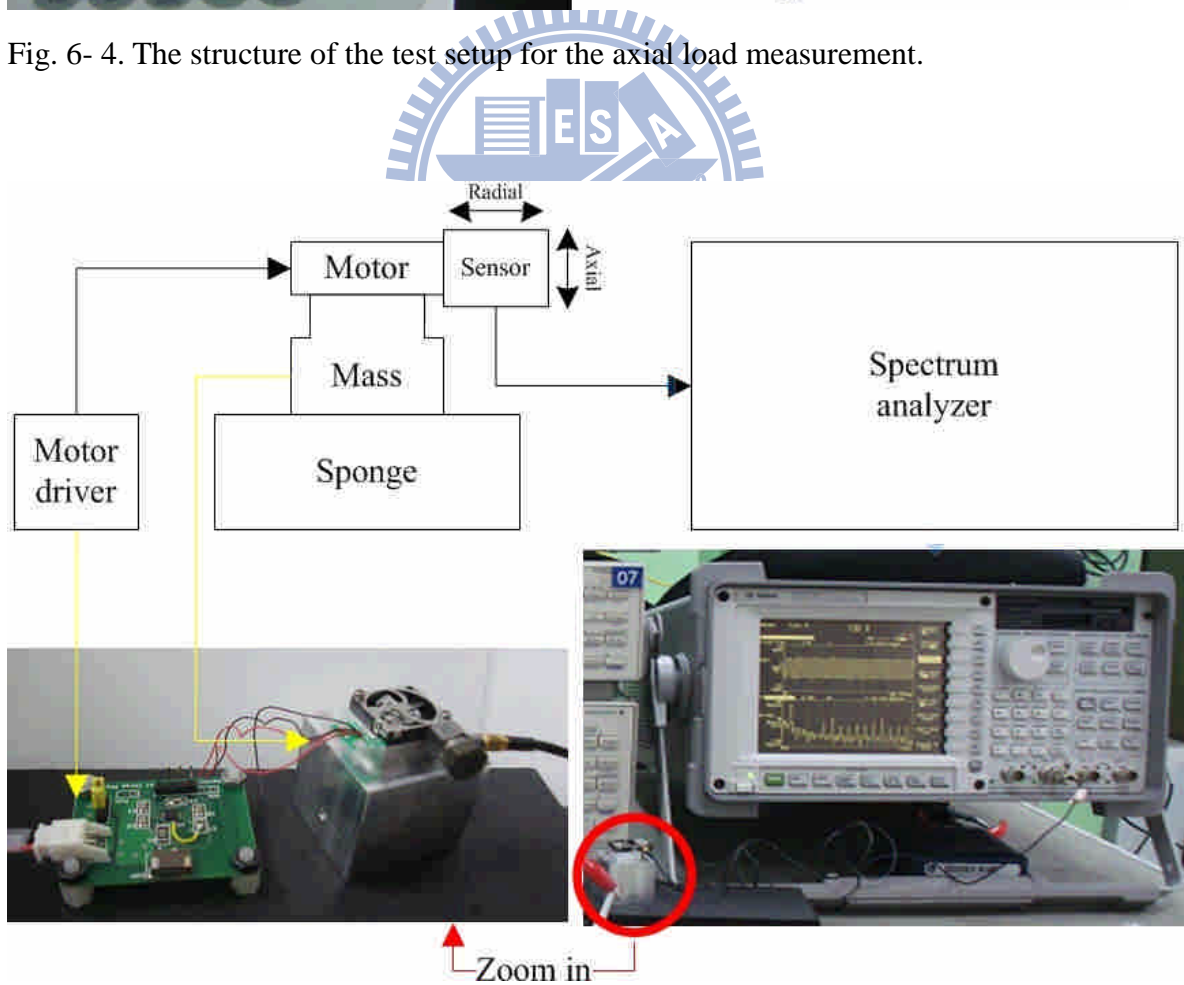


Fig. 6- 5. Configuration of the test setup for vibration measurement.

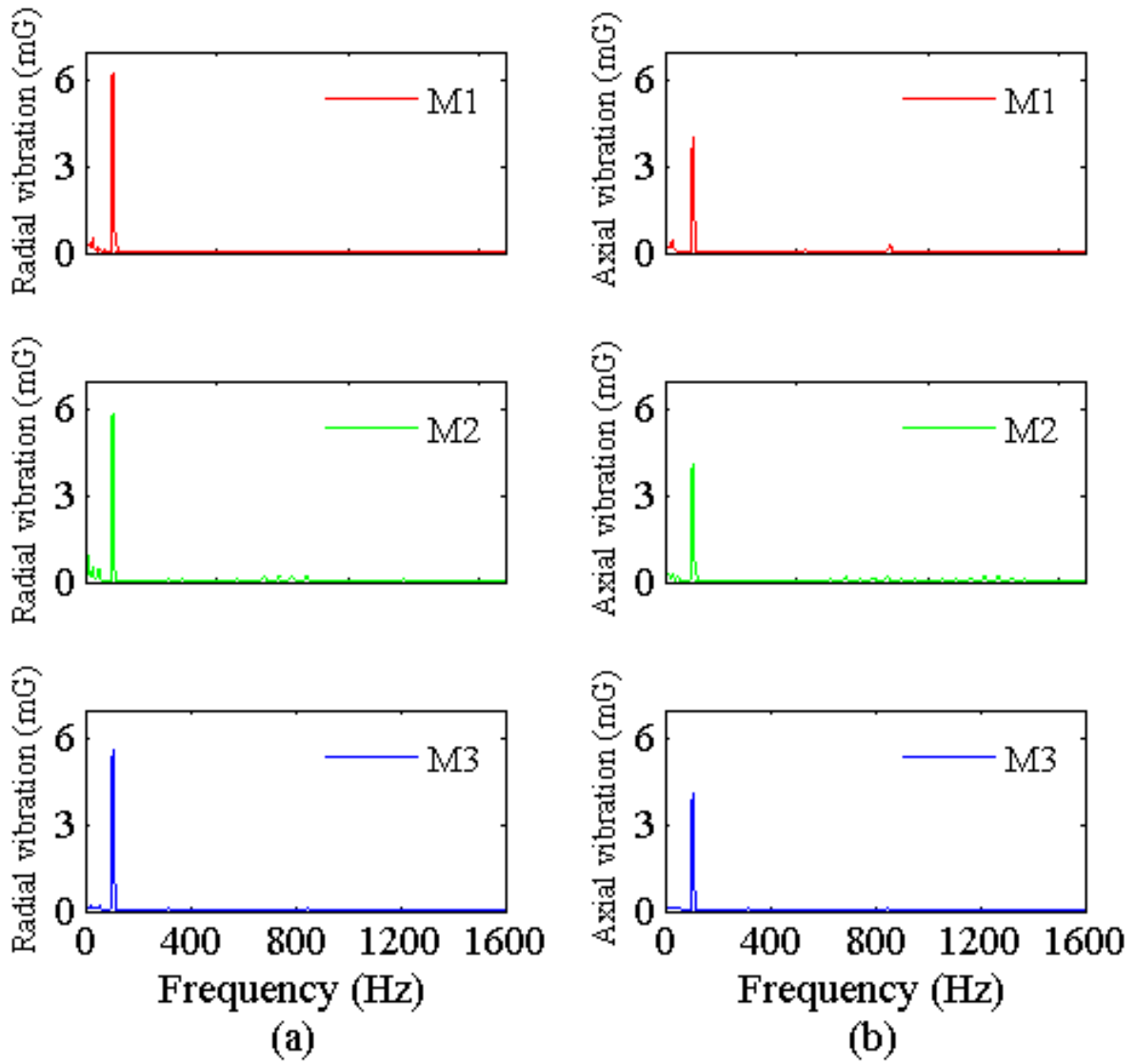


Fig. 6- 6. Frequency spectra of (a) radial and (b) axial vibrations for motors M1 to M3.

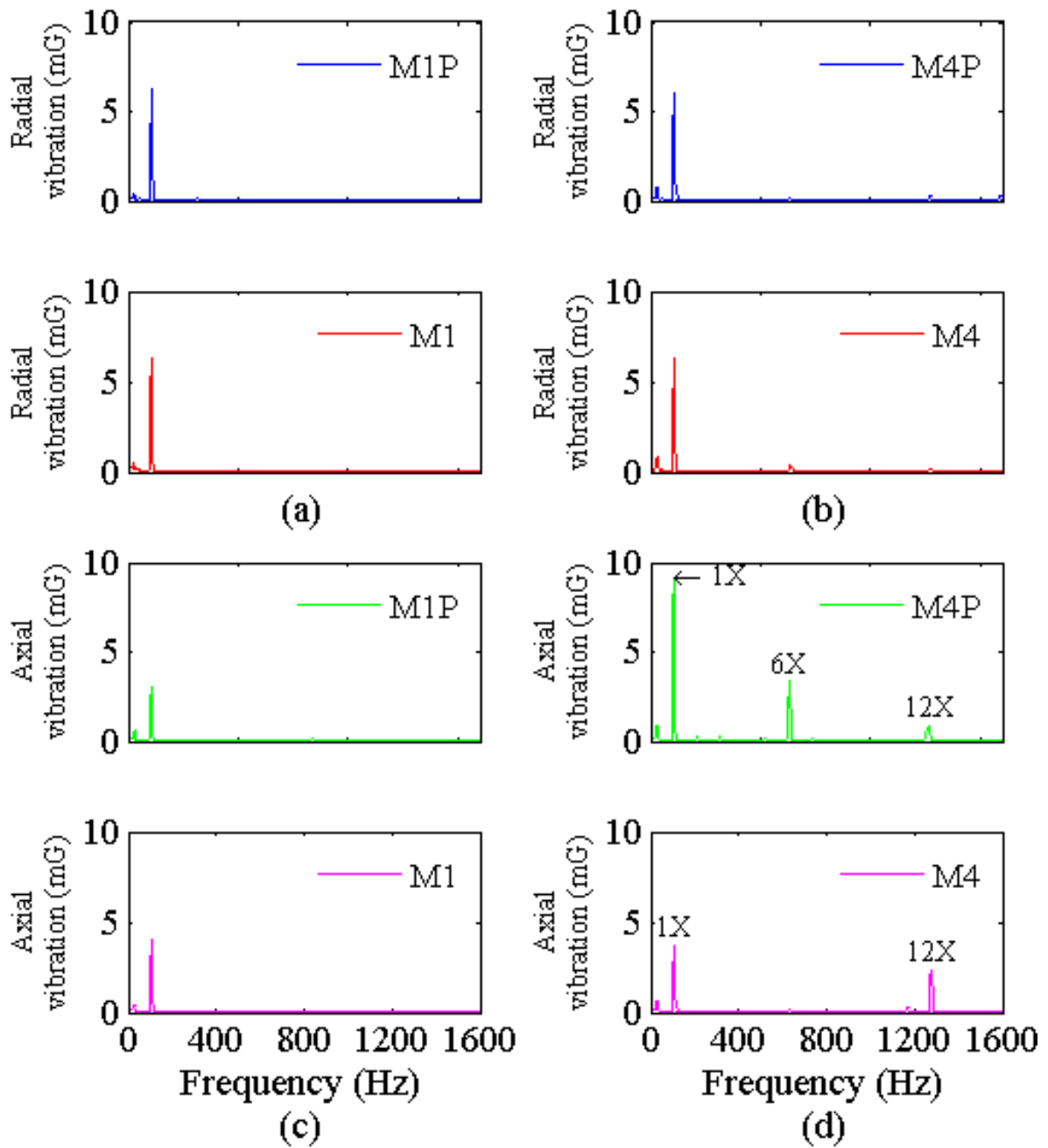


Fig. 6- 7. The frequency spectra of the radial and axial vibrations for motors. Radial vibration: (a) M1P and M1; and (b) M4P and M4; axial vibration: (c) M1P and M1; and (d) M4P and M4.

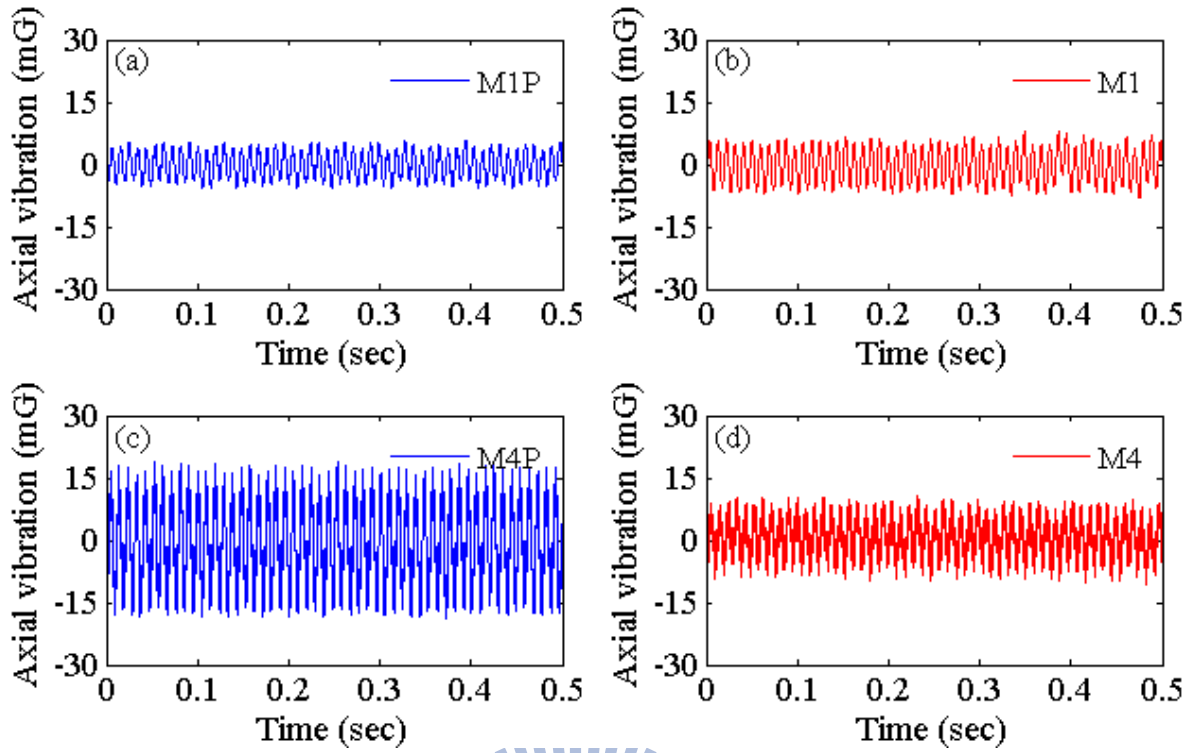
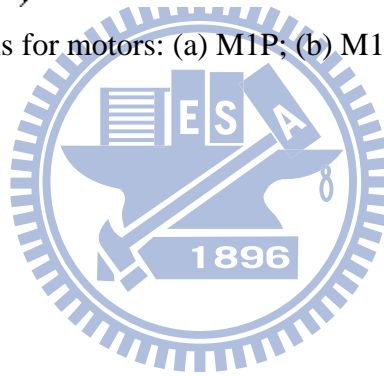


Fig. 6- 8. The axial vibrations for motors: (a) M1P; (b) M1; (c) M4P; and (d) M4.



Chapter 7

Conclusion

Referring to the above results and discussion, the conclusions of this dissertation are summarized below.

A credible mathematical model has been developed to predict the dynamic behaviour of the MB motor, and the numerically simulated RRO of the MB motor has good agreement with the experimental one. The system utilizing repulsive magnetic force is the one in which the rotor can be stably levitated in the radial direction, i.e., the highly compact MB configuration applying only a single pivot point can successfully get around Earnshaw's theorem and make achievable contact less of the rotor along radial direction. In addition, it is experimentally validated that in comparing this MB motor with the conventional ball type motor for small motor applications, it shows that the MB motor possesses the lower torque loss. Furthermore, the gyroscopic effect actively suppresses the radial vibration of the rotor due to the mass unbalance response while the spindle was operated within a speed range between 3000 and 6000 rpm. Accordingly, it is believed that a scaled-down version of the MB motor could be developed utilizing the presented structure to deal with the dynamic model; this will make possible the development of a miniature MB motor in the near future.

As is well-known, the passive MBs motor intrinsically represent the disadvantage of lack of damping, and the original damping ratio of our MB motor prototype is only 0.0655. On the basis of our simplified physical model of the MB motor the prediction shows that the novel damping device can effectively improved the damping ratio of the MB motor, and the experimental results show a good consistency with those of simulated one. The ratio in damping ratio of new development to the original one is 214 %. The natural frequencies for lateral and rotational modes of the rotor are around 22 Hz measured by impulse response method. It is 42 Hz below the rated speed of 64 Hz; therefore, the system resonance is avoided completely. Finally, we have demonstrated that the anti-shock performance is significantly improved by our innovative damping technology in a passive MB motor which will be useful for high density data storage applications.

Moreover, the radial vibration of the MB motor affected by axial force has been investigated. The lower net axial force of the motor can result in increasing the radial vibration of the motor. However, the applied bias-magnetic force contributing to suppressing the axial force of the motor can significantly reduce the radial vibration of the spindle motor when the resonant frequency is reached. Therefore, the bias-magnetic force could be useful for the reduction of the radial vibration of a MB motor. A compact bias-magnetic force device embedded in a MB motor would be implemented in the

future work.

In order to realize the effects of scaling down size of the MB configuration, two application examples were studied. One is the MMB motor with suppressed magnetic coupling effect expected for applying in the portable optical disc drives; the other one is preliminary study of the axial vibration for a mobile fan motor. For the investigation of the first case, the shaft can be rotated without any frictional contacts in radial direction. Furthermore, the MMB motor presents the lower friction loss than the conventional MBB type does. Moreover, the radial vibration (peak-peak) of the MMB motor is 21 % lower than the conventional MBB type. This shows that the innovative magnetic bearing research with the consideration of the magnetic coupling effect applied to the passive MMB motor improved the motor performance significantly. For the second case, we introduced an approach to realize the axial load effect for a flat-type motor with an axial air gap. When a symmetric magnetic sheet is utilized to produce the axial force for the developed micro motor with 6 slots/8 poles, the preload slightly increases the axial vibration of the spindle; however, when the asymmetric magnetic sheet is employed to preload the motor with 2 slots/6 poles and the intrinsically excited UMF, the preload significantly decreases the magnitude of the 1X axial vibration harmonic. Moreover, comparing the axial vibration of the small motor without and with the asymmetric magnetic sheet, the magnitudes of the axial vibration and its 1X harmonic for the latter

are 45 and 59 percent reduction of the former, respectively. It appears that the axial load highly affects the axial vibration of the mobile motor with an UMF.

The suggestions for the future study are listed as follows.

(1) Optimization of dimensions of ring magnet with strong repulsive force. The repulsive force is directly related to the stiffness of the MB; thus, an analytical solution of the force between the annular magnets can help to figure out the MB with more compact size while it represents an amazed repelling force.

(2) Taking into account the cross-coupled stiffness coefficients of a MB. Since the cross-coupled exists in the real system, if the term can be considered in the mathematical model, then how it affects the system can be realized.

(3) Study of the MB installed in a flat-type motor. As is known, a flat motor has the potential to be thin and small in size, so it is worth to investigate the performance of a flat motor designed with the MB.

Vitae (in Chinese)

姓名：王建昌

籍貫： 台灣省苗栗縣

論文題目：被動式微小型磁懸浮馬達之動態特性研究

A study of the dynamic behavior of a passive micro
magnetic suspension motor

學歷：

1988–1991 省立台中第二高級中學 畢業

1991–1995 私立東吳大學 物理學系 畢業

1995–1997 國立中正大學 物理研究所 碩士班 畢業

2004–2010 國立交通大學 材料科學與工程研究所 博士候選人

經歷：

July 1996–October 1997 工業技術研究院 研究生

September 1999–July 2003 工業技術研究院 副工程師

July 2003– 迄今 工業技術研究院 工程師



References

Chapter 1–2

- [1] M. Sagawa, S. Hirosawa, H. Yamamoto, S. Fujimura, and Y. Matsuura, “Nd–Fe–B permanent magnet materials,” *Jpn. J. Appl. Phys.*, vol. 26, pp. 785–800, June 1987.
- [2] M. Sagawa, S. Fujimura, H. Yamamoto, Y. Matsuura, and S. Hirosawa, “Magnetic properties of rare-earth-iron-boron permanent magnetic materials,” *J. Appl. Phys.*, vol. 57, pp. 4094–4098, April 1985.
- [3] A. K. and M. D. Simon, “Magnet levitation at your fingertips,” *Nature*, vol. 400, pp. 323–324, July 1999.
- [4] M. V. Berry and A. K. Geim, “Of flying frogs and levitrons,” *Eur. J. Phys.* vol. 18, pp. 307–313, June 1997.
- [5] C. K. McMichael, K. B. Ma, M. A., Lamb, M. W. Lin, L. Chow, R. L. Meng, P. H. Hor, and W. K. Chu, “Practical adaptation in bulk superconducting magnetic bearing applications,” *Appl. Phys. Lett.* vol. 60, pp. 1893–1895, April 1992.
- [6] C. Elbukem, M.B. Khamesee, and M. Yavuz, “Eddy current damping for magnetic levitation: downscaling from macro to micro-levitation,” *J. Phys. D: Appl. Phys.* vol. 39, pp. 3932–3938, September 2006.
- [7] S. Earnshaw, “On the nature of the molecular forces which regulate the constitution

- of the luminiferous ether,” *Trans. Camb. Philos. Soc.* vol. 7, pp. 97-112, 1839.
- [8] M. D. Simon, L. O. Heflinger, and S. L. Ridgway, “Spin stabilized magnetic levitation,” *Am. J. Appl. Phys.* vol. 65, no. 4, pp. 286-292, April 1997.
- [9] J. P. Yonnet, “Permanent magnet bearings and couplings,” *IEEE Trans. Magn.* vol. 17, no. 1, pp. 1169-1173, January 1981.
- [10] J. P. Yonnet, G. Lemarquand, S. Hemmerlin, and E. O. Rulliere, “Stacked structures of passive magnetic bearings,” *J. Appl. Phys.* vol. 70, pp. 6633-6635, November 1991.
- [11] C. C. Wang, Y. D. Yao, Y. H. Chang, P. C. Tung, and R. B. Xiao, “Magnetic force-induced damping effect for magnetic bearing motor,” *J. Appl. Phys.* vol. 97, pp. 10Q502-1-10Q502-3, May 2005.
- [12] G. Chen, “Study on nonlinear dynamic response of an unbalanced rotor supported on ball bearing,” *Trans. ASME, Journal of Vibration and Acoustics*, vol. 131, pp. 061001-1-061001-9, December 2009.
- [13] M. Tiwari, K. Gupta and O. Prakash, “Dynamic response of an unbalanced rotor supported on ball bearings,” *Trans. ASME, Journal of Sound and Vibration*, vol. 238, issue 5, pp. 757-779, December 2000.
- [14] V. V. Kharlamov, V. L. Kolmogorov, and S. V. Pavlishko, “Friction and wear model of a heavy loaded sliding pair Part III. Application to a lubricated plane bearing,”

International Journal Wear, vol. 241, pp. 65-78, June 2000.

[15] P. R. K. Murti, "Squeeze films in full porous metal bearings," International Journal

Wear, vol. 30, pp. 257-165, November 1974.

[16] A. Marinkovic, "Structural optimization of journal porous metal bearing," Trans.

FME, vol. 33, pp. 25-39, no. 1, 2005.

[17] P. J. Geary, "Magnetic and electric suspensions," S.I.R.A. Res. Rep. R314, 1964.

[18] J. P. Yonnet, "Passive magnetic bearings with permanent magnets," vol. MAG-14,

pp. 803-805, September 1978.

[19] W. E. Campbell, Boundary Lubrication, Boundary lubrication, an Appraisal of

World Literature, , ASME, New York, pp. 87-117, 1969.

[20] N. K. Myshkin, C. K. Kim, and M. I. Petrokovets, "Introduction to tribology",

Cheong Moon Gak, 1997.

[21] H. Moes, Lubrication and Beyond, University of Twenty Press, 2000.

[22] H. Shikata, Hitach powdered metals technical report, vol. 2, no. 2, 2003.

[23] J. W. Lund, F. K. Orcutt, "Calculations and Experiments on the Unbalance

Response of a Flexible Rotor," ASME Journal of Engineering for Industry, vol. 89,

pp. 785–796, November 1967.

[24] F. F. Ehrich, "The dynamic stability of rotor/stator radial rubs in rotating

machinery,” ASME Journal of Engineering for Industry, vol. 91, 1025–1028, November 1969.

[25] I. G. Begg, “Friction induced rotor whirl – A study in stability,” ASME Journal of Engineering for Industry, vol. 96, no. 5, pp. 450–453, May 1974.

[26] F. K. Choy, and J. Padovan, “Non-linear Transient Analysis of Rotor-Casing Rub Events,” Journal of Sound and Vibration, vol.113, no.3, pp.529-545, March 1987.

[27] J. H. Wang, Y. C. Sheu, and C. H. Chang, “Find the dynamic model of a spindle motor for CD-ROM drive by experimental measurement of the operation modes,” the Seventh National Conference on the Society of Sound and Vibration, R.O.C, pp. 12-19, 1999.

[28] S. X. Chen, Q. D. Zhang, Z. J. Liu, and H. Lin, “Design of fluid bearing spindle motors with controlled unbalanced magnetic forces,” IEEE Trans. Magn., vol. 33, no. 5, pp. 2638-2640, September 1997.

[29] A. Hartman and W. Lorimer, “Undriven vibrations in brushless DC motors,” IEEE Trans. Magn., vol. 37, no. 2, pp. 789-792, February 2001.

Chapter 3

[30] J. Delamare, E. Rulliere, and Yonnet, J.-P, “Classification and synthesis of permanent magnet bearing configuration,” IEEE Trans. Magn., vol. 31, no. 6, pp.

4190-4192, November 1995.

- [31] V. Fernandez, G. Reyne, and O. Cugat, "Prospective FEM modeling of induced planar micromotors," *IEEE Trans. Magn.*, vol. 35, no. 3, pp. 1805-1808, May 1999.
- [32] V. Fernandez, G. Reyne, O. Cugat, P.-A. Gilles, and J. Delamare, "Design and modeling of permanent magnet micro-bearings," *IEEE Trans. Magn.*, vol. 34, no. 5, pp. 3596-3599, September 1998.
- [33] V. Fernandez, J. Fandino, C. Sauvey, J.-Paul Yonnet, G. Reyne, and O. Cugat "A design methodology for permanent magnet microbearings," *IEEE Trans. Magn.*, vol. 36, no. 4, pp. 1919-1922, July 2000.
- [34] A. Tozune, "Vibration characteristics of motors with dynamic absorbers," *Electric Power Applications, IEE Proceedings B*, vol. 138, no. 1, pp. 21-27, January 1991.
- [35] H. Lotz, "Damping device for a magnetically supported rotor," U.S. Patent 5 910 695, June 1999.
- [36] J. Imlach, "Passive magnetic support and damping system," U.S. Patent 6 448 679, September 2002.
- [37] J. A. Tecza, and D. K. Rao, "Damping for passive magnetic bearings," U.S. Patent 5 521 448, May 1996.
- [38] V. Nguyen, J. Delamare, and J.-P Yonnet, "A passive damper for magnetic

suspension,” IEEE Trans. Magn., vol. 30, no. 6, pp. 4749-4751, 1994.

[39] K. Nagaya, H. Kojima, Y. Karube, and H. Kibayashi, “Braking forces and damping coefficients of eddy current brakes consisting of cylindrical magnets and plate conductors of arbitrary shape,” IEEE Trans. Magn., vol. 20, no. 6, pp. 2136-2145 1984.

[40] G. Genta, C. Delprete, A. Tonoli, E. Rava, and L. Mazzocchetti, “Analytical and experimental investigation of a magnetic radial passive damper,” IEEE Trans. Magn., in Proceedings of the third International Symposium Magnetic Bearings, pp. 255-264, July 1992.

Chapter 4



[41] W. K. Hong, “Spindle motor having magnetic bearing,” U. S. Patent 5 783 886 June 1998.

[42] M. Takahashi, “Axial load carrying magnetic bearing for a rotatable body,” U.S. Patent 6 175 174 B1, January 2001.

[43] D. H. Jeong, “Non-contact driving motor,” U.S. Patent 6 420 810 B1, July 2002.

[44] G. H. Jang, and J. S. Park, “Development of a highly efficient hard disk drive spindle motor with a passive magnetic thrust bearing and a hydrodynamic journal bearing” J. Appl. Phys. 97, 10Q507-1-10Q507-3, May 2005.

[45] C. C. Wang, Y. D. Yao, P. C. Tung, R. B. Xiao, and Y. H. Chang, “Magnetic

force-induced damping effect for magnetic bearing motor,” J. Appl. Phys. 97, 10Q502-1-10Q502-3, May 2005.

[46] J. Delamare, E. Rulliere, and J. P. Yonnet, “Axial bearings using superconductors and permanent magnets,” IEEE Trans. Mag., vol. 31, pp. 4190-4192, November 1995.

[47] V. Fernandez, J. Fandino, C. Sauvey, J. P. Yonnet, G. Reyne, and O. Cugat, “A design methodology for permanent magnet microbearings,” IEEE Trans. Mag., vol. 36, pp. 1919-1922, November 1995.

[48] W. K. Hong, “Spindle motor having magnetic bearing,” U.S. Patent 5 783 886 July 1998.

[49] S. Earnshaw, “On the nature of molecular force...,” Trans. Cambridge Philisophical Society, vol. 7, part 1, pp. 97-112, 1839.

[50] C. M. Harris, Shock and Vibration Handbook, 4th ed., McGraw-Hill, New York: 1995, pp. 6.4-6.9.

Chapter 5

[51] D. L. Blankenbeckler, D. H. Davies, W. W. A. Dunford, B. W. Bell Jr., and R. H. Hamer, “Performance characteristics of a 32 mm small form-factor optical disc and drive,” Jpn. J. Appl. Phys., vol. 43, no. 7B, pp. 4896-4899, July 2004.

[52] S. B. Luitjens, M.W. Blum, B. M. de Boer, W. F. J. Fontijn, M. A. H. van der Aa.,

“Small form factor optical drive: miniaturized plastic high NA objective lens and optical drive,” Proceedings of ISOM/ODS 2002, pp. 251-253, July 2002.

[53] S. B. Luitjens, M. W. Blum, B. M. deBoer, W. F. J. Fontijn, and M. A. H. van der Aa, “Small form factor optical Portable Blue drive power consumption considerations,” in Proc. Intl’ Conf. Consumer Electronics (ICCE). IEEE Press, June, 2003.

[54] S. Q. Lee, K. H Park and M. C. Paek, International Symposium on Optical Memory and Optical Data Storage (ISOM 2005), WP5, Honolulu, Hawaii, USA, July 2005.

[55] C. C. Wang, Y. D. Yao, P. C. Tung, R. B. Xiao, and Y. H. Chang, “Magnetic force-induced damping effect for magnetic bearing motor,” J. Appl. Phys., vol. 97, 10Q502-1-10Q502-3, May 2005.

[56] V. Fernandez, J. Fandino, C. Sauvey, J. P. Yonnet, G. Reyne, and O. Cugat, “A design methodology for permanent magnet microbearings,” IEEE Trans Magn., vol. 36, pp. 1919-1922, July 2000.

[57] J. Delamare, J. P. Yonnet, and E. Rulliere, “A compact magnetic suspension with only one axis control,” IEEE Trans Magn., vol. 30, pp. 4746-4748, November 1994.

[58] Z. Q. Zhu and D. Howe, “Analytical prediction of the cogging torque in radial field permanent magnet brushless motors,” IEEE Trans Magn., vol. 28, no. 2, pp.

1371-1374, March 1992.

- [59] K. J. Han, H. S. Cho, D. H. Cho, H. R. Cho, H. S. Lee, and H. K. Jung, "Optimal core shape design for cogging torque reduction of brushless DC motor," IEEE Trans Magn., vol. 36, no. 4, pp. 1927-1931, July 2000.
- [60] T. Li and G. Slemon, "Reduction of cogging torque in permanent magnet motors," IEEE Trans Magn., vol. 24, no. 6, pp. 2901-2903, November 1988.
- [61] C. S. Koh, and J. S. Seol, "New cogging-torque reduction method for brushless permanent-magnet motors," IEEE Trans Magn., vol. 39, no. 6, pp. 3503-3506, November 2003.
- [62] P. S. Shin, H. D. Kim, G. B. Chung, H. S. Yoon, G. S. Park, and C. S. Koh, "Shape optimization of a large-scale bldc motor using an adaptive RSM utilizing design sensitivity analysis," IEEE Trans Magn., vol. 43, no. 4, pp. 1653-1556, April 2007.

Chapter 6

- [63] C. I. Lee, and G. H. Jang, "Experimental Measurement and Simulated Verification of the Unbalanced Magnetic Force in Brushless DC Motors," IEEE Trans. Magn. vol. 44, no. 11, pp. 4377-4380, November 2008.
- [64] A. Hartman and W. Lorimer, "Undriven vibrations in brushless DC motors," IEEE Trans. Magn., vol. 37, no. 2, pp. 789-792, March 2001.
- [65] Y. D. Yao, D. R. Huang, J. C. Wang, S. H. Liou, S. J. Wang, T. F. Ying and D. Y. Chiang, "Simulation study of the reduction of cogging torque in permanent magnet

- motors,” IEEE Trans. Magn., vol. 33, no. 5, pp. 4095-4097, September 1997.
- [66] Y. D. Yao, D. R. Huang, J. C. Wang, S. J. Wang, T. F. Ying and D. Y. Chiang, “Study of a high efficiency and low cogging torque spindle motor,” IEEE Trans. Magn., vol. 34, no. 2, pp. 465-467, March 1998.
- [67] S. X. Chen, Q. D. Zhang, Z. J. Liu, and H. Lin, “Design of fluid bearing spindle motors with controlled unbalanced magnetic forces,” IEEE Trans. Magn., vol. 33, no. 5, pp. 2638-2640, September 1997.
- [68] C. M. Chao, S. J. Wang, C. P. Liao, D. R. Huang, and T. F. Ying, “Torque and cogging torque in sandwich type CD-ROM spindle motor,” IEEE Trans. Magn., vol. 34, no. 2, pp. 471-473, March 1998.
- [69] B. I. Kwon, B. Y. Yang, S. C. Park, and Y.S. Jin, “Novel topology of unequal air gap in a single-phase brushless DC motor,” IEEE Trans. Magn., vol. 37, no. 5, pp. 3723-3726, September 2001.

Publication List

Journal papers

1. **C. C. Wang**, Y. D. Yao, Y. H. Chang, Pi. C. Tung, and R. B. Xiao, “Magnetic force-induced damping effect for magnetic bearing motor,” J. Appl. Phys., vol. 97, pp. 10Q502-1-10Q502-3, May 2005.
2. **C. C. Wang**, Y. D. Yao, “Development of micromagnetic bearing motors with suppressed magnetic coupling effect for small form factor for optical drives,” J. Appl. Phys., vol. 99, 08R302-1-08R302-3, February 2006.
3. **C. C. Wang**, Y. D. Yao, C. S. Liu, L. Y. Cheng, “Micro Magnetic Suspension Motor Design for Miniature Optical Drive,” Jpn. J. Appl. Phys., vol. 45, no. 7, pp. 5801-5803, July 2006.
4. **C. C. Wang**, and Y. D. Yao, “Bias-magnetic force for vibration reduction of magnetic bearing motors,” IEEE Trans. Magn., vol. 43, no. 6, pp. 2486-2488, June 2007.
5. **C. C. Wang**, Y. D. Yao, K. Y. Liang, C. C. Huang, Y. C. Chang, and D. A. Lowther, “Axial vibration study of a mobile fan motor,” IEEE Trans. Magn., vol. 46, no. 6, pp. 1397-1399, June 2010.

Conference papers

1. **C. C. Wang**, Y. D. Yao, Y. H. Chang, P. C. Tung, and R. B. Xiao, "Magnetic force-induced damping effect for magnetic bearing motor," 49th Annual conference on Magnetism and Magnetic Materials (MMM), GQ-26, Jacksonville, Florida, USA, November 2004.
2. **C. C. Wang**, Y. D. Yao, C. S. Liu, L. Y. Cheng, "Micro magnetic suspension motor design for miniature optical drive," International Symposium on Optical Memory and Optical Data Storage (ISOM 2005), MP1, Honolulu, Hawaii, USA, July 2005.
3. **C. C. Wang**, Y. D. Yao, S. J. Wang, "Development of micromagnetic bearing motors with suppressed magnetic coupling effect for small form factor for optical drives," 50th Annual conference on Magnetism and Magnetic Materials, HR-17, San Jose, California, USA, November 2005.
4. **C. C. Wang**, Y. D. Yao, S. J. Wang, "A novel micro magnetic bearing motor design," International Magnetism Conference (Intermag), CV-09, San Diego, California, USA, May 2006.
5. **C. C. Wang**, Y. D. Yao, "Bias-magnetic Force for vibration reduction of magnetic bearing motors," 10th Joint MMM/Intermag Conference, ET-03, Baltimore, Maryland, USA, January 2007.
6. **C. C. Wang**, Y. D. Yao, K. Y. Liang, C. C. Huang, Y. C. Chang, and D. A. Lowther, "Axial vibration study of a mobile fan motor," 11th Joint MMM/Intermag Conference, GV-05, Washington, DC, USA, January 2010.
7. **C. C. Wang**, Y. D. Yao, K. Y. Liang, Y. C. Chang, and D. A. Lowther, "Passive magnetic levitation for small motor applications," 11th Joint MMM/Intermag Conference, CP-04, , Washington, DC, USA, January 2010.